1994

Hollow core optical fiber sensors for monitoring static and dynamic stress in large structures

Jing Wang
Lehigh University

AUTHOR:

Wang, Jing

TITLE:

Hollow Core Optical Fiber Sensors for Monitoring Static and Dynamic Stress in Large Structures

DATE: January 15, 1995

Hollow Core Optical Fiber Sensors for Monitoring Static and Dynamic Stress In Large Structures

by

Jing Wang

A Thesis
Presented to the Graduate and Research Committee of Lehigh University in Candidacy for the Degree of Master of Science

in
Electrical Engineering Department

Lehigh University
December 9, 1994

Hollow Core Optical Fiber Sensors for Monitoring Static and Dynamic Stress in Large Structures

Jing Wang

Thesis submitted and approved in partial fulfillment of the requirements for the degree of Master of Science in Electrical Engineering.

_____
Date

_____
Thesis Advisor

_____
Thesis Advisor

_____
Chairperson of Department

Acknowledgements

I gratefully acknowledge my advisor, Dr. K. D. Bennett of Lafayette College, for his abundant help in all areas of my research work, for supporting me with direction, encouragement, challenge, and friendship, for the progress I have achieved toward my Master's degree. I also thank my advisor Dr. D. Christodoulides who first gave me the opportunity to work and study in the area of linear and nonlinear optics, for many helpful discussions, and for his encouragement.

I also would like to thank the sponsor of this work, The Center for Advanced Technology for Large Structural Systems at Lehigh University. Their generous support has enabled me to pursue a Master's degree, and I greatly appreciate this valuable experience and academic achievement.

Sincerest thanks also go to my mentors and teachers Mr. G. B. Liu, Mr. F. A. Gao and my parents Mr. Z. C. Wang and Mrs. F. Y. Liu who introduced me to science and electronics during elementary and high school years, and put me through college to learn Electromagnetic and Microwave Technology in China. Their support, love, and understanding have always encouraged me to go forward.

I also wish to acknowledge my fellow members of the Photonics Technology Laboratory at Lafayette College where I did all experimental study and most of my thesis, for their help and friendship.

I would like to give my thanks to my best friend K. A. Mosher, for her solid spiritual support all throughout my graduate work, for her patient and endless help to get me through the language barrier.

My special thanks also go to C. Dedert, my English tutor and good friend, who helped me to pass the TOEFL and GRE exams, which were the prelude to my graduate studies.

Finally, I would like to thank my dearest husband W. Z. Meng for his love and comfort, understanding, unconditional support, endless encouragement and respect.

Table of Contents

Abstract

This research work explores the possibility of fiber optic load monitors and accelerometers. The sensors studied in this work consist of a transmitting and receiving multimode fiber inserted into the two ends of a short length of hollow core fiber; deflection of the hollow fiber due to pressure or acceleration leads to a transmission loss between the fibers. Two approaches were taken to demonstrate the unique characteristics of this fiber sensor mechanism. First, loss due to axial displacement of multimode, step-index fiber ends was calculated using a ray optics model which assumed a Gaussian power distribution among the fiber modes, and experiments were performed to confirm its accuracy. Second, the much more complicated problem of predicting losses in the bent hollow core fiber was addressed. The computer simulation was expanded to model the light emitted from the transmitting fiber end face, trace the light as it propagates through a certain length of bent hollow core fiber, and calculate the amount of power captured by the receiving multimode fiber.

In order to realize construction of the the intensity modulated sensor, the affect of changing various sensor parameters was studied, including fiber type, diameter, numerical aperture, end separation, launching condition, and cleave angle. Many theoretical concepts from ray optics, matrix optics, Gaussian beam theory, and existing spot size measurement techniques were considered. Electromagnetic tunneling was reviewed, as it affects the reflection of radiation at a curved dielectric interface. Finally, a prototype sensor was assembled and tested under loading conditions. The results are analyzed and assessed.

1. Introduction

Optical fiber sensors are essentially a means whereby light guided within an optical fiber can be modified in response to an external physical, chemical, biological or similar influence. An optical fiber sensor generally includes three parts: an optical source and an optical detector whose relevant optical properties remain constant, and an optical fiber at which the measurement is to take place. light is launched by the optical source into the fiber and captured by the optical detector; the light can be allowed to exit the fiber and be modulated in a separate zone before being relaunched into either the same or a different fiber; such sensors are called *extrinsic.* Alternatively, in intrinsic sensors, the light can continue within the fiber and be modulated in response to the measurand while still being guided.

The main advantages of optical fiber sensor include immunity from electromagnetic interference and radio frequency interference, electrical isolation, chemical passivity, small size and low weight, intrinsic safety in explosive environments, high reliability and security with no risk of fire/sparks.

Fiber optic sensors that have been presented in the literature include pressure, temperature, liquid level, liquid refractive index, liquid PH, antibodies, electric current, rotation, displacement, acceleration, acoustic, and electric and magnetic fields. Initial developmental work has concentrated on military applications like fiber optic hydrophones for submarine and undersea application, and gyroscopes for applications in ships, missiles and aircraft. Gradually, a large number of civilian applications have also picked up. Fiber optic sensors are expected to play a major role in future industrial, medical, aerospace, and consumer applications.

Our early work we have done dealt with an intensity modulated optical fiber sensor that is based on the deflection of the hollow core fiber. Two 100/140 μm (core/cladding) step index fibers were pulled away from each other in a straight hollow core fiber having an inner diameter of 145 μm (a flexible glass tube) with a predetermined gap left between them. One fiber is connected to the optical source, an LED for our experiments, the other

was connected to an optical photodetector. The hollow core sleeve was affixed to a strip of spring steel which was vertically deflected, or bent by a micrometer screw. A curve depicting bend loss as a function of the deflection distance was reasonably linear. It is quite clear that the sensitivity is a function of the fiber end gap (fiber end separation), we also would like to know how the other parameters such as the fiber numerical aperture and diameter, launching conditions from the source to the fiber, and the refractive-index profile will affect the sensitivity.

From splices in communications applications to sensing applications using fiber to fiber coupling, models to determine optical loss caused by fiber misalignment in butt joints have been studied for many years. Several models appear in the literature for calculating loss due to small angular and longitudinal misalignments in multimode, step-index fiber butt-joints [1–3]. Unfortunately, there is little agreement between the calculated and the predicted results, and few if any deal with large separations. In addition, most of these models make the assumption that there is a uniform power distribution across the face of the emitting fiber (transmitting fiber), especially for step-index multimode fibers [4]. Based on the concept of diffraction of light, if there was a uniform energy distribution across the face of the emitting fiber, airy pattern with the radius of the central disk would be observed at the far field. In practice, only a Gaussian-like power distribution was noticed by using CCD camera. Gaussian-like curves could be Gaussian ; polynomial; hyperbolicsecant. We would like to emphasize that Gaussian power distribution is not a Gaussian beam that must be restricted by the intensity distribution; beam waist; beam divergence; phase; wavefronts and so on. The Gaussian power distribution we have discussed is that the intensity distribution in any transverse plane is a circularly symmetric Gaussian function centered about optical axis, but this beam diverges much faster than the Gaussian beam. In fact, the beam emitting from the step-index multimode fiber spreads just like that predicted in our model depending on the experimental measurement.

As a part of this work, a computer model has been created based on these needs. Rather than a uniform power distribution, the power distribution across the cone of radiation defined by the numerical aperture at any point on the fiber core is assumed to be Gaussian in form. The model is based on ray optics principles; only meridional rays were considered

because of the circular symmetry of the power distribution, and because meridional models have been shown to accurately represent the more complicated situation which includes skew rays in many situations [5]. This model of ray propagation thus allows the use of a transfer matrix approach.

The power distributions which were calculated in a few transverse planes centered at optical axis away from the emitting fiber end matched experimental data extremely well, these are Gaussian power distributions. The longitudinal separation loss versus the separation distance was calculated, it also agreed the experimental data well. Comparing bending results of the model and the experimental data doesn't give very good agreement. one of the seasons could be explained that meridional rays is not enough to predict the propagation of the rays when the rays path is bent, this could be a very complicated problem. Our future work could focus on using cones instead of the meridional rays.

Chapter 2 discusses the basic concepts we are use in the computer simulation to predict the mechanisms of the light propagation in the fiber and also can produce the results of the axial displacement and bending tests of the hollow core fiber. The fundamental principles of wave optics will be discussed in Chapter 3, while it is not necessary to read the chapter to understand the sensing concepts, it is helpful and provides a background. Chapter 4 reviews the properties of Gaussian beams which we used to pay great attention, it will help to understand that the foundamental mode of the single mode fiber is transformed into the fundamental gaussian beam mode when the waves is radiated from the fiber end. Chapters 5 and 6 include the principle and characteristics of the computer model, model results and sensitivity optimization. Chapter 7 covers the principle of our sensor, the experimental set-ups and a discussion of the results. The overall conclusions which can be drawn from this work are presented in the final chapter.

2. Ray Optics Representation

Electromagnetic propagation along optical waveguides is described exactly by Maxwell's equations. However, it is well known that classcal geometric optics provides an approximate description of light propagation in regions where the refractive index varies only slightly over a distance comparable to the wavelength of light. An intuitive picture of the propagation mechanism in an ideal multimode step-index optical waveguide is most easily seen by a simple ray (geometrical) optics representation.

2.1 Snell's Law and Total Internal Reflection

Refraction occurs when light passes from one homogeneous isotropic medium to another; the light ray will be bend at the interface between the two media. The mathematic expression that describes the refraction phenomena is known as Snell's Law, which follows:

$$n_1 \sin\alpha_i = n_2 \sin\alpha_t \quad , \tag{2.1}$$

where

n_1 = index of refraction of the first medium
n_2 = index of refraction of the second medium
α_i = angle between the incident ray and the normal to the interface
α_t = angle between the refracted ray and the normal to the interface

Figure 2.1a shows the case for light passing from a high index medium to a lower index medium. Even though refraction is occuring, a certain portion of the incident ray is reflected. If the incident ray hits the boundary at ever increasing angles, a value of $\alpha_1 = \alpha_c$ will be reached, at which no refraction will occur. The angle, α_c, is called the critical angle. The refracted ray of light propagates along the interface, not penetrating into the lower index medium as shown in Figure 2.1b. At that point, $\sin\alpha_t$ is equal to unity. For angles α_i, greater than α_c, the ray is entirely reflected at the interface and no refraction takes place as shown in Figure 2.1c. This phenomenon is known as total internal reflection.

In Figure 2.2, a ray of light incident on the end of an optical fiber at an angle θ will be refracted as it passes into the core. If the ray travels through the high index media at an angle greater than α_c, it will reflect off the cylindrical wall, make multiple reflections, and will emerge at the other end of the optical fiber. For a circular fiber, considering only meridional rays (which will be discussed later), the entrance and exit angles are equal. Considering Snell's Law for the optical fiber, core index n_1, cladding index n_2, and the surrounding media index n_0, then,

$$\begin{aligned} n_0 \sin\theta_0 &= n_1 \sin\theta_1 \\ &= n_1 \sin(\pi/2 - \alpha_c) \\ &= n_1 [1 - (n_2/n_1)^2]^{1/2} \\ &= (n_1^2 - n_2^2)^{1/2} = NA \end{aligned} \qquad (2.2)$$

The quantity $n_0 \sin\theta_0$ is defined as the numerical aperture (NA), and is determined by the difference in refractive index between the core and the cladding. It is a measure of the light acceptance capability of the optical fiber. As the NA increases, so does the ability of the fiber to couple light into the fiber, as shown in Figure 2.3a. The larger NA allows the fiber to couple in light from more severe grazing angles. Coupling efficiency also increases as the fiber diameter increases, since the large fiber can capture more light (see Figure 2.3b). Therefore, the maximum light collection efficiency occurs for large diameter core and large NA fibers.

Here we also would like to introduce Fresnel's law which gives the reflection and refraction coefficient at the interface of the two different media. The nature of reflection and refraction can be extracted by considering the electric and magnetic fields perpendicular to the direction of the light propagation. First we look the case where the electric field lies in the x-y plane of Figure 2.5a, which corresponds to the plane in which the interface between the regions of index n_1 and n_2 lies. This corresponds to the case of wave propagation characterized as transverse elctric field (TE) polarization. The boundary condition that the electric field must be continuous across the interface is expressed

$$E_i + E_r = E_t \quad , \qquad (2.3)$$

while the boundary condition that the tangential component of H must be continuous across the interface gives

$$-H_i \cos\alpha_i + H_r \cos\alpha_r = -H_t \cos\alpha_t \quad . \tag{2.4}$$

Using the law of reflection $\alpha_i = \alpha_r$ in (2.4) results in

$$-H_i \cos\alpha_i + H_r \cos\alpha_i = -H_t \cos\alpha_t \quad . \tag{2.5}$$

Using Faradays's Law

$$\nabla \times \vec{E} = \varepsilon \frac{\partial \vec{H}}{\partial t} \quad , \tag{2.6}$$

which is equivalent to

$$\vec{k} \times \vec{H} = -\varepsilon\omega\vec{E} \quad , \tag{2.7}$$

where $k = 2\pi/\lambda$, with λ being the wavelength of the light beam. $\vec{k}$ having a direction along the propagation path of the light beam (see Fig.2.4), $H_i = (1/\mu\omega)\, k_i E_i$, $H_r = (1/\mu\omega)\, k_r E_r$, and $H_t = (1/\mu\omega)\, k_t E_t$, and Eq.(2.5), we have

$$-k_i E_i \cos\alpha_i + k_r E_r \cos\alpha_i = -k_t E_t \cos\alpha_t \quad . \tag{2.8}$$

where ε and μ are the permittivity and permeability of the medium respectivily. Going through a similar process for the case shown in Figure 2.5b, where the transverse magnetic field (TM) is in the x-y plane, the corresponding equations for Eqs.(2.3), (2.5), and (2.6) are

$$H_i + H_r = H_t \tag{2.9}$$

$$E_i \cos\alpha_i - E_r \cos\alpha_i = E_t \cos\alpha_t \tag{2.10}$$

and

$$K_i E_i + K_r E_r = -K_t E_t \tag{2.11}$$

Eliminating E_r and E_t, the reflection and refraction coefficients for the TE and TM polarized light beams are given by

$$r_F^E = \left(\frac{E_r}{E_i}\right)_{TE} = \frac{n_1 \cos\alpha_i - n_2 \cos\alpha_t}{n_1 \cos\alpha_i + n_2 \cos\alpha_t} \tag{2.12}$$

$$t_F^E = \left(\frac{E_t}{E_i}\right)_{TE} = \frac{2n_1 \cos\alpha_i}{n_1 \cos\alpha_i + n_2 \cos\alpha_t} \tag{2.13}$$

$$r_F^H = \left(\frac{E_r}{E_i}\right)_{TM} = \frac{n_2 \cos\alpha_i - n_1 \cos\alpha_t}{n_2 \cos\alpha_i + n_1 \cos\alpha_t} \tag{2.14}$$

$$t_F^H = \left(\frac{E_t}{E_i}\right)_{TM} = \frac{2n_1 \cos\alpha_i}{n_2 \cos\alpha_i + n_1 \cos\alpha_t} \tag{2.15}$$

It is important to note that the reflection and refraction coefficient of the two polarization states differ, and consequently, a beam may become increasingly polarized by making a series of reflections that favor one polarization state at the expense of another.

2.2 Meridional Rays and Skew Rays

The definition of total internal reflection and numerical aperture have been based on meridional ray analysis (i.e., the ray path, through its numerous reflections, passes through the longitude axis of the fiber). Using Figure 2.2 as a reference, it can be shown that the length of a meridional ray in a fiber in air ($n_0 = 1$) is:

$$l(\theta) = \frac{L}{[1 - (\sin\theta/n_1)^2]^{1/2}}$$

$$= L \sec(\theta_1) \quad , \tag{2.16}$$

where $l(\theta)$ is the length of the optical path for a ray inclined to the fiber axis at an angle θ_0, and L is the length of the fiber measured along the fiber axis. It is interesting to note that the length of the optical path for an incident ray depends only on the fiber length, the angle of incidence, and the refractive

index of fiber core, while being independent of fiber diameter. The number of reflections, however, is dependent on fiber diameter. The larger the diameter of the fiber, the fewer the number of reflections as defined below:

$$N = (L/2a) \tan \theta_1 \quad , \tag{2.17}$$

where N is the number of reflections at the core/cladding interface and a is the fiber radius.

In general, meridional rays describe a very simplified ray propagation. Often rays are skewed in nature and dominate the optical properties of the fiber. These rays affect the "real" ray propagation and alter the simplified definition of numerical aperture, ray propagation and number of reflections.

Skew rays are not confined to a single plane, but instead tend to follow a helical path along the fiber as illustrated in Figure 2.6. These rays are more difficult to track as they travel along the fiber, since they do not lie in a single plane. Although skew rays constitute a major portion of the total number of guided rays, their analysis is not necessary to obtain a general picture of rays propagating in a fiber. The examination of meridional rays will suffice for this purpose. A more detailed treatment of skew rays is given in references [6]-[8].

2.3 Matrix Optics

Matrix optics is a technique for tracing paraxial rays (which will be discussed in chapter 4). The rays are assumed to travel only within a single plane, so that the formalism is applicable to systems with planar geometry and to meridional rays in circularly symmetric systems.

2.3.1 Ray Transfer Matrix

A ray can be described by its position and its angle with respect to the optical axis in a optical system. These variables are altered as the ray travels through the system. In the paraxial approximation, the position and angle at the input and output planes of an optical system are related by two linear algebraic equations. As a result, the optical system is described by a 2×2 matrix called the ray-transfer matrix.

The convenience of using matrix methods is that the ray-transfer matrix of a cascade of optical components or systems is a product of the ray-transfer matrices of the individual components or system. Matrix optics provides a formal mechanism for describing complex optical systems in the paraxial approximation.

Consider a circularly symmetric optical system formed by a succession of refracting and reflecting surfaces all centered about the same axis (the optical axis). The z axis lies along the optical axis and points in the general direction in which the rays travel. Consider rays in a plane containing the optical axis, say the y-z plane. We proceed to trace a ray as it travels through the system, i.e., as it crosses the transverse planes at different axial distances. A ray that crossing the transverse plane at z is completely characterized by the coordinate y of its crossing point and the angle θ that it makes with the optical axis.

An optical system is a set of optical components placed between two transverse planes at z_1 and z_2, refereed to as the input and output planes, respectively. The system is characterized completely by its effect on an incoming ray of arbitrary position and direction (y_1,θ_1). It steers the ray so that it has new position and direction (y_2,θ_2). Schematic expression shows in Figure 2.7.

In the paraxial approximation, when all angles are sufficiently small so that $\sin\theta \approx \theta$; the relation between (y_2,θ_2) is linear and can generally be written in the form

$$y_1 = Ay_1 + B\theta_1 \tag{2.18}$$

$$\theta_2 = Cy_1 + D\theta_1 \tag{2.19}$$

where A,B,C,D are real numbers. Equations (2.18) and (2.19) may be conveniently written in matrix form as

$$\begin{bmatrix} y_2 \\ \theta_2 \end{bmatrix} = \begin{bmatrix} A & B \\ C & D \end{bmatrix} \begin{bmatrix} y_1 \\ \theta_1 \end{bmatrix} \tag{2.18}$$

The matrix $\vec{M}$, whose elements are A,B,C,D, characterizes the optical system completely since it permits (y_2,θ_2) to be determined for any (y_1,θ_1). It is known as the *ray-transfer matrix.*

Based on this concept in which rays travel in free space along straight lines, a ray traversing a distance d is altered in accordance with $y_2 = y_1 + \theta_1 d$ and $\theta_2 = \theta_1$. The ray-transfer matrix is therefore

$$\vec{M} = \begin{bmatrix} 1 & d \\ 0 & 1 \end{bmatrix} \tag{2.19}$$

2.3.2 Matrices of Cascaded Components

A cascade of optical components whose ray-transfer matrices are $\vec{M}_1$, $\vec{M}_2$, ..., $\vec{M}_N$ is equivalent to a single optical component of ray-transfer matrix

$$\vec{M} = \vec{M}_N \ldots \vec{M}_2 \vec{M}_1.$$

Note the order of matrix multiplication: the matrix of the system that is crossed by the rays first is placed to the right, so that it operates on the column matrix of the incident ray first.

2.4 Bent Fiber

The reflection of a local plane wave from a curved interface between two nonabsorbing dielectric media has some differences from the simple planar interface described in connection to the Fresnel equations [9,10]. It could be simply said that total internal reflection does not exist for a curved interface. Here we would like to introduce the formula for the effect of a dielectric interface on the reflection and refraction of plane waves for arbitrary values of the refractive indices on either side of the interface. This analysis is applicable to interfaces of general shape. When the interfaces is concave toward the denser medium, the total internal reflection is prevented by electromagnetic tunneling. These results could be applied to determine the reflective and refractive coefficients of an optical slab waveguide, an optical fiber, or a hollow core fiber under bending.

2.4.1 Plane Interface

Consider a plane wave incident, in the optically denser medium, at a plane interface between two nonabsorbing dielectric media of refractive indices n_1 and $n_2 < n_1$ as shown in Figure 2.8. The incidence and transmission angles relative to the normal are α_i and α_t, respectively. When the wave is incident at an angle that is greater than or equal to the critical angle α_c, it is totally reflected. For $y \geq 0$, the electromagnetic field is evanescent and decays exponentially away from the interface [11].

For $\alpha_i < \alpha_c$, the wave is only partially reflected, since some of the incident light energy is transmitted normally to the less dense medium. The transmitted or refracted wave originates at the interface by Snell's Law of Eqn. (2.1), so that the critical angle is that value of α_i for which at $\alpha_t = \pi/2$; thus

$$\sin\alpha_c = n_2 / n_1 \quad . \tag{2.20}$$

We define a power transmission coefficient T as

$$T = 1 - \frac{\text{Power of the reflected wave}}{\text{Power of the incident wave}} \quad . \tag{2.21}$$

For the plane interface, T is given by Fresnel's classical expression $T = T_F$. When $\alpha_i \geq \alpha_c$, $T_F = 0$, and when $0 \leq \alpha_i \leq \alpha_c$, the transmission coefficient depends on the polarization of the incident wave. If the electric vector is parallel to the interface ($E_y = 0$) then $T_F = T_F^E$, from (2.11), T_F^E should be

$$T_F^E = 1 - (t_F^E)^2 = \frac{4\,[1-(\cos\alpha_c/\cos\alpha_i)^2]^{1/2}}{\{1+[1-(\cos\alpha_c/\cos\alpha_i)^2]^{1/2}\}^2} \quad . \tag{2.22 a}$$

When the magnetic vector is parallel to the interface ($H_y = 0$) then $T_F = T_F^H$,

$$T_F^H = 1 - (t_F^H)^2 = \frac{4\,[1-(\cos\alpha_c/\cos\alpha_i)^2]^{1/2}/\sin^2\alpha_c}{\{1+[1-(\cos\alpha_c/\cos\alpha_i)^2]^{1/2}/\sin^2\alpha_c\}^2} \quad . \tag{2.22 b}$$

In the case of nearly equal refractive indices, $n_1 \approx n_2$, $\sin\alpha_c \approx 1$, and $T_F^H \approx T_F^E$. On the other hand, when $\sin\alpha_c \approx \alpha_c$ and the refractive indexes are arbitrary

$$T_F^H \approx T_F^E \sin^2\alpha_c \approx 4\,[1-(\cos\alpha_c/\cos\alpha_i)^2]^{1/2}. \qquad (2.22\,c)$$

2.4.2 Curved Interface

Snell's Law and Fresnel's Law were used only for plane interface. Next we would like to introduce the formulas for a curved interface. In general, when a plane wave is incident on a curved interface, it is only partially reflected, even when the angle of incidence is larger than the critical angle. A. W. Snyder and J. D. Love investigated the reflection of a local plane wave from a curved interface between two nonabsorbing dielectric media. Some formulas have already been derived for different situations.

From Figure 2.9, it's easy to understand that the waves $y_{tp} = 0$, i.e., those with $\alpha_i \le \alpha_c$ will be called refracting waves. The waves with $y_{tp} > 0$, i.e., those with $\alpha_i > \alpha_c$ will be called tunneling waves.

The power transmission coeffecient for a curved interface is given as

$$T = |T_F|\, C \quad . \qquad (2.23)$$

where T_F is Fresnel's classical transmission coeffecient for a plane interface between nonabsorbing media as given by (2.22). The curvature factor C is

$$C = \frac{|\,\mathrm{Ai}\,(\Delta \exp[2\pi i/3])\,|^{-2}}{4\pi\,|\Delta|^{1/2}} \quad . \qquad (2.24)$$

where

$$\Delta = (k_1 \rho / 2 \sin^2\alpha_i)^{2/3}\,(\cos^2\alpha_c - \cos^2\alpha_i) \qquad (2.25)$$

$$k_1 = 2\pi n_1/\lambda \qquad (2.26)$$

and λ is the wavelength in vacuum, ρ is the radius of the curvature in the plane of incidence. The modulus of the Airy function $|\,\mathrm{Ai}\,(\Delta \exp[2\pi i/3])|^{-2}$ is

a smooth decreasing function of Δ. Further details and tables of Airy functions are found in reference [12]. The expressions for T given by (2.23) is uniformly valid on either side of the critical angle. They simplify for the several cases of practical interest to be discussed next

1. $\alpha_i < \alpha_c$

When the angle of the incidence α_i is less than the critical angle α_c, Fresnel's classical expression for T is given by (2.22). Because when $-\Delta >> 1$, $C \approx 1$, (2.23) reduces to (2.22). In other words, when the interface is curved, Fresnel's law for $\alpha_i \leq \alpha_c$ fail for angles of incidence too close to the cririca angle.

2. $\alpha_i = \alpha_c$

For angles of incidence close to the critical angle, the classical Fresnel's law gives T = 0. However, a good approximation to T is to set $\alpha_i \approx \alpha_c$ in (2.23). then, from (2.22c), (2.23), (2.24) and (2.25)

$$T^E \equiv T^H \sin^2 \alpha_c \equiv \frac{1}{\pi \cos\alpha_c} \left(\frac{2 \sin^2\alpha_c}{k_1\rho}\right)^{1/3} \left| \text{Ai}\left(\Delta \exp[2\pi i/3]\right) \right|^{-2} \quad . \qquad (2.27)$$

3. $\alpha_i > \alpha_c$

When $\alpha_i > \alpha_c$ and not too close to α_c, $\theta_i = \pi/2 - \alpha_i$ and $\theta_c = \pi/2 - \alpha_c$ (where $\theta_i, \theta_c << 1$) are defined, and for $n_1 \approx n_2$

$$T^E = T^H \equiv 4(\theta_i/\theta_c)\left(1 - \theta_i^2/\theta_c^2\right)^{1/2} \exp[-2/3\, k_1\rho\, (\theta_c^2 - \theta_i^2)^{3/2}]. \qquad (2.28)$$

Note that the modulus of T^E for $\alpha_i > \alpha_c$ has an imaginary numerator and a complex denominator.

2.4.3 Interface with Convex Curvature

The results above apply only to the concave curvature. There is no tunneling when the curvature is convex, thus Fresnel's coefficients given by (2.22) provide a suitable approximation.

2.4.4 Case of $n_2 > n_1$

When the index of refraction of medium 2 is greater than medium 1, there is no tunneling and Fresnel's coefficients (2.22) are again a suitable approximation. For our computer modeling of light propagation in a hollow core fiber, it is the case of $n_2 > n_1$, so that electromagnetic tunneling need not be considered..

In this chapter basic geometric optics for light propagation in optical fibers have been introduced. Geometric optics analysis is seen to be simple; however, it is inapplicable of modelling single mode fibers and is unable to characterize wavelength, interference, or polarization effects in multimode fibers. Electromagnetic theory is considered universally applicable. However, exact calculations are extremely complicated, so many simplifying approximations are necessary for practical applications.

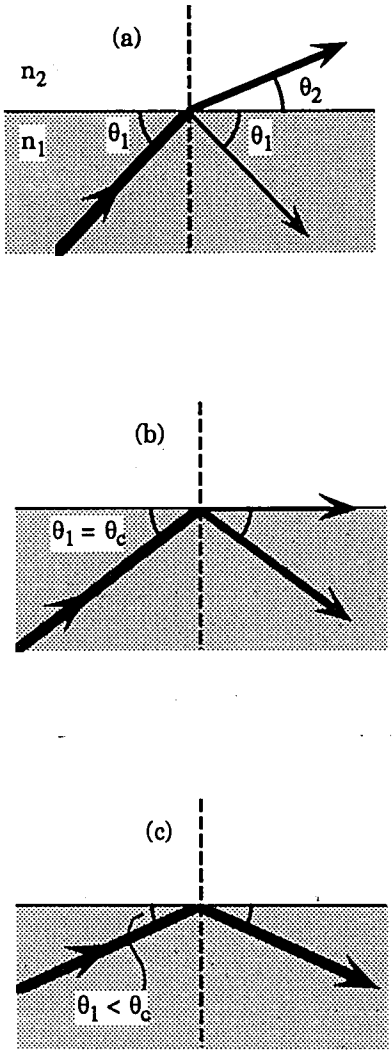

Figure 2.1 Ray incident at a plane interface between a low and high index medium.

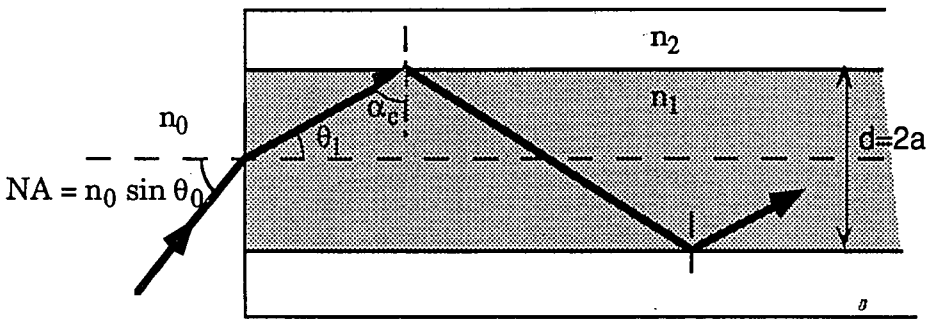

Figure 2.2. Numerical aperture, core size, ray passage along a optical fiber.

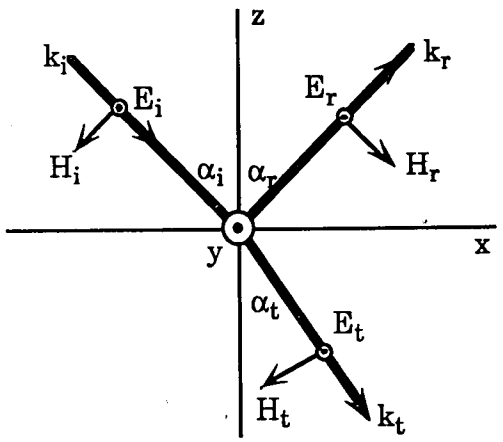

Figure 2.3a. Reflection and refraction of light incident on an interface in the TM polarization state.

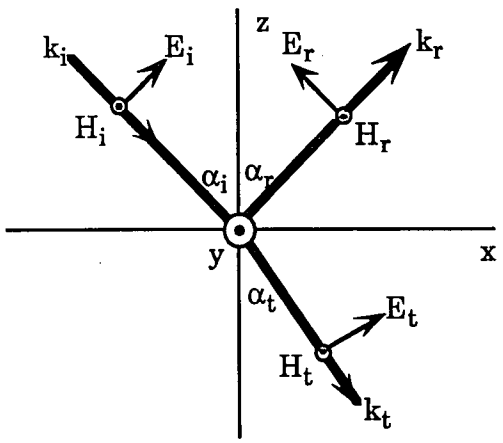

Figure 2.3b. Reflection and refraction of light incident on an interface in the TE polarization state.

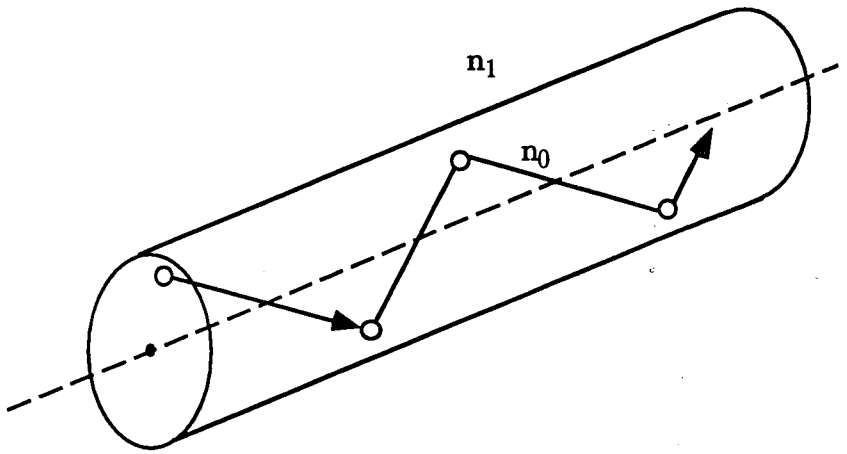

Figure 2.4(a) Passage of a skew ray along a straight circular dielectric cylinder.

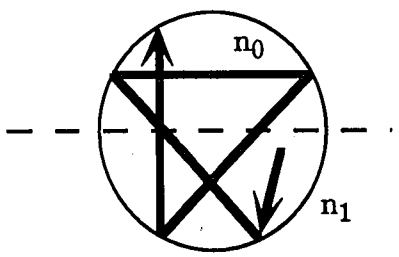

Figure 2.4(b) Helical path traversed by the skew ray.

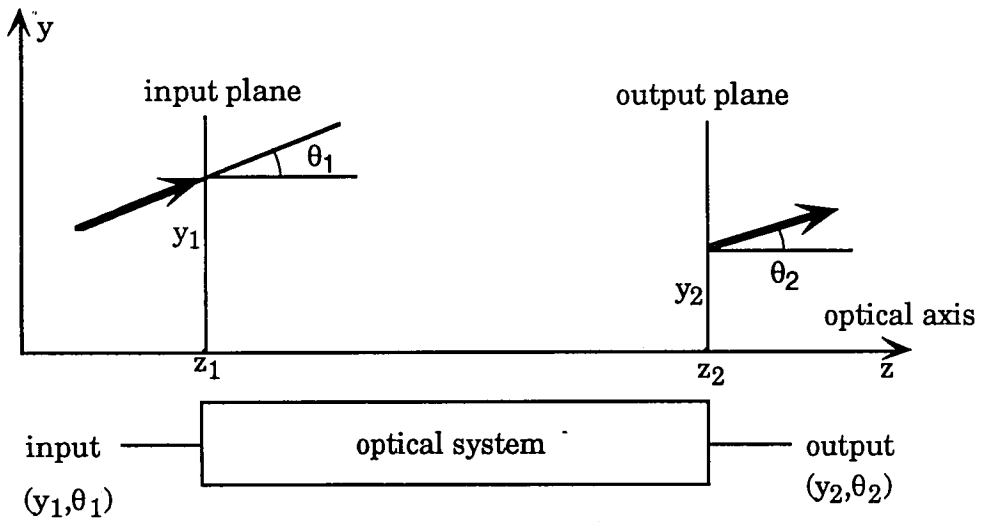

Figure 2.5. An optical system.

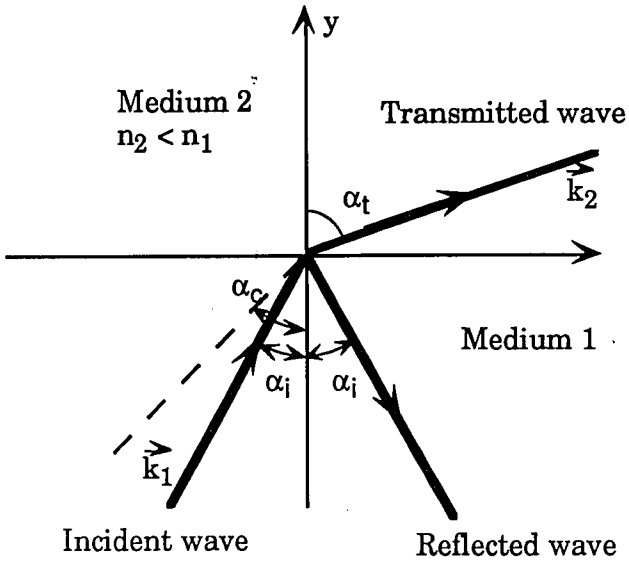

Figure 2.6. Plain wave reflection from a plane interface between two nonabsorbing media of indices of refraction n_1 and n_2. The wave vectors in media 1 and 2 are $\vec{k}_1$ and k_2, respectively. The plane of incidence is defined by $\vec{k}_1$ and the normal (y axis). $\vec{k}_2$ lies in the plane of incidence. The figure illustrates a wave undergoing refraction. α_c is the critical angle.

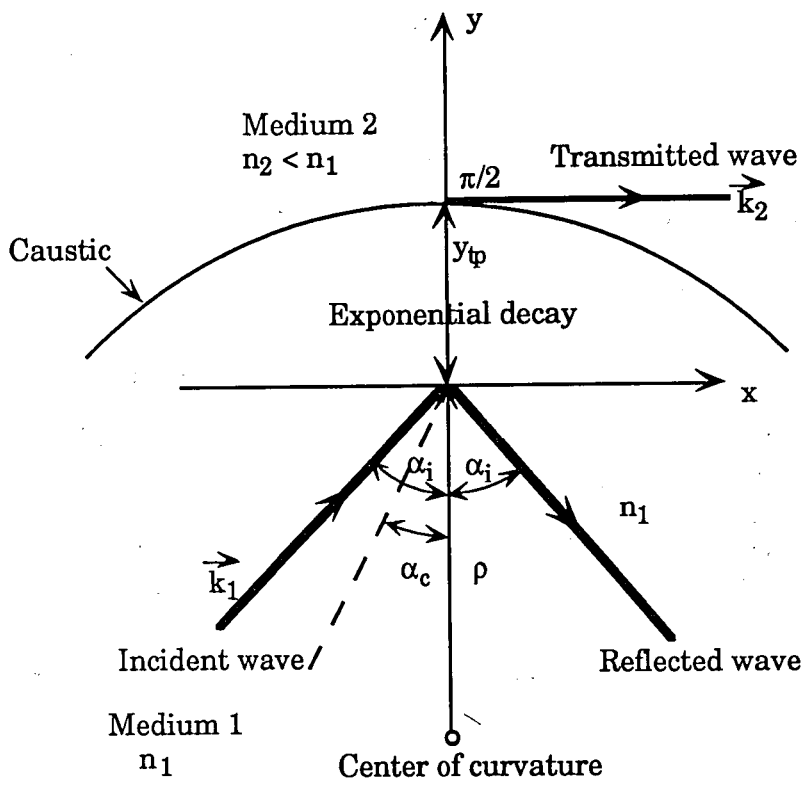

Figure 2.7. Reflection from a curved interface between two nonabsorbing media. When $\alpha_i > \alpha_c$, the transmitted wave originates tangent to the caustic at $y = y_{tp} = \rho\{(\sin\alpha_i/\sin\alpha_c) - 1\}$. The radius of curvature in the plane formed by the normal to the interface and the incident wave direction $\vec{k}_1$ is called ρ.

3. Wave Optics Representation

The wave theory of light encompasses the ray theory. Strictly speaking, ray optics is the limit of wave optics when the wavelength is infinitesimally short. However, the wavelength need not actually be equal to zero for the ray-optics theory to be useful. As long as the light waves propagate through and around objects whose dimensions are much greater than the wavelength, the ray theory suffices for describing most phenomena.

To attain a more detailed and correct understanding of the optical power propagation mechanism in a fiber, however, it is necessary to solve Maxwell's equations subject to the cylindrical boundary conditions of the fiber. First we will derive the wave equation in cylindrical coordinates from Maxwell's equations. Afterwords, the modal equations relevant to step index optical fibers will be developed.

3.1 Maxwell's equations

The general form of Maxwell's equations in a source-free region can be written as follows:

$$\nabla \times \vec{E} = -\frac{\partial \vec{B}}{\partial t} \tag{3.1}$$

$$\nabla \times \vec{H} = \frac{\partial \vec{D}}{\partial t} \tag{3.2}$$

$$\nabla \cdot \vec{D} = 0 \tag{3.3}$$

$$\nabla \cdot \vec{B} = 0 \tag{3.4}$$

where $\vec{D} = \varepsilon \vec{E}$ and $\vec{B} = \mu \vec{H}$. The parameter ε is the permitivity and μ is permeability of the medium.

Taking the curl of Eq. (3.1) and making use of Eq. (3.2) yields

$$\nabla \times (\nabla \times \vec{E}) = -\mu \frac{\partial}{\partial t}(\nabla \times \vec{H}) = -\varepsilon \mu \frac{\partial^2 \vec{E}}{\partial t^2} \ . \tag{3.5}$$

Using the vector identity

$$\nabla \times (\nabla \times \vec{E}) = \nabla(\nabla \cdot \vec{E}) - \nabla^2 \vec{E} \ ,$$

and using Eq. (3.3), Equation (3.5) becomes

$$\nabla^2\vec{E} = \varepsilon\mu\frac{\partial^2\vec{E}}{\partial t^2} \quad . \tag{3.6}$$

Similarly, by taking the curl of Eq. (3.2), it can be shown that

$$\nabla^2\vec{H} = \varepsilon\mu\frac{\partial^2\vec{H}}{\partial t^2} \quad . \tag{3.7}$$

Equations (3.6) and (3.7) are the standard *vector wave equations.*

3.2 Cylindrical Waveguide Equation

Consider plane electromagnetic waves propagating along the cylindrical fiber shown in Figure 3.1. For this fiber a cylindrical coordinate system $\{r,\phi,z\}$ is defined with the z-axis lying along the axis of the waveguide. If the electromagnetic waves are to propagate along the z-axis, they will have a functional dependence of the form

$$\vec{E} = \vec{E}_0(r,\phi)\, e^{j(\omega t-\beta z)} \tag{3.8}$$

$$\vec{H} = \vec{H}_0(r,\phi)\, e^{j(\omega t-\beta z)} \tag{3.9}$$

which are harmonic in time t and coordinate z. The parameter β is the z component of the propagation vector and will be determined by the boundary condition on the electromagnetic fields at the core-cladding interface.

When Eqs. (3.8) and (3.9) are substitute d into Maxwell's curl equations, we have, from Eq. (3.1),

$$\frac{1}{r}\{\frac{\partial E_z}{\partial\phi} + jr\beta E_\phi\} = -j\omega\mu H_r \tag{3.10}$$

$$j\beta E_r + \frac{\partial E_z}{\partial r} = j\omega\mu H_\phi \tag{3.11}$$

$$\frac{1}{r}\{\frac{\partial}{\partial\phi}(rE_\phi) - \frac{\partial E_r}{\partial\phi}\} = -j\omega\mu H_z \tag{3.12}$$

and from Eq.(3.2)

$$\frac{1}{r}\{\frac{\partial H_z}{\partial \phi} + jr\beta H_\phi\} = j\varepsilon\omega E_r \tag{3.13}$$

$$j\beta H_r + \frac{\partial H_z}{\partial r} = -j\varepsilon\omega E_\phi \tag{3.14}$$

$$\frac{1}{r}\{\frac{\partial}{\partial \phi}(rH_\phi) - \frac{\partial H_r}{\partial \phi}\} = j\varepsilon\omega E_z \tag{3.15}$$

By eliminating variables these equations can be rewritten such that, when Ez and Hz are known, the remaining transverse components Er, Eϕ, Hr, and Hϕ can be determined. Doing so yields

$$E_r = -\frac{j}{q^2}\{\beta\frac{\partial Ez}{\partial r} + \frac{\mu\omega}{r}\frac{\partial Hz}{\partial \phi}\} \tag{3.16}$$

$$E_\phi = -\frac{j}{q^2}\{\frac{\beta}{r}\frac{\partial Ez}{\partial \phi} - \mu\omega\frac{\partial Hz}{\partial r}\} \tag{3.17}$$

$$Hr = -\frac{j}{q^2}\{\beta\frac{\partial Hz}{\partial r} - \frac{\mu\omega}{r}\frac{\partial Ez}{\partial \phi}\} \tag{3.18}$$

$$H\phi = -\frac{j}{q^2}\{\frac{\beta}{r}\frac{\partial Hz}{\partial \phi} + \mu\omega\frac{\partial Ez}{\partial r}\} \tag{3.19}$$

where $q^2 = \omega^2\varepsilon\mu - \beta^2 = k^2 - \beta^2 = k0^2 n^2 - \beta^2$. Here k_0 is the free space wave number, determined by $2\pi/\lambda_0$, where λ_0 is the free space wavelength of the optical radiation; $n = n_1$ in the core and $n = n_2$ in the cladding, and β is the modal propagation constant. At the outset we will note that β is restricted in its value by the wave number in the core and cladding; that is

$$n_1 k_0 \geq \beta \geq n_2 k_0. \tag{3.20}$$

Substitution of Eqs. (3.18) and (3.19) into Eq. (3.15) results in the wave equation in cylindrical coordinates

$$\frac{\partial^2 E_z}{\partial r^2} + \frac{1}{r}\frac{\partial E_z}{\partial r} + \frac{1}{r^2}\frac{\partial^2 E_z}{\partial \phi^2} + q^2 E_z = 0 \quad , \tag{3.21}$$

and substitution of Eqs. (3.16) and (3.17) into Eq. (3.12) leads to

$$\frac{\partial^2 H_z}{\partial r^2} + \frac{1}{r}\frac{\partial H_z}{\partial r} + \frac{1}{r^2}\frac{\partial^2 H_z}{\partial \phi^2} + q^2 H_z = 0 \quad . \tag{3.22}$$

If the boundary conditions do not lead to coupling between the field components, mode solutions can be obtain in which either $E_z = 0$ or $H_z = 0$. When $E_z = 0$ the modes are called transverse electric or TE modes, and when $H_z = 0$ transverse magnetic or TM modes. Hybrid modes exist if both E_z and H_z are nonzero. These are designated as HE or EH modes, depending on whether H_z or E_z, respectively, makes a larger contribution to the transverse field.

3.3 Wave Equations for Step-Index Optical Fibers

We may use the above results to find the guided modes in a step-index fiber. A standard mathematical procedure for solving equations such as Eq. (3.21) is to use the separation-of-variables method, which assumes a solution of the form

$$E_z = F_1(r)\, F_2(\phi)\, F_3(z)\, F_4(t) \quad . \tag{3.23}$$

As was already assumed, the time and z dependent factors are given by

$$F_3(z)F_4(t) = e^{j(\omega t - \beta z)} \tag{3.24}$$

since the wave is sinusoidal in time and propagates in the z direction. In addition, because of the circular symmetry of the waveguide, each field

component must not change when the coordinate ϕ is increased by 2π. We thus assume a periodic function of the form

$$F_2(\phi) = C\, e^{j\nu\phi} \tag{3.25}$$

The constant ν can be positive or negative, but it must be an integer since the fields must be periodic in ϕ with a period of 2π.

Substituting Eq. (3.24) into Eq. (3.23) the wave equation (3.21) for E_z becomes

$$\frac{\partial^2 F_1}{\partial r^2} + \frac{1}{r}\frac{\partial F_1}{\partial r} + \left(q^2 - \frac{\nu^2}{r^2}\right) F_1 = 0 \tag{3.26}$$

which is the well-known differential equation for Bessel functions. An identical equation can be derived for H_z.

Equation (3.26) is a form of Bessel's equation, having several independent solutions. The choice of which solutions apply depends on the fact that fields must be finite everywhere and must die to zero as r goes to infinity. The outcome of these physical arguments for the cases where $q^2 > 0$ (core) and $q^2 < 0$ (cladding) results in the combined solution of (3.21):

$$E_z = \begin{cases} A\, J_l(ur/a) \begin{pmatrix} \sin l\phi \\ \cos l\phi \end{pmatrix} & r<a \\ B\, K_l(wr/a) \begin{pmatrix} \sin l\phi \\ \cos l\phi \end{pmatrix} & r>a \end{cases} \tag{3.27}$$

where

$$u = k_0\, a\, [n_1^2 - (\beta/k_0)^2]^{1/2} \tag{3.28}$$

$$w = k_0\, a\, [(\beta/k_0)^2 - n_2^2]^{1/2} \tag{3.29}$$

and a is the fiber core radius. J_l is the Bessel function of the first kind, and K_l is the modified Bessel function of the second kind, both of order l. Either the sine or the cosine term can be chosen.

Similarly, for H_z we have

$$H_z = \begin{cases} C\, J_l(ur/a) \begin{pmatrix} -\cos l\phi \\ \sin l\phi \end{pmatrix} & r<a \\ D\, K_l(wr/a) \begin{pmatrix} -\cos l\phi \\ \sin l\phi \end{pmatrix} & r>a \ . \end{cases} \tag{3.30}$$

It can be shown that the signs of the ϕ dependent terms which appear in (3.30) are demanded by boundary conditions and the orthogonal relation between E_z and H_z. Unknown amplitude coefficients A, B, C, D, and unknown β are left; the solutions for β will be determined by the boundary conditions.

Boundary conditions require that the tangential components of the electric and magnetic fields be continuous at r = a. This means

$$\begin{array}{ccc} \underline{r<a} & & \underline{r>a} \\ E_z \mid_{r=a} & = & E_z \mid_{r=a} \\ E_\phi \mid_{r=a} & = & E_\phi \mid_{r=a} \\ H_z \mid_{r=a} & = & H_z \mid_{r=a} \\ H_\phi \mid_{r=a} & = & H_\phi \mid_{r=a} \end{array} \tag{3.31}$$

E_ϕ and H_ϕ are evaluated using the relations

$$E\phi = -\frac{j}{q^2}\left[\frac{\beta}{r}\frac{\partial Ez}{\partial \phi} - \mu_0\omega\frac{\partial Hz}{\partial r}\right] \tag{3.32}$$

$$H\phi = -\frac{j}{q^2}\left[\omega\varepsilon_0 n^2\frac{\partial Ez}{\partial r} + \frac{\beta}{r}\frac{\partial Hz}{\partial \phi}\right] \tag{3.33}$$

which result from Maxwell's equations. Here ε_0 and μ_0 are the free space permittivity and permeability, respectively.

Equations (3.31) comprise a set of four simultaneous equations, which have a nontrivial solution provided that the determinant of these coefficients is zero. This determinant is usually expanded to form the characteristic or eigenvalue equation. It will be found that only discrete values restricted to the range given by Eq. (3.20). If the approximation of weak guidance is made, simplify can be considered. Specifically, if it is assumed that core and cladding indices are approximately equal, that is $n_1 \approx n_2$, or equivalently $\Delta = \frac{n_1^2 - n_2^2}{2n_1^2} \approx \frac{n_1 - n_2}{n_1} \ll 1$, then the characteristic equation takes the form

$$\frac{J_l(u)}{u\, J_{l-1}(u)} + \frac{K_l(w)}{w\, K_{l-1}(w)} = 0 \qquad l = 0, 1, 2,.... \tag{3.34}$$

Solutions to (3.31) for β are generally derived numerically, with multiple values of β satisfying the equation for a given value of l and a given set of fiber parameters n_1, n_2, a, and λ. For a given l value, there will be m roots of Eq. (3.34). These roots will be designated by β_{lm}, and the corresponding modes are either TE_{lm}, TM_{lm}, EH_{lm}, or HE_{lm}.

Figure 3.2 shows β plotted against the *normalized frequency* V, where

$$V = k_0\, a\, (n_1^2 - n_2^2)^{1/2} \quad . \tag{3.35}$$

This parameter is connected with the cut-off condition and a dimensionless number that determines how many modes a fiber can support. Another parameter called *normalized propagation constant* b may represent the number of modes more conveniently:

$$b = \frac{a^2 w^2}{V^2} = \frac{(\beta/k)^2 - n_2^2}{n_1^2 - n_2^2} \tag{3.36}$$

From the Figure 3.2, each mode can exist only for values of V that exceed a certain limiting value. The modes are cut off when $\beta/k = n_2$. The HE_{11} mode has no cut off as long as the core diameter is not zero.

When the field which result from the solution of equation (3.34) are expressed in rectangular components, it is seen that the electric field is either directed along x or along y, meaning they are linearly polarized. For this reason, these modes are generally referred to as LP_{lm} modes.

Finally general field expressions for the transverse components x and y can be written as

$$\vec{E}_t = \begin{cases} A_{lm} \dfrac{J_l(u_{lm}r/a)}{J_l(u_{lm})} \begin{pmatrix} \sin l\phi \\ \cos l\phi \end{pmatrix} \exp[j(wt - \beta_{lm}z + \psi_{lm})] \begin{pmatrix} \vec{a}_x \\ \vec{a}_y \end{pmatrix} & r<a \\ A_{lm} \dfrac{K_l(w_{lm}r/a)}{K_l(w_{lm})} \begin{pmatrix} \sin l\phi \\ \cos l\phi \end{pmatrix} \exp[j(wt - \beta_{lm}z + \psi_{lm})] \begin{pmatrix} \vec{a}_x \\ \vec{a}_y \end{pmatrix} & r>a \end{cases} \quad (3.27)$$

The parameter V can also be related to the number of modes M in a multimode fiber when M is large. An approximate relationship for the number of modes which may propagate in a step-index fibers can be derived from ray theory. The total number of modes M entering the fiber is thus given by [R]

$$M \approx \frac{2\pi^2 a^2}{\lambda^2}(n_1^2 - n_2^2) = \frac{V^2}{2} \quad . \quad (3.37)$$

For electromagnetic radiation of wavelength λ emanating from a laser or a waveguide, the number of modes per unit solid angle is given by $2S/\lambda^2$. where S is the area which the mode is leaving or entering. For the fiber, $S = \pi a^2$, and the solid acceptance angle for the fiber is $\Omega = \pi\theta^2 = \pi(\sin\theta)^2 = \pi(n_1^2 - n_2^2)$ for a small θ.

Solving the Maxwell's equations to get the electric field distributions will be a strict and accurate way to predict the mechanisms of the light propagation in the fiber. To model the propagation of light can be realized by solving the characteristics equation, superpose every solution. It is obvious that this method will be very complicated and huge amount of the numerical calculations. However, it is well known that geometric optics provides an approximate description of light propagation in regions where the refractive

index varies only slightly over a distance comparable to the wavelength of light. It will be seen that the ray optics is much easier to be used to model the power distributions in the multimode optical fibers.

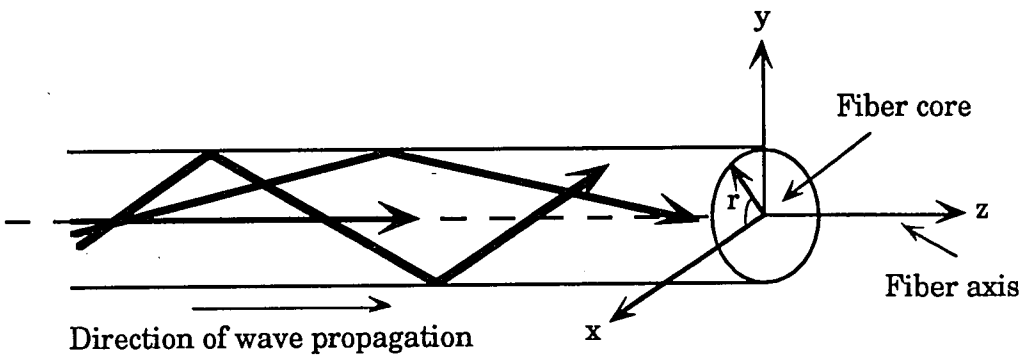

Figure 3.1 Cylindrical coordinate system used for analyzing electromagnetic wave propagation in an optical fiber.

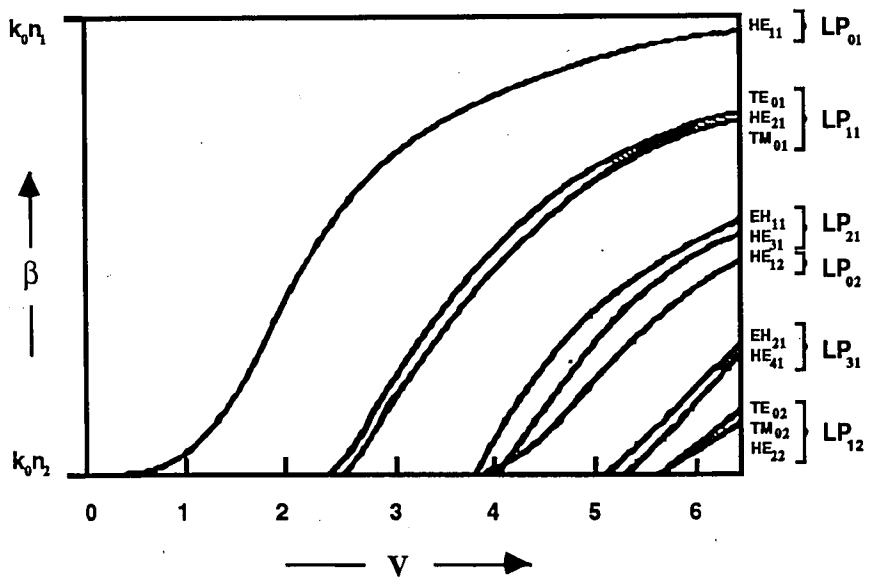

Figure 3.2 Propagation constant versus the normalized frequency V for the first several modes. Shown are the vector modes and their corresponding LP mode designations.

4. The Gaussian Beam

The Gaussian Beam is a solution of the paraxial Helmholtz equation which is the slowing varying envelope approximation of the Helmhotz equation. For a single-mode fiber, the fundamental fiber mode will be transformed into the fundamental Gaussian beam mode when the wave is radiated from the fiber end [18]. Since the Gaussian beam is well known, thus single-mode fiber can be used for remote sensing system. In this chapter, we will review some properties of the Gaussian beam and summarize the different definitions of the spot size of the single mode fibers.

4.1 Paraxial Waves

A wave is said to be paraxial if its wavefront normals are paraxial rays. One way of constructing a paraxial wave is to start with a plane wave A exp (-jkz), regard it as a "carrier" wave, and modify or "modulate" its complex envelope A, making it a slowlyvarying function of position $A(\vec{r})$. In this way, the complex amplitude of the modulated wave becomes

$$U(\vec{r}) = A(\vec{r}) \exp(-jkz). \tag{4.1}$$

The variation of $A(\vec{r})$ with position must be slow within the distance of a wavelength $\lambda = 2\pi/k$, so that the wave approximately maintains its underlying plane-wave nature.

4.1.1 Complex Amplitude of Gaussian Beams

The concept of paraxial waves was introduced above. The complex amplitude is shown in Eq. (4.1). The envelope is assumed to be approximately constant within a neighborhood of size λ, so that the wave is locally like a plane wave with wavefront normals that are paraxial rays.

For the complex amplitude $U(\vec{r})$ to satisfy the Helmholtz equation,

$\nabla^2 U + k^2 U = 0$, the complex envelope $A(\vec{r})$ must satisfy the paraxial Helmholtz equation

$$\nabla_T^2 A - j2k\frac{\partial A}{\partial z} = 0 \tag{4.2}$$

where $\nabla_T^2 = \partial^2/\partial x^2 + \partial^2/\partial y^2$ is the transverse part of the Laplacian operator. One simple solution to the paraxial Helmholtz equation provides the paraboloidal wave for which

$$A(\vec{r}) = \frac{A_1}{z}\exp(-jk\rho/2z) \quad , \tag{4.3}$$

where A_1 is a constant and $\rho = x^2 + y^2$. The paraboloidal wave is the paraxial approximation of the spherical wave $U(r) = (A_1/r)\exp(-jkr)$ when x and y are much smaller than z.

Another solution of the paraxial Helmholtz equation provides the Gaussian beam. It is obtained from the paraboloidal wave by use of a simple transformation. Since the complex envelope of the paraboloidal wave (4.3) is a solution of the paraxial Helmholtz equation (4.2), a shifted version of it, with $z - \xi$ replacing z where ξ is a constant,

$$A(\vec{r}) = \frac{A_1}{q(z)}\exp(-jk\rho/2q(z)) \quad , \tag{4.4}$$

is also a solution, where $q(z) = z - \xi$. This provides a paraboloidal wave centered about the point $z = \xi$ instead of $z = 0$. When ξ is complex, (4.4) remains a solution of (4.2), but it acquires dramatically different properties. In particular, when ξ is purely imaginary, say $\xi = -jz_0$ where z_0 is real, (4.4) gives rise to the complex envelope of the Gaussian beam

$$A(\vec{r}) = \frac{A_1}{q(z)}\exp(-jk\rho/2q(z)) \quad , \tag{4.5}$$

the parameter z_0 is known as the Rayleigh range, where $q(z) = z - jz_0$.

To separate the amplitude and phase of this complex envelope, we write the complex function $1/q(z) = 1/(z+jz_0)$ in terms of its real and imaginary parts by defining two new real functions R(z) and W(z), such that

$$\frac{1}{q(z)} = \frac{1}{R(z)} - j\frac{\lambda}{\pi W^2(z)} \tag{4.6}$$

It will be shown that W(z) and R(z) are measures of the beam width and wavefront radius of curvature, respectively. Expressions of W(z) and R(z) as functions of z and z_0 are provided below. Substituting (4.6) into (4.5) and using (4.1), an expression for the complex amplitude $U(\vec{r})$ of the Gaussian beam is obtained:

$$U(\vec{r}) = A_0\frac{W_0}{W(z)}\left[\exp(-\frac{\rho^2}{W^2(z)})\right]\exp\left(-jkz - ik\frac{\rho^2}{2R(z)} + j\xi(z)\right) \tag{4.7}$$

where

$$W(z) = W_0\,[1 + (z/z_0)^2]^{1/2} \tag{4.8}$$

$$R(z) = z\,[1 + (z_0/z)^2] \tag{4.9}$$

$$\xi(z) = \tan^{-1}(z_0/z) \tag{4.10}$$

$$W_0 = (\lambda z_0/\pi)^{1/2}\ , \tag{4.11}$$

and a new constant $A_0 = A_1 / jz_0$ has been defined for convenience.

The expression for the complex amplitude of the Gaussian beam is central to this section. It contains two parameters, A_0 and z_0, which are determined from the boundary conditions. All other parameters are related to the Rayleigh range z_0 and the wavelength λ by (4.8) to (4.11).

4.1.2 Intensity

The optical intensity $I(\vec{r}) = |U(\vec{r})|^2$ is a function of the axial and radial distances z and $\rho = (x^2 + y^2)^{1/2}$,

$$I(\rho,z) = I_0\left[\frac{W_0}{W(z)}\right]^2\exp\left(-\frac{2\rho^2}{W^2(z)}\right) \tag{4.12}$$

where $I_0 = |A_0|^2$. At each value of z the intensity is a Gaussian function of the radial distance ρ. This is why the wave is called a Gaussian beam. The Gaussian function has its peak at ρ = 0 and drops monotonically with increasing ρ. The width W(z) of the Gaussian distribution increases with the axial distance z as illustrated in Figure 4.1.

On the beam axis (ρ = 0), the intensity

$$I(0,z) = I_0\left[\frac{W_0}{W(z)}\right]^2 = \frac{I_0}{1+(z/z_0)^2} \tag{4.13}$$

has its maximum value I_0 at z = 0 and drops gradually with increasing z, reaching half its peak value I_0 at $z = \pm z_0$ as illustrated in Figure 4.2. When $|z| >> z_0$, $I(0,z) \approx I_0 z_0^2/z^2$, so that the intensity decreases with the distance in accordance with an inverse-square law, as for spherical and paraboloidal waves. The overall peak intensity $I(0,0) = I_0$ occurs at the beam center (z = 0, ρ = 0).

4.2.3 Power

The total optical power carried by the beam is the integral of the optical intensity over a transverse plane

$$P = \int_0^\infty I(\rho,z)\, 2\pi\rho\, d\rho \quad ,$$

which gives

$$P = \frac{1}{2} I_0 \pi W_0^2 \quad . \tag{4.14}$$

The result is independent of z, since the beam power is one-half the peak intensity times the beam area (i.e., the total power is conserved along the propagation axis). Since beams are often described by their power P, it is useful to express I_0 in terms of P using (4.14) and rewrite (4.12) in the form

$$I(\rho,z) = \frac{2P}{\pi W^2(z)} \exp\left(-\frac{2\rho^2}{W^2(z)}\right) \tag{4.15}$$

The ratio of the power carried within a circle of radius ρ_o in the transverse plane at position z to the total power is

$$\frac{1}{P}\int_0^{\rho_0} I(\rho,z)\, 2\pi\rho d\rho = 1 - \exp\left(-\frac{2\rho_0^2}{W^2(z)}\right) . \tag{4.16}$$

The power contained within a circle of radius $\rho_0 = W(z)$ is approximately 86% of the total power. About 99% of the power is contained within a circle of radius 1.5W(z).

4.1.4 Beam Radius

Within any transverse plane, the beam intensity assumes its peak value on the beam axis, and drops by the factor $1/e^2 \cong 0.135$ at the radial distance $\rho = W(z)$. Since 86% of the power is carried within a circle of radius W(z), we regard W(z) as the beam radius (also called beam width). The r.m.s. width of the intensity distribution is $\sigma = 1/2W(z)$.

The dependence of the beam radius on z is governed by Eq. (4.8),

$$W(z) = W_0 \{ 1 + (z/z_0)^2 \}^{1/2} . \tag{4.17}$$

It assumes its minimum value W_0 in the plane $z = 0$, called the beam waist. Thus W_0 is the *waist radius*. The waist diameter $2W_0$ is called the *spot size*.

The beam radius increases gradually with z, reaching $\sqrt{2}\, W_0$ at $z = z_0$, and continues increasing monotonically with z (Figure 4.3). For $z >> z_0$ the first term of (4.17) may be neglected, resulting in the linear relation

$$W(z) \approx \frac{W_0}{z_0} z = \theta_0 z \tag{4.18}$$

where $\theta_0 = W_0/z_0$. Using (4.11), we can also write

$$\theta_0 = \frac{\lambda}{\pi W_0} \quad . \tag{4.19}$$

4.2 Gaussian Approximation of the Fundamental Mode

For simulating how light propagates in an optical fiber or for calculating the power launched into the fiber input end and losses at fiber connectors, one needs to know the radial amplitude distribution both in the core and in the cladding. In order to get simple formulas, it is important to find a simple approximation for the amplitude distribution of the elaectric field in the radial direction, $E(\rho)$, both in the core and in the cladding.

From the fact that the fundamental fiber mode appears to be similar to a free space Gaussian beam, one can conclude that a simple function to give a close approximation to the true amplitude distribution is a Gaussian function [13,14,15,16]:

$$E(\rho) \approx E_0 \exp\left[-\left(\frac{\rho}{w_G}\right)^2\right] \quad . \tag{4.20}$$

In Eq. (4.20), there is just one parameter to match the width of the approximate Gaussian field profile to the width of the true field profile; w_G is called the spot size or the field radius of the fundamental mode. The mode field diameter may be defined as two times the spot size [17]. For many refractive-index profiles and for typical operating wavelengths, the mode field diameter is slightly larger than the core diameter.

There are at least five definitions for the spot size. As will be explained later, one method often used to define the spot size is to consider the problem of launching the fundamental fiber mode by a Gaussian beam incident on the fiber input end. The waist of the Gaussian beam is assumed to be located at the fiber input face, and the axes of the beam end of the fiber to coincide. The power launched into the fundamental mode depends on the spot size w_0 of the Gaussian beam at its waist. The spot size w_G of the fundamental fiber mode is then defined as that spot size w_0 of the Gaussian beam which maximizes the launching effeciency.

The amplitude E_0 in the Gaussian approximation should be chosen in such a manner that the power transmitted by the substitute Gaussian field

equals the power transmitted by the true mode. The main advantage of using the Gaussian approximation for the radial amplitude distribution is that one does not have to specify two different functions in the core and in the cladding, but only one parameter, namely the spot size w_G.

For the fundamental mode guided by a multimode graded-index fiber with untruncated parabolic refractive-index profile with g = 2 for all ρ, the radial field distribution is described exactly by a Gaussian function [17]. For single mode fibers with homogeneous cladding, the true field distribution is never exactly Gaussian. Since the field decay in the cladding is more like an exponential function than like a Gaussian function, the Gaussian approximation underestimates the evanescent field in the cladding.

The Gaussian approximation is good for fibers operated at a wavelength near the cutoff wavelength of the second order mode. When the wavelength gets larger, the Gaussian approximation becomes less accurate.

4.3 The Spot Size of the Radial Field Distribution

For real fibers, the radial field distribution $E(\rho)$ is not strictly Gaussian and in general can only be calculated numerically from the refractive index profile or determined experimentally. For example, the radial field distribution in a step-index fiber is described in the core by the Bessel function $J_0(u\rho/a)$ and in the cladding by the modified Hankel function $K_0(w\rho/a)$, so that a Gaussian function only represents a useful approximation to the true radial field distribution.

The problem of defining a spot size for non-Gaussian field distributions is a difficult one, and at least eight definitions seem to exist [18], that is if we do not count the determination of the 1/2, 1/e, $1/e^2$ points as different. Depending on the problem in question, it turns out that one is led to different definitions for the field width.

Definitions proposed in the literature will be summarized. We introduce the five most important ones.

4.3.1 Simple Definition of the Spot Size

The simplest method for defining the width of the near-field is the following: the spot size W_s is that distance from the axis for which the amplitude of the true electric field is 1/e = 0.37 of its value on the fiber axis. At this distance, the intensity is $1/e^2 = 0.135$ of its maximum. Note that some authors use the 1/e-width of the intensity distribution instead, which for a Gaussian field distribution is 0.707 W_s.

It has been recognized that the simple 1/e-radius W_s of the electromagnetic field supplies too rough an approximation to the actual mode field radius and is not satisfactory for definition and specification purposes [19,20].

4.3.2 Spot Size Related to Launching

The launching problem was first analyzed by Marcuse [21]: A fundamental Gaussian beam mode in air is incident on the fiber input end. In order to launch as much power as possible into the fundamental mode of the fiber, it is first necessary to match the wavefronts. Since the wavefronts of LP_{01} mode are planes normal to the axis, the axis of the Gaussian beam must coincide with the fiber axis. Moreover, since the Gaussian beam has a plane wavefront only at its waist, the waist must located on the fiber input face. Under these conditions, the launching effeciency is given by the launch efficiency integral, which is essentially the square of the overlap integral [26]:

$$\eta = \frac{\{\int_0^\infty E(\rho)E_G(\rho)\rho d\rho\}^2}{\int_0^\infty E^2(\rho)\,\rho\,d\rho \int_0^\infty E_G^2(\rho)\rho d\rho} \quad . \tag{4.21}$$

In the integrals, the function $E(\rho)$ is the true radial field amplitude distribution of the fundamental mode to be launched and

$$E_G(\rho) = E_0 \exp[-(\rho/W_0)^2] \tag{4.22}$$

is the radial field distribution of the Gaussian beam in the waist at z = 0. The parameter W_0 is the spot size at the waist of the Gaussian beam.

The launching effeciency clearly depends on the spot size W_0. For a certain value of W_0, the launching effeciency becomes a maximum, i.e.

$$\frac{d\eta}{dW_0} = 0, \qquad \text{for } W_0 = W_G \quad .$$

This optimum spot size W_G of the incident Gaussian beam is the second measure proposed to define the spot size of the fundamental fiber mode [22,23]. The subscript "G" is intended to remind us that launching is by a Gaussian beam. The spot size w_G of the Gaussian beam which would optimally excite the fundamental fiber mode is not equal to the simple 1/e width W_s of the fundamental mode.

4.3.3 Spot Size Related to Microbending Losses

For analyzing microbending losses in single-mode fibers, Petermann [24,25] introduced a third kind of spot size W_e by the definition

$$w_e^2 = \frac{2\int_{\infty}^{0} E^2(\rho)\rho^2\rho d\rho}{\int_{\infty}^{0} E^2(\rho)\,\rho\, d\rho} \quad . \tag{4.23}$$

Since Petermann also defined other spot sizes (4.24), W_e sometimes is called the Petermann I spot size.

The integrals in this definition have simple meanings: the integral in the denominator is proportional to the power transmitted by the fundamental mode. In the integral in the numerator, the square of the distance ρ from the fiber axis is weighted by the square of the electric field strength, i.e. by the mode intensity. Thus, we represents the root-mean-square (rms) or effective value of ρ, as indicated by the subscript "e".

Alternatively, the spot size W_e can be regarded as representing the second moment of the near-field intensity distribution [26].

Not only microbending losses, but also losses due to small tilts, i.e. angular misalignment, depend on the effective spot size [20]. Low tilt losses thus require small values of W_e [27].

4.3.4 Spot Size Related to Waveguide Dispersion

When analyzing waveguide dispersion D_w, which is expressed by

$$D_w = -\left(\frac{n_1-n_2}{\lambda c}\right) V \frac{d^2(Vb)}{dV^2}, \tag{4.24}$$

Petermann defined a fourth, "strange" kind of spot size [32]:

$$W_d^2 = \frac{2\int_0^\infty E^2(\rho)\rho d\rho}{\int_0^\infty (dE/d\rho)^2 \rho d\rho} \tag{4.25}$$

The subscript "d" indicates "dispersion" or the "derivitive" of the radial field distribution in the denominator. This spot size is the inverse of the rms-value of the relative slope $(dE/d\rho)/E$ of the radial near-field distribution $E(\rho)$. The quantity w_d is called the Petermann II spot size.

On carring out the integral in the denominator by parts the square of the first derivative is replaced by the transverse Laplace operator [28]. Some authors [29] call w_d the "Laplace spot size".

3.4.5 Spot Size Related to Transverse Offset Loss

Streckert introduced the transverse offset method for measuring the spot size. The theory underlying this measuring method can also be used to define a fifth kind of spot size, w_a [30].

The power transmission function $\eta(s,\phi_s)$ for a butt joint with a transverse axis offset is:

$$\eta(s,\phi_s) = \left(\frac{\int_0^{2\pi} \int_0^{\infty} E(\rho,\phi)E(\rho',\phi')\rho d\rho d\phi}{\int_0^{2\pi} \int_0^{\infty} E^2(\rho,\phi)\rho d\rho d\phi} \right)^2 \tag{4.26}$$

where s is the transverse offset with azimuth ϕ_s depicted in Figure 4.4. The variables ρ' and ϕ' are related to the variables of integration ρ and ϕ by the two equations

$$\rho'^2 = \rho^2 + s^2 - 2\rho s \cos(\phi - \phi_s) \quad , \tag{4.27}$$

and

$$\tan\phi' = \frac{\rho \sin\phi - s \sin\phi_s}{\rho \cos\phi - s \cos\phi_s} \tag{4.28}$$

The overlap integral in the numerator of (4.26) is propotional to the amplitude transmission coefficient of the joint with transverse offset. In its integrand, the near-field amplitude distribution of the fundamental fiber mode is multiplied by a shifted version of the same field distribution. Thus the integral in the numerator represents the two-dimensional autocorrelation function of the near-field amplitude distribution. The normalized power transmission function $\eta(s,\phi_s)$ is propotional to the squared modules of the autocorrelation function.

Now, from the normalized power transmission function $\eta(s,\phi_s)$, the autocorrelation or mode field convolution spot size w_a is defined as that value of the transverse offset s, for which the power transmission is 1/e = 0.37 of its maximum value of unity at s = 0. For a circular near-field distribution, any direction ϕ_s of transverse offset can be taken.

We have discussed the properties of the Gaussian beam and definitions of the spot size of the radial field distributions only for single mode fibers. In our experiment, we used the concept of the spot size to measure the width of the radial power distributions for multimode optical fibers.

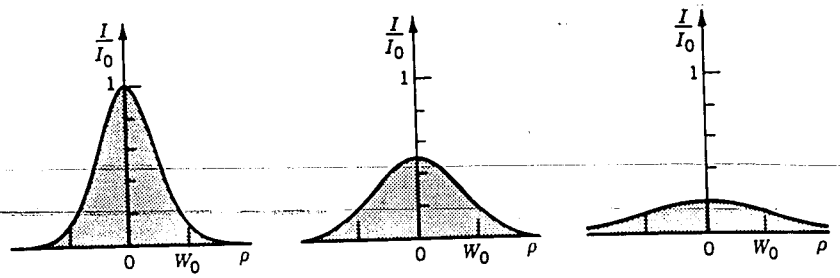

Figure 4.1. The normalized beam intensity I/I_0 as a function of the radial distance ρ at different axial distances: (a) $z = 0$; (b) $z = z_0$; (c) $z = 2z_0$.

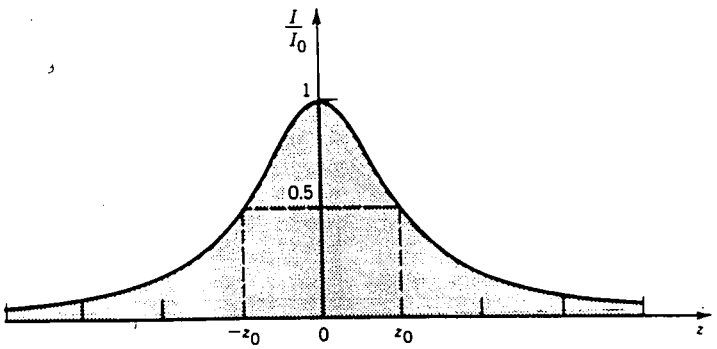

Figure 4.2. The normalized beam intensity I/I_0 at points on the beam axis ($\rho = 0$) as a function of z.

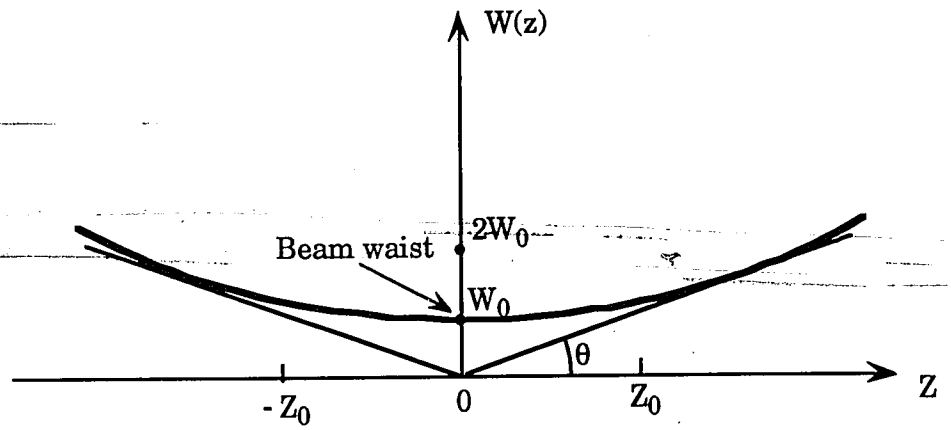

Figure 4.3 The beam radius W(z) has its minimum value W_0 at the waist (z = 0), reaches $\sqrt{2}\, W_0$ at $z = \pm z_0$, and increases linearly with z for large z.

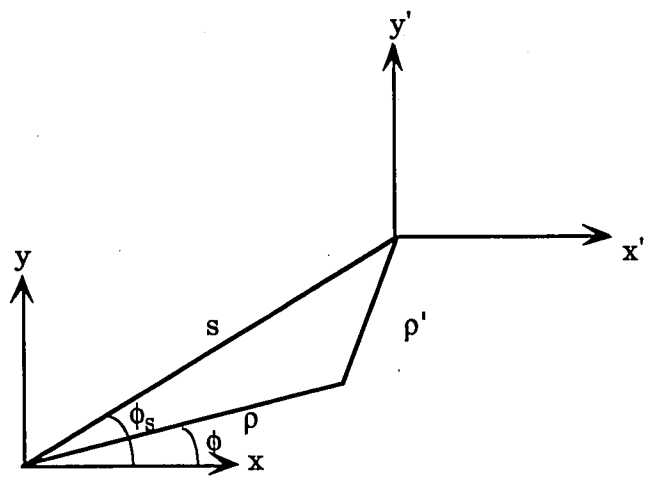

Figure 4.4. Coordinates used for calculating the near-field autocorrelation.

5. Ray Optics Model of Multimode Fiber

From splices in communications applications to sensing applications using fiber to fiber coupling, the ability to determine optical loss caused by fiber misalignments in butt joints is essential. There are several models which appear in the literature for calculating loss due to small angular and longitudinal misalignments in multimode fiber butt-joints. Unfortunately, there is often poor agreement between predicted and actual losses [31]. Actually the total effect of a splice in a multimode optical fiber system depends on how the splice is excited (input power distribution), how the splice couples light from one fiber to another ("local" splice characteristics), and how the splice affects the loss of the receiving fiber (length dependence). Losses in the receiving fiber are extremely difficult to calculate because the various loss and coupling coefficients of the individual modes in a multimode optical fiber are not known, and therefore the total effect of a splice in a multimode system is difficult to characterize accurately. Usually geometric optics models are generated to determine the various input contributors to splice loss so that fiber, connection, and system design can be optimized. These models are not useful for predicting losses for a given individual splice in the field with high accuracy because of the uncertainties mentioned previously.

Gloge and Marcatili showed in 1973 that if all the modes of a multimode fiber are equally exited, the power distribution across any local numerical aperture at any point on the core is uniform and the overall power distribution exiting the end of the fiber has the shape of the index profile for profile parameter g, discussed in the next section between 2 and infinity [31]. Several authors have assumed this power distribution as the basis for calculating splice loss [32-35]. Using this model, Miller calculated the splice loss caused by transverse offsets for both identical and diameter mismatched fibers and showed that these uniform power model calculations for identical parabolic fibers were highly inaccurate. The other authors also found these calculations inadequate for explaining observed splice losses. It appeared that the " uniform power" assumption was causing the discrepancies seen.

In this chapter, a new model is proposes, in which we assume a Gaussian power distribution to calculate the loss in multimode step-index fiber butt-joints. The model allows for large end separation distances and includes the effect of axial and angular misalignments, and when the splice is contained within a hollow core fiber, accounts for reflections from the hollow fiber walls. The approach to simulate the light with the Gaussian power distribution at the end of the fiber is based on the ray optics approximation. A meridional ray model was used, as this has been shown to be highly accurate in fibers where the power distribution is circularly symmetric [36].

5.1 General Properties of Fibers

Before the model is introduced, we would like to develop some of the general properties of fibers and light sources; these will be required to generate models and theories for calculating the loss caused by the axial displacement and the deflection of the hollow core fiber.

5.1.1 Refractive Index Profiles

General form of refractive index profile can be written as follow:

$$n(r) = n_1\left[\, 1 - 2\Delta\left(\frac{r}{a}\right)^g \,\right]^{1/2} \qquad (6.1)$$

where

$\Delta \approx (n_1 - n_2)/n_1$
n_1 = maximum index in the core
n_2 = index of the cladding
g = index profile parameter
a = fiber core radius

Figure 5.1 shows the index profile for several values of the profile parameter, g. The most commonly used values of g for multimode fibers are ~ 2 (parabolic graded-index fibers) and ∞ (step-index fibers). Triangular one is when g = 1. It is clear to see that triangular index profile

has sharper shape than graded index profile, and graded index profile has sharper shape than step index profile.

5.1.2 Point Sources

To simplify and generalize the concepts involved in hollow core deflection loss modeling for optical fibers from a geometric optics point of view, it is necessary to define a point light source. Since in this analysis only meridional rays are considered, so that every point source is on the diameter of the fiber, the position of each point source is only a function of r, the distance from the fiber axis. A ray is described by three characteristics: its position r, its angle θ with respect to the optical axis, and its power. The position and angle at the input and output planes of an optical system are related by two algebraic equations (given by the ray transfer matrix), and the ray maintains its power regardless of its position or angle. The matrix which stores information about the rays will obviously require three columns, one each for the ray position, angle, and power.

5.1.3 Local Numerical Aperture

Fiber with a core index of refraction which obeys equation (5.1) has a numerical aperture (NA) given by equation.

$$NA(r) \equiv n_1 (2\Delta)^{1/2} [1 - (r/a)^g]^{1/2} . \qquad (5.2)$$

This equation defines the local numerical aperture for any point on the core and clearly has the same shape as the index profile as a function of radius, decreasing monotonically from its maximum at the center of the core to zero at the core cladding boundary. The NA gives the acceptance angle for each point on the index-matched core, that is, the maximum angle θ with respect to the longitudinal axis of the fiber at which light rays can propagate and still be guided by total internal reflection. Any light entering the fiber at that point on the core at angles greater than θ_a = arc sin[NA(r)] is very rapidly lost through radiation or leaky modes. From an electromagnetic theory point of view, this means that all power is propagating in bound modes. If this condition is satisfied, each point in the

core of the transmitting fiber can be considered a point source with light distributed over the acceptance angle at that point.

5.1.4 Modal Power Distribution

To calculate hollow core deflection loss using a series of point sources along a core diameter, it is also necessary to know both the amount of power propagating in the transmitting fiber at each radial point on the core and how it is angularly distributed.

The angular distribution of the power is a function of both the modal power distribution in the fiber and the shape of the core index of refraction. In step-index ($g = \infty$) fibers, each mode can be uniquely represented by an angle of propagation in the core. The angular power distribution at any point is therefore directly related to the modal power distribution [31]. Since no unique ray angle is associated with each mode in a graded-index fiber, the angular power distribution there is not directly related to the modal power distribution. Another difference between step-index and graded-index fibers is that meridional rays have an outer turning point (caustic) in graded-index fibers but extend over the entire core in step-index fibers. These complexities in graded index fibers make it very difficult to actually measure the modal power distribution in these fibers and most geometric optics splice loss models and EM splice loss theories rely on using assumed modal power distributions [31].

5.2 General Approach of the Model

The most important feature of the model presented here is that the actual distribution of the light energy among the fiber modes is taken into account. Launching conditions and mechanical strain on the fiber will affect the modal distribution. The modal distribution, in turn, will affect how the energy is distributed across the fiber face and through the angles of emission. We consider only multimode fibers, so that the ray approximation can be used. In addition, the present analysis is restricted to step-index fiber, but could be extended to the graded-index core.

Consider an arbitrary point on the diameter (meridional rays approximation) of the core of the transmitting fiber (TF), as shown in

Figure 5.3. Using the ray approximation, a ray associated with any of the propagating modes can exit the fiber from this point at discrete angles to the surface normal. The angle at which a ray exits depends on the mode it represents, and all rays exit at an angle equal to or less than the maximum acceptance angle of the fiber. If we consider just one set of rays associated with a specific mode, and therefore a specific exit angle, rays can be thought of as a set of generators for two rays at the same angle (one with positive angle, the other with negative angle but the same value) whose apex lies at the point of exit on the diameter of the fiber face. Other modes leaving the fiber at the same point will exit with other angles relative to the propagation axis. Lower order modes will have smaller exit angles, while higher order modes will be associated with larger exit angles. If several of the propagating modes are included, a series of emission rays are generated. These rays can be calculated to represent the actual mode distribution in the fiber.

In our model, the concepts of the meridional rays and the ray transfer matrix were used. The ray positions and angles can be determined by dividing the available radius into *psteps* equal parts and maximun emitting angle into *asteps* equal parts. Also, *asteps* and *psteps* are integers, which control the resolution and can be changed by the user. The position and angle increments are defined by the number of steps: *pinc* = a/*psteps*, and *ainc* = θ_c/*asteps*, where a is the fiber radius, and θ_c is the maximum exit angle, calculated as $\sin^{-1}$(NA) and corresponding to the critical angle α_c of the step-index fiber. Each ray in the fiber is fixed by assigning it an exit position relative to the fiber axis which equals an integer value (positive or negative) times *pinc* and an exit angle relative to the fiber axis which equals an integer value (positive or negative) times *ainc*. Therefore the total number of sources is 2 *psteps* + 1, and at each source, the number of rays is 2 *ateps* + 1. Thus the total number of rays emerging from the fiber will be (2 *psteps* + 1) × (2 *ateps* + 1). Figures 5.4 (a) and (b) show the power distribution in free space 5 mm away from the emitting fiber end for two different values of *psteps*. It is obvious that choosing a larger number of *psteps* would lead to a smoother curve, although this at the expense of more computation time.

Therefore the positions and the angles could be positive or negative with respect to the optical axis. In the matrix, we define three parameters for

each ray, one is for the position called *r2(i,1)*, one is for the angle, *r2(i,2)*, and the third is for the power, *r2(i,3)*, where *i* is an integer between 1 and (2 *psteps* + 1) × (2 *ateps* + 1). The power variation at each position, which could be either the equal or the Gaussian power distribution, and is only a function of the exit angle, determined by the ray number *n* times *ainc*, which we call θ. The width of the power distribution is controlled by *ba*, so that the power *r2(i,3)* = exp (– (*ba* * *ainc* * n)^2), where *n* is the ray number. The relationship between the power and angle can be seen in Figure 5.5.

Similar to the angles, each position could also have either the equal or the Gaussian power distribution controlled by the width parameter *bp*. Hence the model can simulate a power distribution which is equal or Gaussian with respect to either the fiber diameter or the emission angle, or both. However, it was discovered that *bp* values other than 0 (that is, other than equal power distribution across the fiber face) lead to a non-Gaussian-like distribution of power in the far field. As an example, Figure 5.6 depicts the calculated power distribution at 5 mm from the fiber end with *bp* = 20. Since all fibers used in this research yielded Gaussian-like outputs, a *bp* value of 0 was used throughout the remainder of the modelling.

5.2.1 Radial Power Distribution

In the model, the power distribution at a certain distance from the fiber end can be calculated. The matrix *ffield* has (2 *xsteps* + 1) rows and 2 columns. The matrix variable *ffield(n,1)* holds the nth position in the far field at which the output power is calculated and *ffield(n,2)* holds the corresponding power. The resolution along the axis perpendicular to the propagation direction is limitted to (2 *xsteps* + 1) positions, where *xsteps* is an integer number which can be chosen by the user. Figure 5.7 shows the power distributions yielded by the model at different distances (d = 4 mm, 6 mm, 8 mm) when *ba* is equal to 15. It should also be noted that the choice of *xsteps* affects the smoothness of the curve representing the power distribution in the far field, although of course it will not affect the general shape of the curve. This is demonstrated in Figure 5.8, in which *xsteps* was set to 20, leading to the rough curve shown. In Figure 5.9, *xinc* = 20 is compared with *xinc* = 50, the latter of which leads to a smoother curve.

The radial power distribution was measured experimentally for a step-index multimode fiber with core/cladding diameter of 100/140 microns. Light was generated by an LED and captured by a photodetector. A 100 micron diameter pinhole was attached to the photodetector, which was mounted on a three axis micropositioner. The photodetector was first placed at a specified distance from the fiber end, as controled by z-axis positioner, the y-axis positioner was adjusted to find the maximum point of the power and then the power was measured every 100 microns by scanning the x-axis positioner radially across the circularly symmetric output pattern. The measured power distribution when the distance *d* from the fiber end was equal to 6 mm, 8 mm, and 10 mm appear in Figure 5.10.

Comparing the power distribution of the experimental data and the model, we found that they showed excellent agreement when the *ba* of the model is 14.5. That is, with this value of *ba*, the modelled power distribution spread out as a function of distance from the fiber end in a manner similar to the experimentally observed distribution. Figures 5.11, 5.12, and 5.13 show the power distribution curves of the model, the experimental data, and a Gaussian function curve fit with d = 6 mm, 8 mm, and 10 mm.

5.2.2 Longitudinal Separation Loss

We first consider longitudinal separation loss in the hollow core fiber. Calculations were carried out assuming the light to be evenly distributed along the fiber diameter, and according to a Gaussian distribution in emission angle, whose maximum value is equal to the local numerical aperture. As note above, the Gaussian distribution was controlled by the width parameter, called *ba* in our program. When *ba* is equal to zero, the power is evenly distributed, otherwise the power takes a Gaussian distribution in angle.

In the model, the existence of the hollow core fiber was initially neglected because the refractive index of the core is 1, the refractive index of the cladding is about 1.5 for the hollow core fiber, and the reflection coefficient is 4% if a ray hits the boundary between the core and cladding perpendicularly. In fact, the angles of the rays leaving the transmitting fiber to the hollow core boundary wall are much smaller than 90^{o}, so that the reflection coefficient much less than 4% for one polarization state, and

somewhat more for the orthogonal state. Thus, for each ray, roughly 96% of the power will be lost if the ray reaches the boundary, and of the reflected light, only a portion would eventually be collected by the receiving fiber. Therefore, this contribution to the total power collected was ignored.

In the absence of the hollow core boundary, the power captured by the receiving fiber can be readily calculated by our computer model. Ray transfer matrix rules were strictly employed to determine the position and angle of each ray at the plane of the receiving fiber face; if the ray position and angle fall within the the receiving fiber diameter and maximum numerical aperture at that point, then the ray is collected. Otherwise it will be lost (meaning that the power for this ray will be assigned a zero value). The total power received is obtained by summing the powers carried by each ray. The FORTRAN 77 program 1 which performs this calculation can be seen in the appendix. Figure 5.14 shows the theoretical loss curves with longitudinal separation produced by the model for three different energy distributions: ba = 0 represents an even energy distribution, while curves with ba = 10 and ba = 30 have increasing concentrations of energy near the central axis of the fiber. That is, there are more lower-order modes in the power distribution with ba = 30 than that in the power distribution with ba = 10. Curves A, B, and C were generated using the energy distributions shown in Figure 5.15, with A representing an even energy distribution, for comparison to previous work. Curves B and C have increasing concentrations of energy near the fiber axis. If curves A, B, and C are collectively compared to the curves produced by the even energy distribution model, we see that they have a fundamentally different shape.

The loss due to longitudinal separation was measured experimentally for a 100/140 micron step-index fiber, with an acceptance angle of 16.86^{o} (in air). The light in the fiber showed the typical "Gaussian" distribution in angle. The loss verses fiber end separation appears in Figure 5.16. Apparently, the model curve does not match the experimental data well, the possible reasons will be discussed in Chapter 6.

5.3 Radial Power Distribution Measurement

For optical fiber communication, the radial field distribution is one of the important parameters characterizing a optical fiber since it determines

launching efficiency, splice loss, transition loss, microbending loss, and wave-guide dispersion. The field diameter of the radial field distribution is two times the spot size. We measured the radial power distribution using the concept of the radial field distribution. Most research which has been done deals with single-mode fibers, one of the reasons is that the fundamental mode LP_{01} is transformed into a free beam which is very similar to the fundamental Gaussian beam. For multimode optical fibers, few successful models came out.

The approach of our computer model is as follows: first the radial power distribution output from a given fiber is measured experimentally at several values of distance from the fiber end. At the same time, the model generates predicted power distributions at each distance. The Gaussian width parameter discussed above, ba, is then adjusted until reasonable agreement between model and experiment is reached. The model then uses an output beam with this value of ba in subsequent calculations of axial displacement and bending losses. If in these tests the modeled and experimental results are similar, our theoretical approach of the model is likely to be correct; otherwise the model needs to be improved.

Because the measurement of the radial power distribution is foundational to the process above, in the next section we would like to introduce several methods used to accomplish this task.

5.3.1 Knife Edge Method

It is well known that the fundamental mode intensity nearly satisfies the Gaussian equation, which we already derived equation 4.7 in Chapter 4:

$$I(r,z) = \left(\frac{W_0}{W(z)}\right)^2 I_0 \exp\left(\frac{-2r^2}{W^2(z)}\right) \quad , \tag{5.3}$$

where

$$W(z) = \left(\frac{(b^2 + 4z^2)}{(b\,k)}\right)^{1/2} \quad , \tag{5.4}$$

$k = 2\pi/\lambda$, $b = kW_0^2$, $W_0 = W(0)$, and $z = 0$ is taken in the plane of the beam waist. Note that b and k are the usual confocal parameter and propagation constant, respectively.

The value of W can be obtained in several ways. The most straightforword is to scan the beam with a pinhole, but this method is slow and tedious. A faster and simpler method is to chop the beam periodically with a straight edge travelling at a known velocity u in the plane in which one wishes to know the value W. For a Gaussian beam, the detected power of the chopped beam is given by

$$p(t) = p_o \int_{-\infty}^{\infty} \int_{ut}^{\infty} \exp\left[-\frac{(ut')^2 + y^2}{W^2}\right] dt'\, dy \quad . \tag{5.5}$$

The variation of p with time is illustrated in Figure 5.17. Performing the indicated integration over y, differentiating Eq. (5.5) with respect to t, and solving for W gives

$$W = -(2/\pi)\, u \left\{ \frac{[p(t)]_{max}}{(dp/dt)_{max}} \right\} \quad . \tag{5.6}$$

Consider the circuit shown schematically in Figure 5.18. Let $v_0(t)$ be the (amplified) voltage from the photodetector and let $v_1(t)$ be the output of a simple RC differentiating circuit when $v_0(t)$ is its input. Then since $v_0(t)$ is proportional to p(t), Eq. (5.6) becomes

$$W = (2/\pi)^{1/2}\, u\, R\, C \left\{ \frac{[v_0(t)]_{max}}{[v_1(t)]_{max}} \right\} \tag{5.7}$$

where R and C are the resistance and capacitance of the differentiating circuit. The value of W can be quickly determined from the circuit in Figure 5.18. It was found to be most suitable to choose a convenient ratio for $[v_0(t)]_{max}/[v_1(t)]_{max}$ and to set the gain in the two oscilloscope channels such that the two maximum values have equal height when this ratio is achieved as illustrated in Figure 5.18. Then R and C are adjusted until the desired

ratio is achieved, and W is calculated from Eq. (5.7). More experiment details are contained in reference [37].

5.3.2 Aperture Method

This technique involves axially translating a precision-machined circular aperture in the far field of a fiber and measuring the power received by a photodetector as a function of axial position. The different positions correspond to different far field acceptance angles. This far field axial scanning technique (FFAST) provides a measure of the integrated far field power and can be used with the type of incoherent light source found in most monochromator-based spectral attenuation test sets in the manufacturing environment. This integrating feature also mitigates the error caused by endface defects [38].

A schematic of the FFAST measurement system used by C. Saravanos and R. S. Lowe is shown in Figure 5.19. A brass disc containing a 2.5 mm-diameter precision-machined circular aperture is placed between the test fiber and a 1 mm thermo-electrically cooled InGaAs p-i-n photodiode so the the center of the aperture coincides with the fiber-detector optical axis. The light passing through the aperture is collected and focused onto the detector by a pair of antireflection-coated achromat lenses. The aperture is moved to different positions along the optical axis by means of a translation stage driven by a computer-controlled precision stepper motor. At each position, corresponding to a particular acceptance cone angle, the transmitted power is measured. Care was taken during the construction of the apparatus to ensure that the aperture remained optimally aligned over the entire 6.4 cm travel of the stage.

There is another integral method similar to the FFAST method which also uses a variable circular aperture, the variable aperture far-field (VAFF) method [39]. The beam radiated from the end of the fiber is transmitted through a lens with variable aperture. The lens focuses the transmitted light onto a photodetector. The power transmitted through the aperture is measured as a function of the aperture diameter. Usually, the diameter of the aperture is not changed continuously but stepwise. At least twelve aperture spanning the half-angle range of numerical aperture from 0.02 to 0.25 should be used.

Instead of an array of aperture with different diameters, one can also use a single circular aperture. In our laboratory, we have a variable diameter circular aperture which could be fixed in front of the photodetector, thereby greatly simplifying measurements based on the FFAST method. One major advantage of this technique is that alignment between the fiber output beam and the translation stage is no longer a major concern, and in fact the translation stage driven by a computer-controlled precision stepper motor can be completely omitted. On the other hand, this method requires being able to accurately determine the opening of the variable aperture at each setting, a problem which can be cumbersome if great accuracy is required.

5.3.3 CCD Camera Method

In order to measure the two-dimentional intensity distribution in the far field, a CCD camera can be used. For multimode optical fibers, the CCD method is the probably the best measuring the radial power distribution. Our experimental set-up for this technique is illustrated in Figure 5.20. One end of a multimode fiber was connected to a LED source, used to minimize modal interference. The other end was held in a fiber micropositioner mounted on a conventional micropositioner with the fiber endface perpendicular to the surface of a CCD camera. The camera is connected directly to a Macintosh computer; thus images of the power distribution could be captured and processed.

Figure 5.21 shows the reverse negative of an actual image captured with a 100/140 μm core-cladding step-index fiber as close to the protective glass of the CCD array as possible (roughly 5 mm). The Gaussian-like, two-dimentional intensity distribution of Figure 5.22 is obtained by taking a digitized, polygonal slice of the image, represented as the dotted line in the Figure 5.21. The maximum intensity was recorded at intervals of separation distance between the front of the camera and the end of the fiber. The experimental behavior of the maximum intensity was then compared with the same for a Gaussian function, but no correlation is infered.

In practice, two major obstacles impaired the use of the CCD for radial power distribution measurements. These are, 1) The protective glass of the CCD array limits the amount of information that can be yielded, since its

thickness (which is not precisely known) prevents taking data at smaller separation distances where the intensity change with distance would be more distinct. Removal of the glass would be necessary to obtain a more valid comparison to the Gaussian propagation, but the CCD manufacturer considers this to present an extremely high risk to the life of the CCD. 2) The CCD array is easily saturated. The DC supply powering the LED has to be reduced to a very low voltage to avoid saturation, which is far away from the 5 Volts value that is specified. This in turn could lead to an unknown change in the modal power distribution launched in the fiber. Each of these barriers could be overcome given enough analysis and money, but the inconvenience presented suggested finding another method to determine the radial power distribution.

5.3.4 Pinhole Method

For measuring the far field radiation pattern, the fiber is allowed to radiate freely from its end. At a distance r from the center of the radiation fiber endface, the intensity is measured on a spherical surface as a function of the polar angle θ. Figure 5.23 shows the coordinates used in the measuring method.

With a direct photodetector with a pinhole attached, one measures not the amplitude distribution, but the intensity. A far-field radiation pattern $P_p(\theta)$ is defined as the angular distribution of the power detected by a photodetector with a pinhole aperture moved on a circle around the fiber end. The far field radiation pattern $P_p(\theta)$ is proportional to the square of the normalized amplitude distribution.

$$Pp(\theta) = c|E_H(q)|^2, \tag{5.8}$$

with c being unimportant constant and with the variables θ and q related through $q = (1/\lambda)\sin\theta$.

Instead of measuring the intensity on a circle (r = constant, θ variable), it can also be measured on a transverse straight line (z = constant, ρ variable) (see figure 5.23). The power $P'_p(\rho)$ received from a photodetector scanned along a straight line through an axis point with coordinate z,

which is related to the power $P_p(\theta)$ measured by a photodetector scanned along a circle through the same point by

$$P'_p(\rho) = P_p(\theta) \cos^2\theta \tag{5.9}$$

where the variable θ and ρ are related by

$$\rho = z \tan\theta \tag{5.10}$$

Relation (5.9) is obtained by taking into account that power received is the product of the intensity $|E_f(r,\theta)|^2$ and the projected sensitive area of the photodetector. A factor of $\cos^2\theta$ in Eq. (5.9) is caused by the fact that, for the linear scan, the distance r increases in inverse proportion to $\cos\theta$, and another factor of $\cos\theta$ by the fact that the projected area decreases as $\cos\theta$. A possible dependence of the reflection loss on the angle θ has been neglected in Eq. (5.9).

Since the far field of the fundamental mode is approximately circularly symmetric, i.e. independent of the azimuth ϕ (Figure 5.23), it is often sufficient to measure the intensity as a function of the polar angle q only. Figure 5.24 shows the experimental apparatus for measuring the function $P_p(\theta)$ or $P'_p(\rho)$ [18].

We have discussed radial field (or intensity) distribution measurement for single-mode fiber. For multimode optical fibers, the pinhole method still can be used as long as the far field distribution is circularly symmetric. The experimental measurements for optical multimode fibers which we have done were also conducted by using the pinhole method. One of the different size circular pinholes attached to the photodetector was used to measure the radial power distribution at different distances. The results are good enough if some requirements are met: 1) the pinhole aperture is much smaller than the far-field radiation pattern (the diameter of the pattern / the diameter of the pinhole $\geq$ 10), and 2) the pinhole aperture, scanned along a straight line through an axis point with z coordinate constant, can not overlap at each incremental scanning position.

Obviously, the results we obtained is one-dimentional intensity distribution which was already shown in Figure 5.11 – 5.13. Those curves are Gaussian-like, and match the power distribution calculated by the

model extremely well. That is most common method we have used in our experiments.

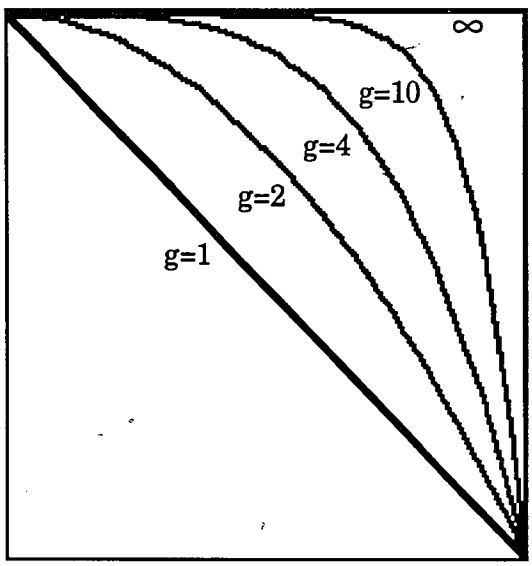

Figure 5.1 Index profiles of the form $n = n_{co} [1 - 2 \Delta (r/a)^g]^{1/2}$ for g = 1, 2, 4, 10 and ∞. For parabolic profile fibers $g \approx 2$.

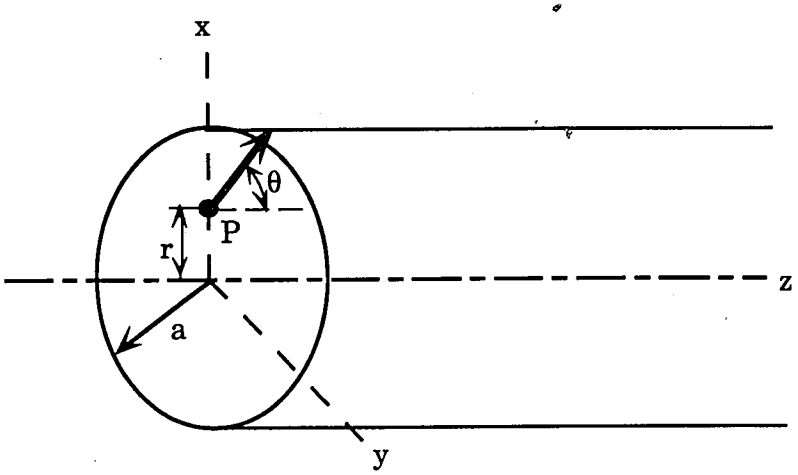

Figure 5.2 Coordinate system for a ray at point P(r,θ) on the face of an optical fiber core.

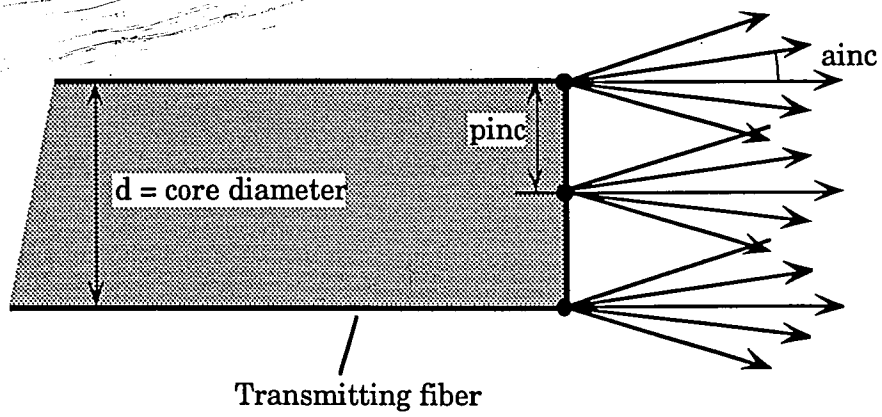

Figure 5.3 Weighting of energy in fiber modes by exit angles. Lower order modes will have smaller exit angles while higher order modes will be associated with larger exit angles.

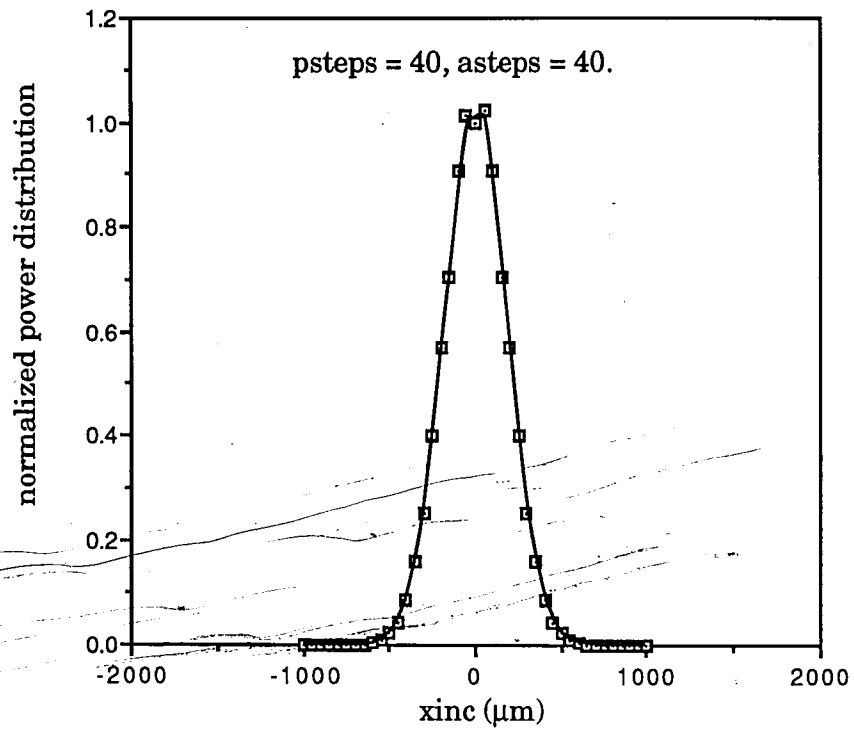

Figure 5.4 (a) Calculated far-field power distribution versus y axis which is perpendicular to the propergation direction with psteps = 40, asteps = 40 at 5mm from the fiber end when ba = 20, bp = 0.

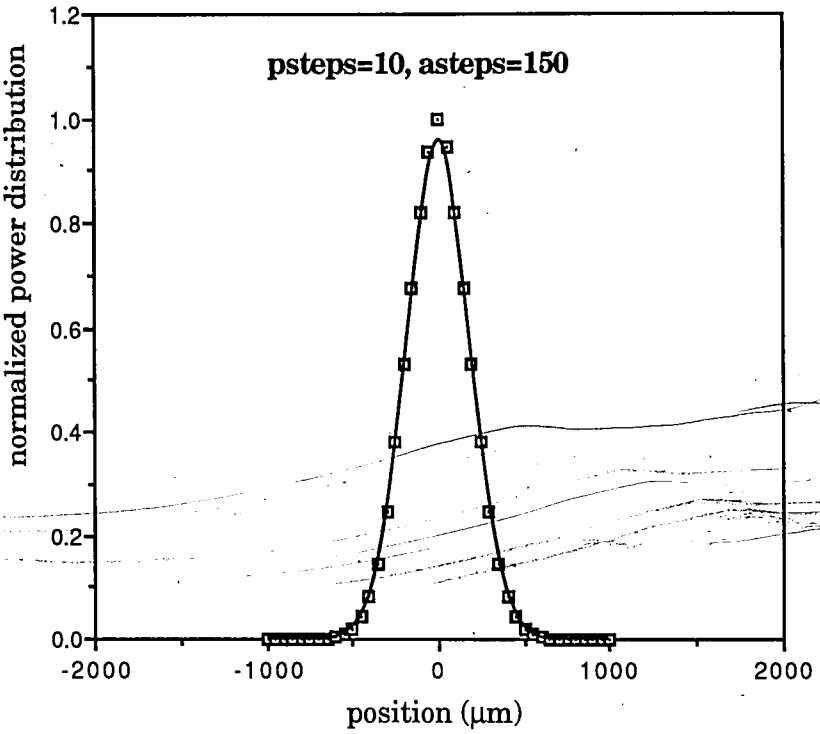

Figure 5.4 (b) Calculated far-field power distribution versus y axis with psteps = 10, asteps = 150 at 5mm from the fiber end when ba = 20, bp = 0.

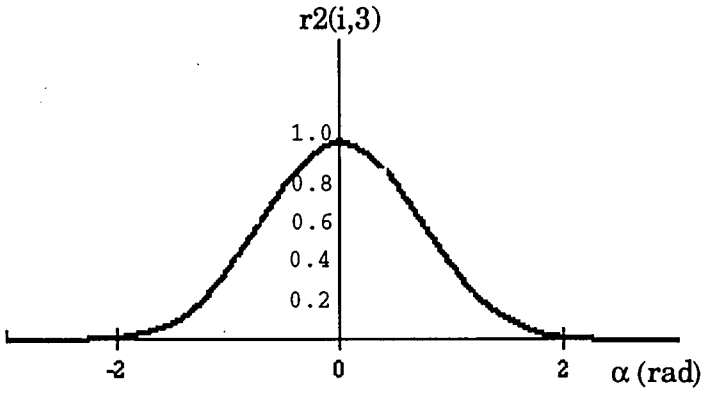

Figure 5.5 The power is Gaussian-like distributed in angle.

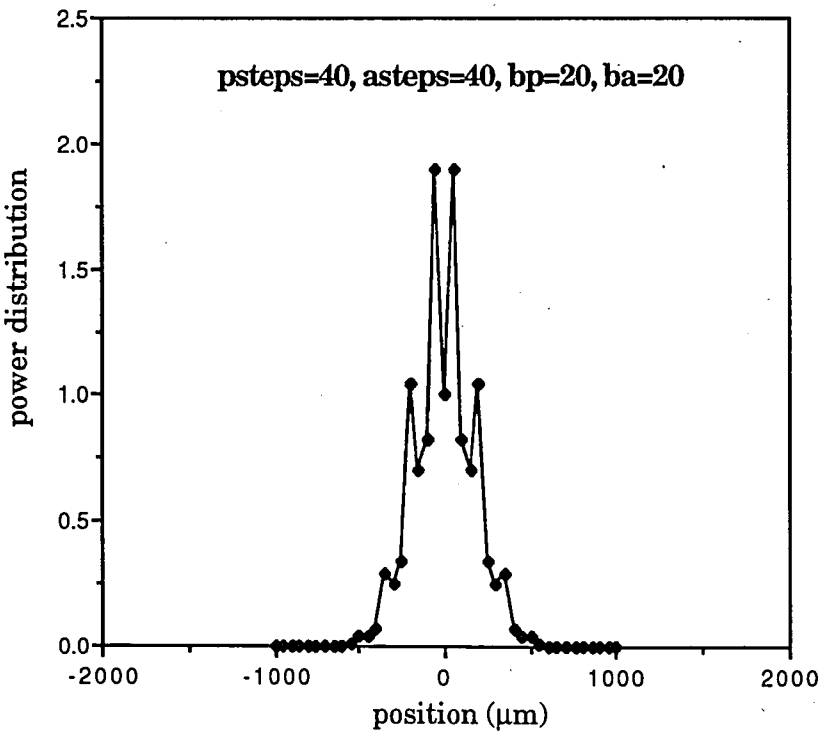

Figure 5.6 Calculated far-field power distribution versus radial increments with psteps = 40, asteps = 40 at 5mm away from the fiber end when ba = 20, bp = 20.

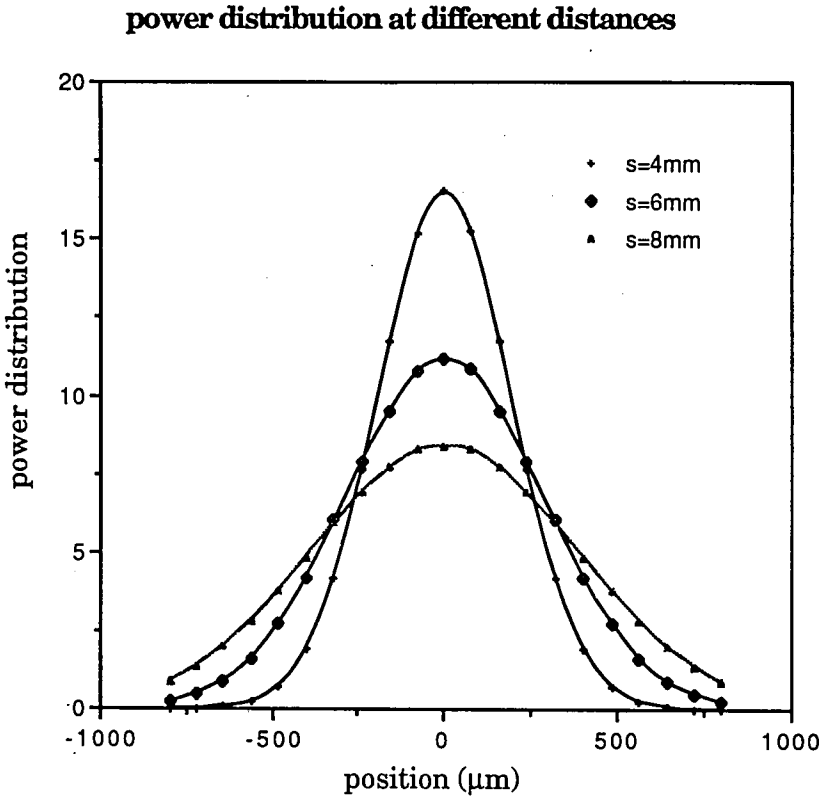

Figure 5.7 The power distributions from the model spread out along the propagation direction when the distances away from the fiber end are 4, 6, and 8mm.

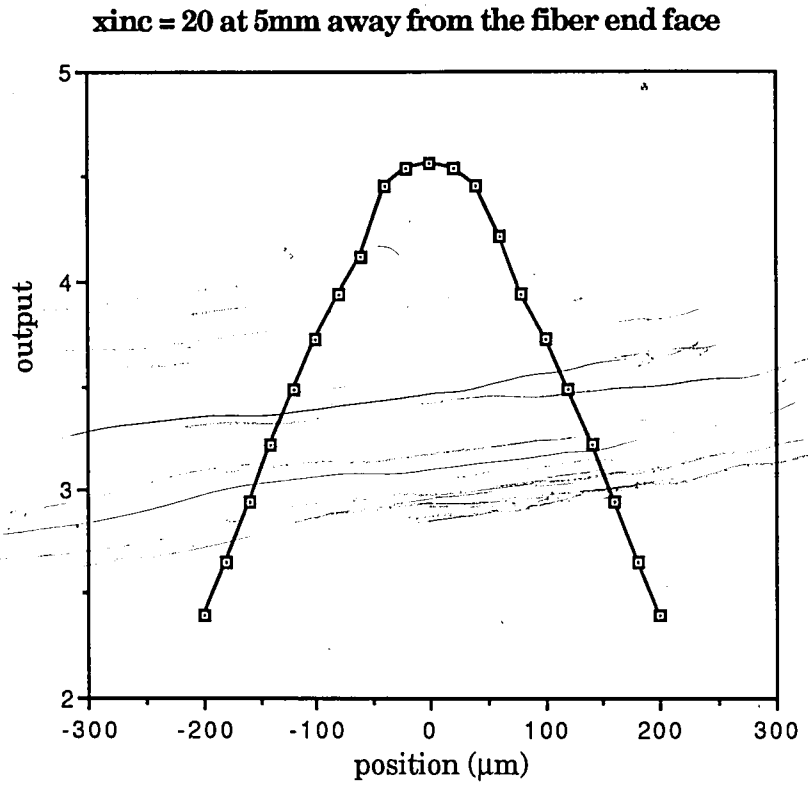

Figure 5.8 The power distribution with inproperly increments when xinc = 20.

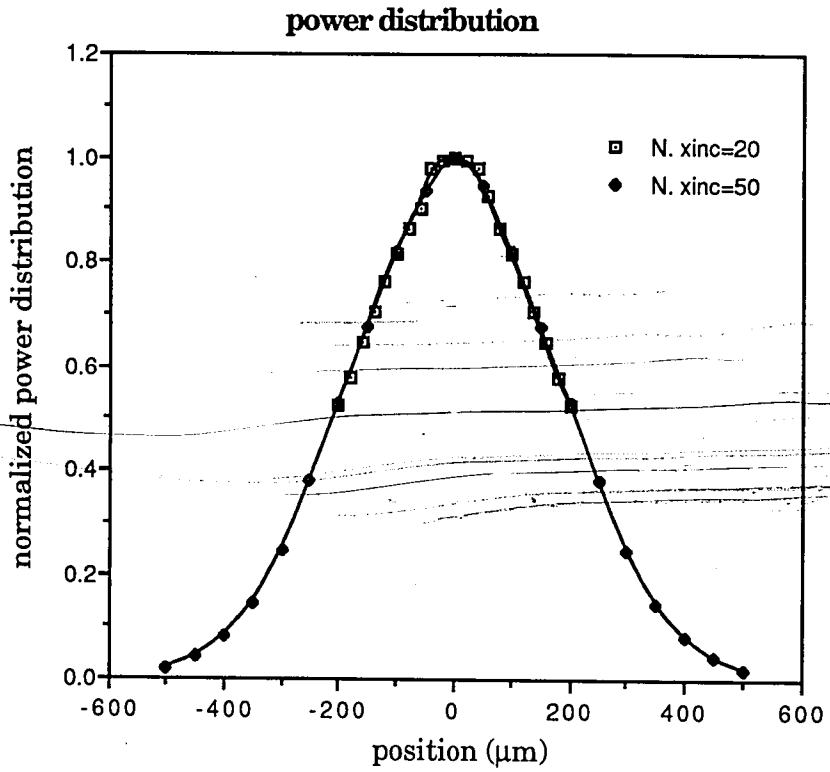

Figure 5.9 Different resolution doesn't affect the power distribution shapes.

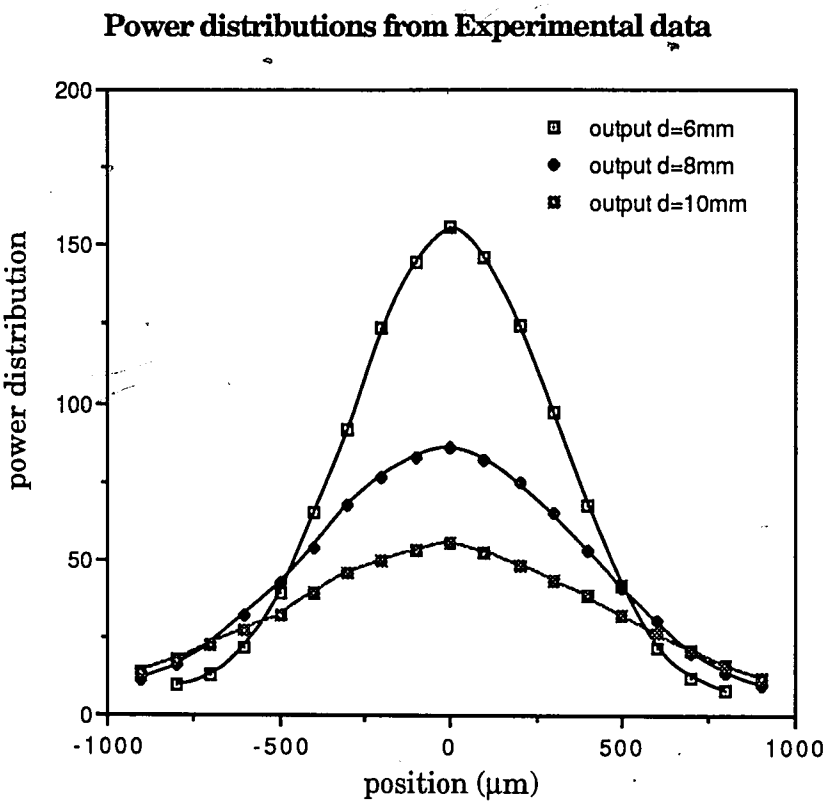

Figure 5.10 The power distributions from the experiment spread out along the propagation direction when d = 6, 8, and 10mm.

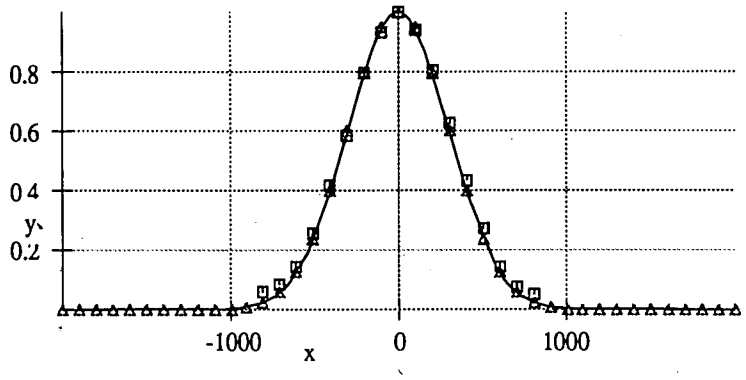

Figure 5.11 Power distribution data from both the model and the experiment when d = 6mm. Experimental data are represented by squares, the model data are represented by triangles, the solid line is a Gaussian curve.

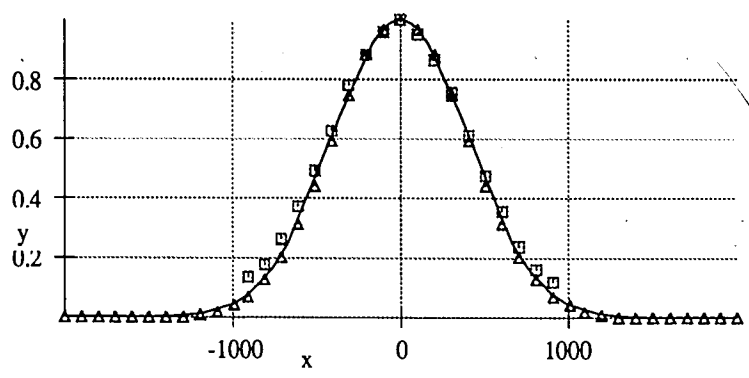

Figure 5.12 Power distribution data from both the model and the experiment when d = 8mm. Experimental data are represented by squares, the model data are represented by triangles, the solid line is a Gaussian curve.

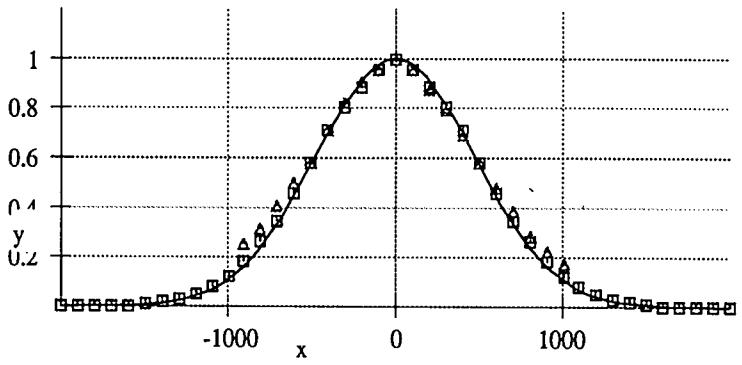

Figure 5.13 Power distribution data from both the model and the experiment when d = 8mm. Experimental data are represented by squares, the model data are represented by triangles, the solid line is a Gaussian curve.

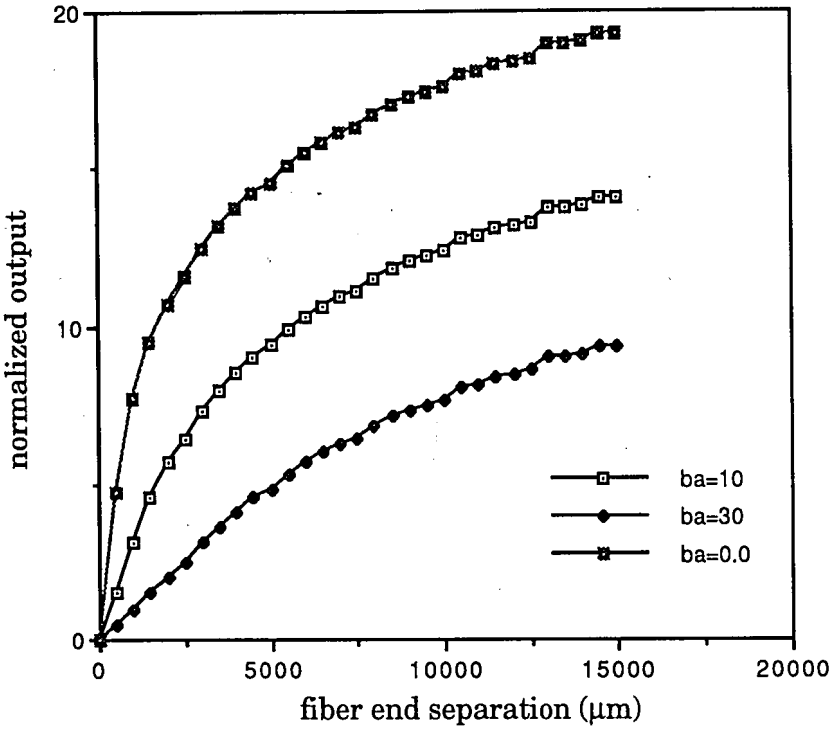

Figure 5.14 The power captured by the receiving fiber versus fiber end separation.

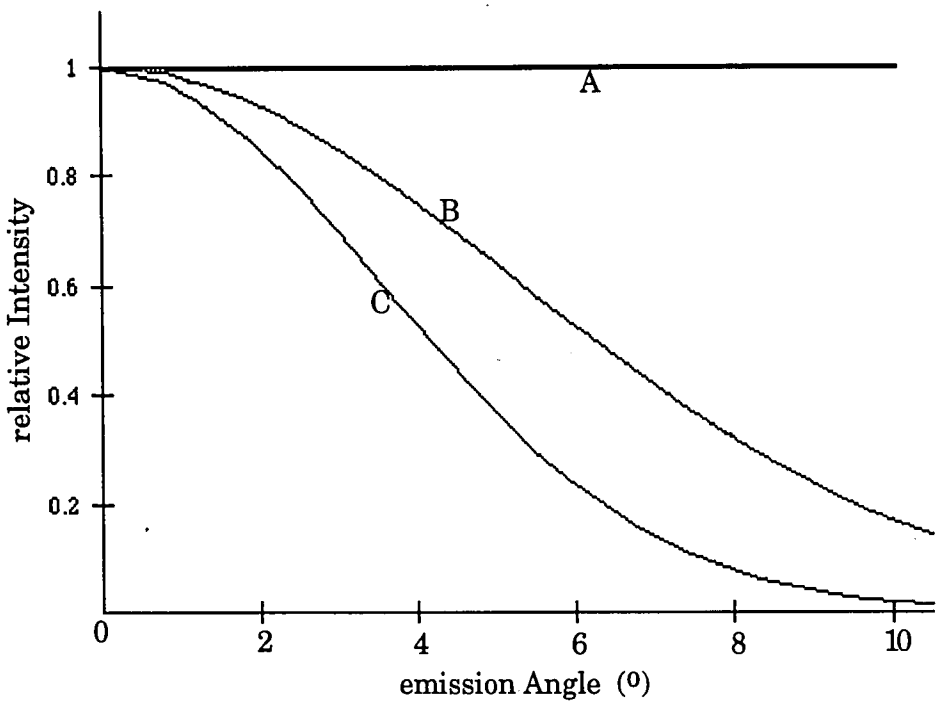

Figure 5.15 Energy versus emission angle.

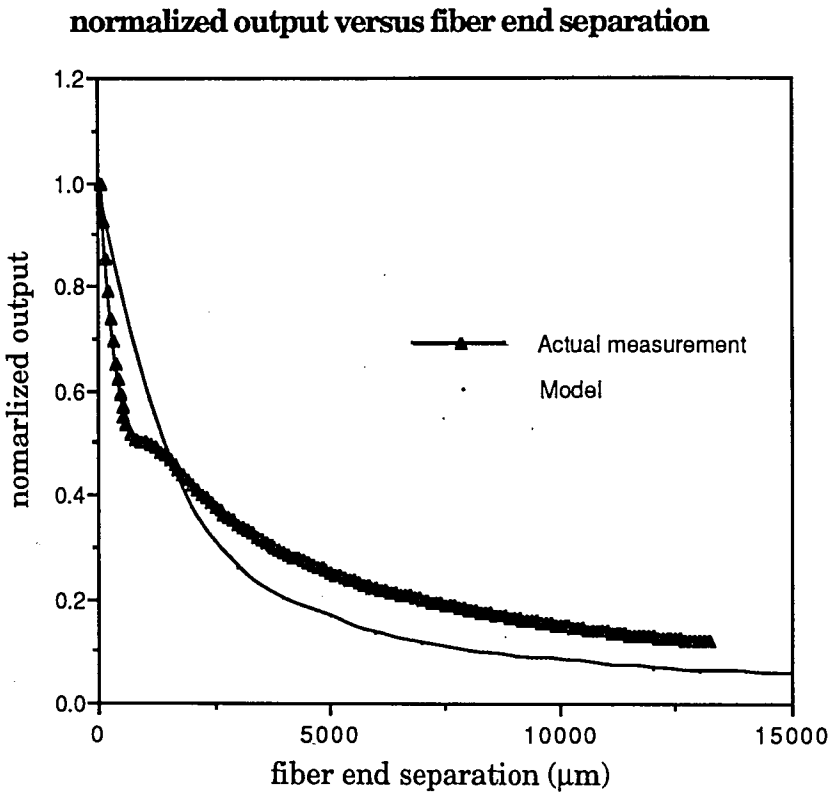

Figure 5.16 Normalized output versus fiber end separation. The solid line is generated using the present model with the energy distribution (ba=14.5), while discrete points represent actual measurements. It was discovered through multiple trials that the experimental data were quite repeatable.

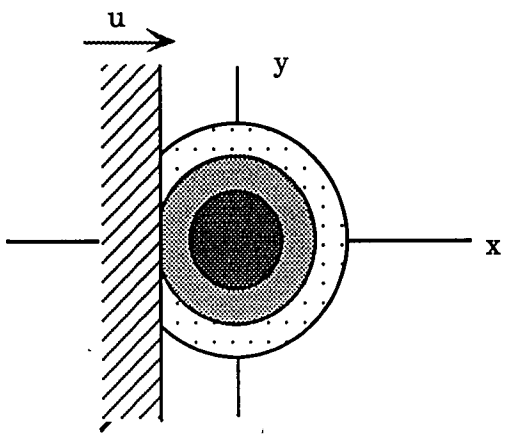

(a)

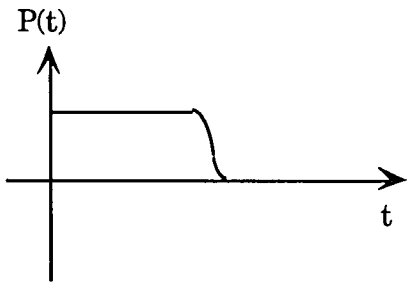

(b)

Figure 5.17 (a) Relative orientation of chopper blade and Gaussian beam. (b) Optical power of chopper beam as a function of time [37].

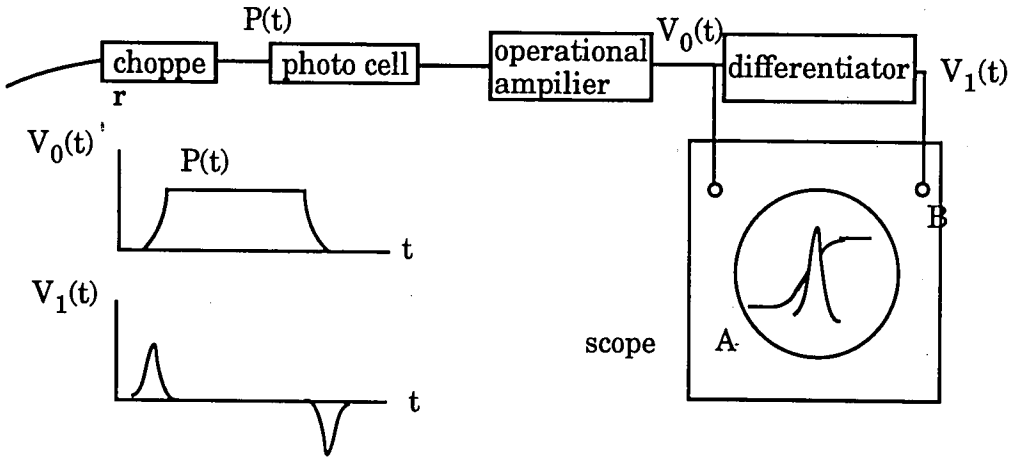

Figure 5.18. Block diagram of the beam width measuring circuit [37].

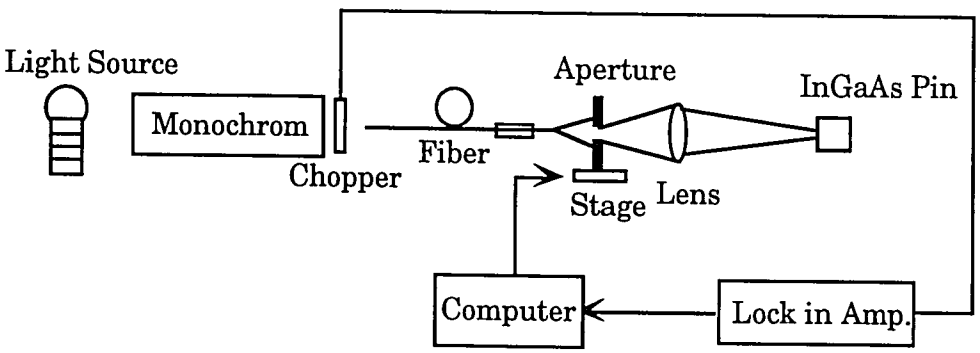

Figure 5.19 Schematic diagram of the FFAST measuring system [38].

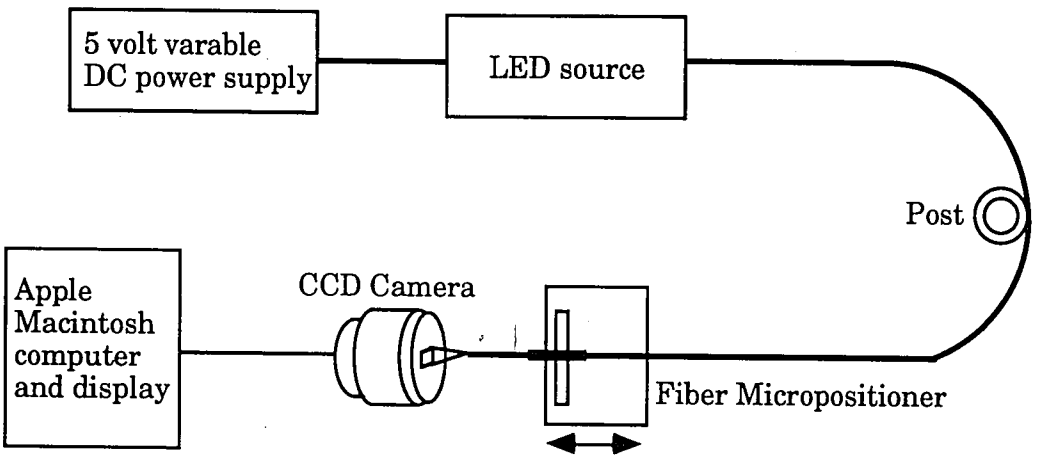

Figure 5.20 CCD camera experiment set up.

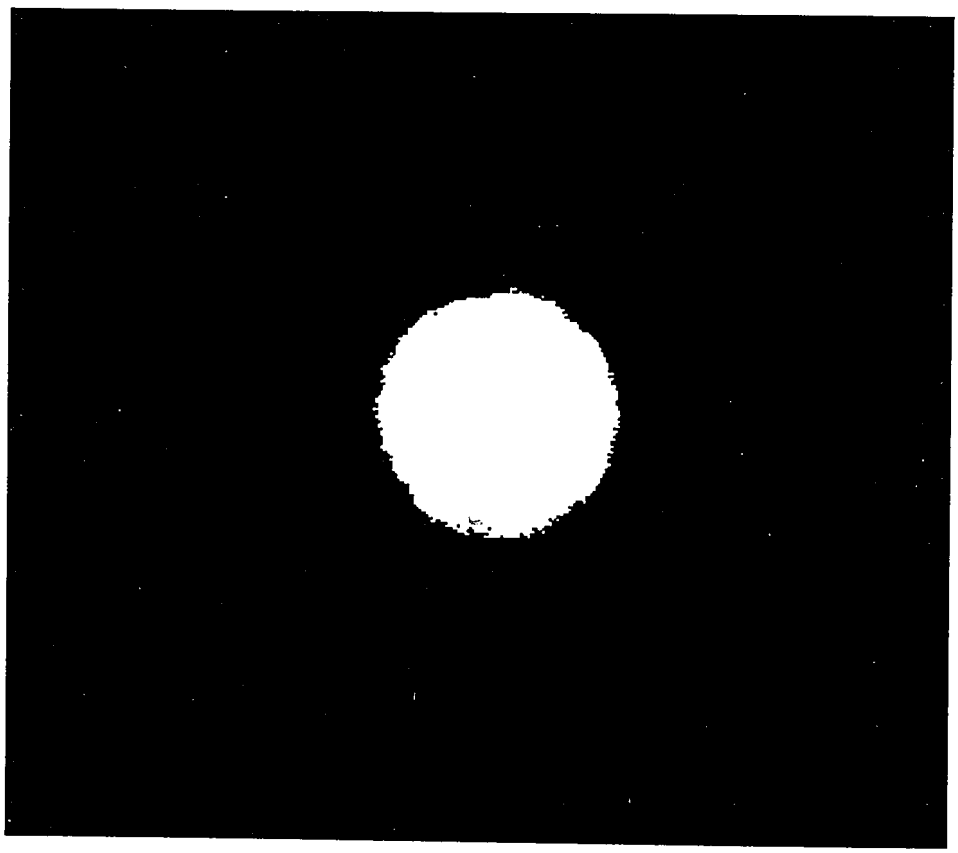

Figure 5.21 CCD image of a multimode fiber output when the fiber is excited with LED light.

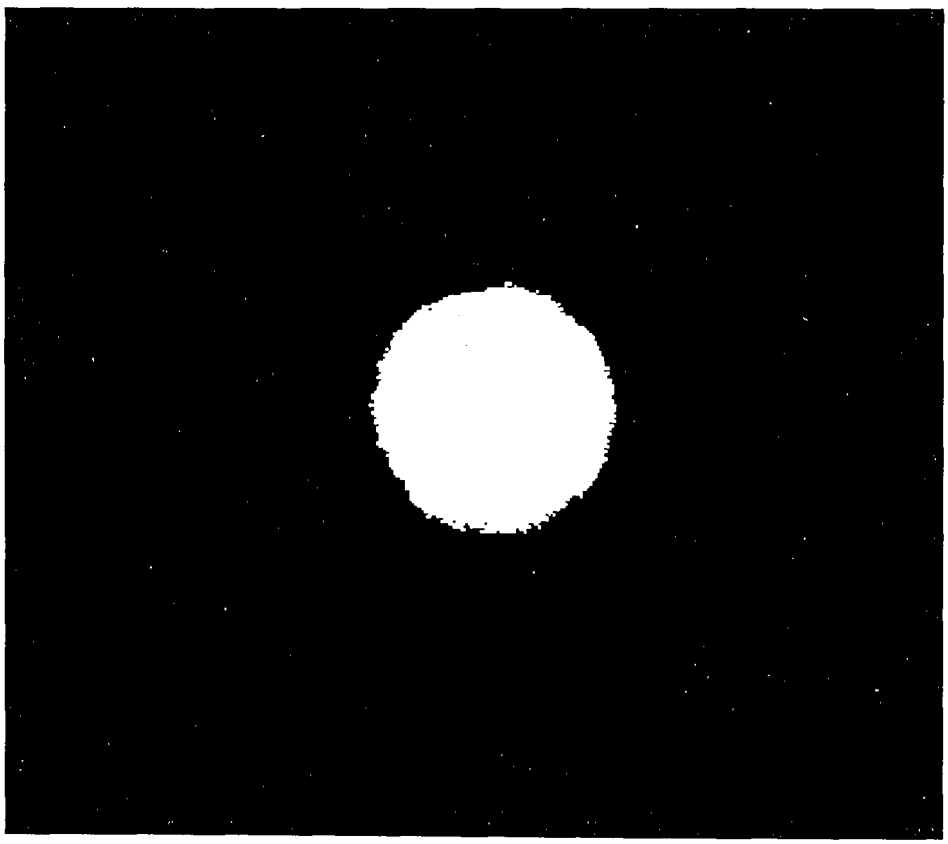

Figure 5.21 CCD image of a multimode fiber output when the fiber is excited with LED light.

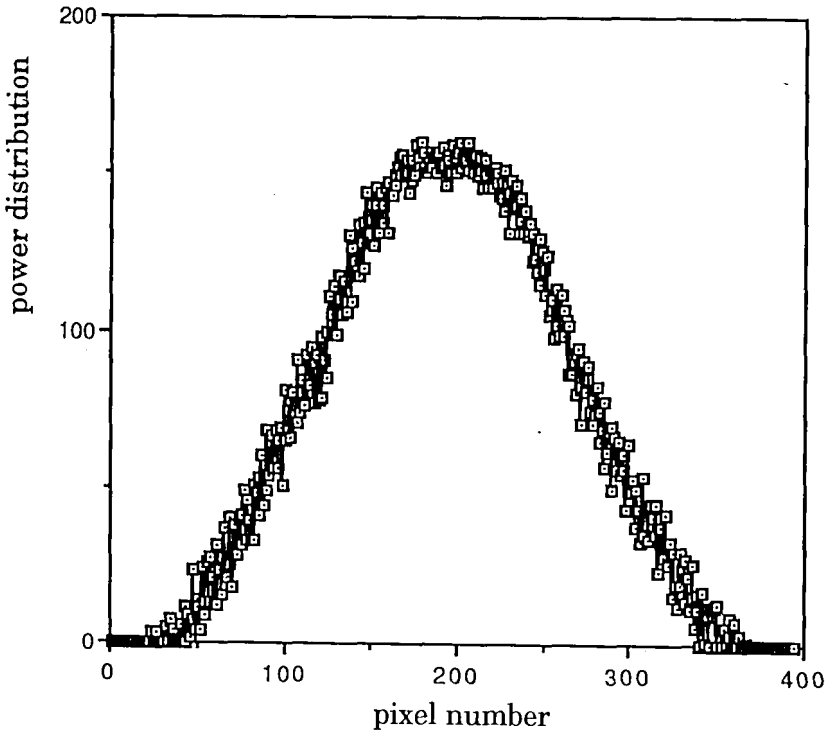

Figure 5.22 2 – D slice of CCD image.

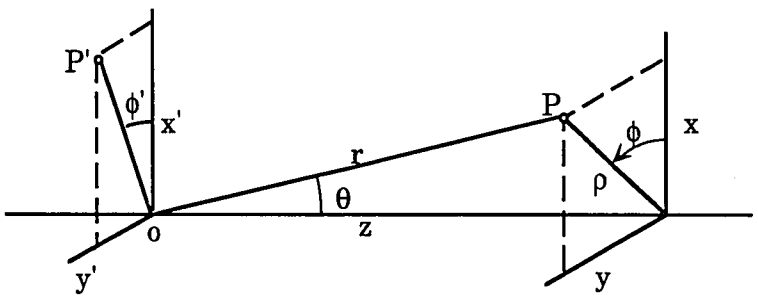

Figure 5.23 Cylindrical polar coordinates ρ', ϕ', o of the source point in the fiber end face and cylindrical polar coodinates ρ, ϕ, z and spherical coordinates r, θ, ϕ of the observation point in the field radiated from the fiber end.

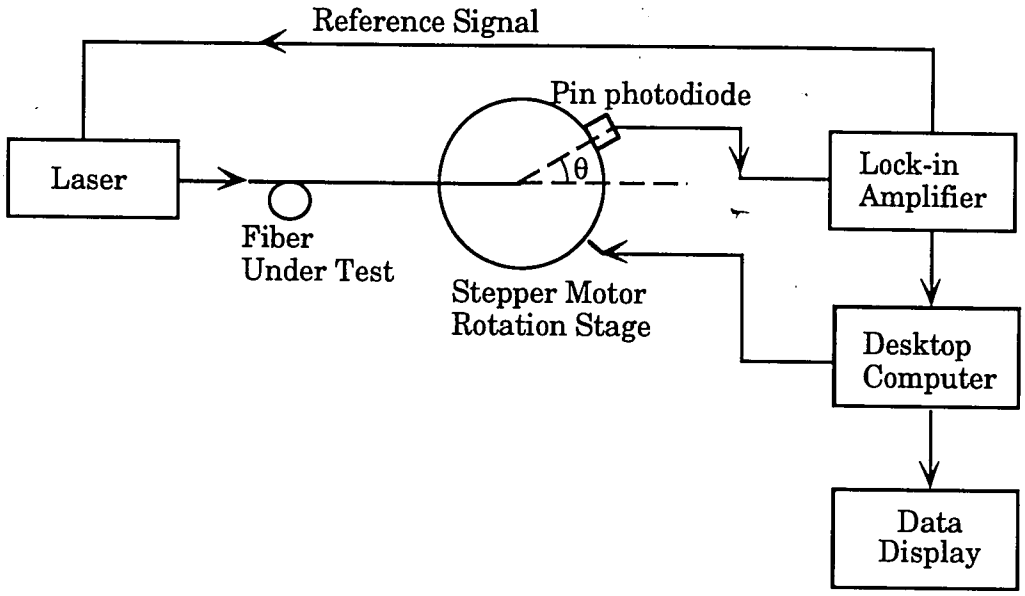

Figure 5.24 Experimental apparatus for measuring the far field radiation pattern.

6. Computer Simulation of the Sensor

The general approach for determining the power distribution at the end face of the fiber was discussed in chapter 5. Next we would like to introduce the load monitor, which is based on the deflection of the hollow core fiber. The experimental set up for bending the fiber is illustrated in Figure 6.1. Two fiber ends are inserted into a hollow core fiber--essentially a flexible glass tube--with a predetermined gap left between them; the hollow core sleeve is affixed to a strip of spring steel, which is then placed in a three point bending fixture. A force is applied to the center of the spring steel using a vertically oriented micropositioner, and the hollow core fiber is bent. In this chapter, discuss how the power captured by the receiving fiber can be modelled. In the computer program, the power leaving the transmitting fiber is normalized to 100.

6.1 Principle of the Sensor Model

A cross section of the bending hollow core fiber with two solid-core fibers inserted is shown in Figure 6.2, where the axis of the bent fiber takes the form of a circular quadrant of radius R. It will be assumed in the following analysis that the excitation of the fiber along the straight section is such that only bound rays are exited in the core. These rays are travelling at angles to the axis such that there is no refraction into the straight part of the cladding. The discrete positions and angles relative to the optical axis (core axis) which are followed by these rays in the straight section are designated by *r2(i,1)* and *r2(i,2)* respectively, and *r2(i,3)* is the power of each ray. The rays will be traced using the ray transfer matrix that was introduced in Chapter 2. The parameters *r2(i,j)* can be treated as input components in the ray transfer matrix. In a similar fashion, the values of positions and angles at the end face of the receiving fiber will be designated by *r3(i,1)*, *r3(i,2)*, and power is *r3(i,3)*. The values *r3(i,j)* can be treated as output components in the ray transfer matrix.

The permutation for the angles of the rays travelling from the transmitting fiber to the receiving fiber are as follows. In the first case, *r2(i,2)* and *r3(i,2)* are negative. This can be seen in Figure 6.3. The

segment OA is given by R + *r2(i,1)*, the angle CAO is equal to $\pi/2 - r2(i,2)$, h is the deflection distance, while the angle AOC can be calculated by

$$\text{angle AOC} = \frac{d}{R} \quad , \tag{6.1}$$

In triangle AOC, r3(i,2) and OC can be computed by

$$r3(i,2) = \text{angle AOC} - r2(i,2) \quad , \tag{6.2}$$

so

$$\frac{OC}{\sin\left(\frac{\pi}{2} - r2(i,2)\right)} = \frac{OA}{\sin\left(\frac{\pi}{2} - r3(i,2)\right)} \quad , \tag{6.3}$$

then

$$OC = OA \frac{\sin\left(\frac{\pi}{2} - r2(i,2)\right)}{\sin\left(\frac{\pi}{2} - r3(i,2)\right)} \quad , \tag{6.4}$$

$$= OA \frac{\cos\left(r2(i,2)\right)}{\cos\left(r3(i,2)\right)} \quad . \tag{6.5}$$

The position of the ray at the end face of the receiving fiber will be

$$r3(i,1) = OC - R \quad , \tag{6.6}$$

and thus the output components *r3(i,1)* and *r3(i,2)* were obtained. If the position *r3(i,1)* is within the diameter of the receiving fiber and *r3(i,2)* is within the acceptance angle of the fiber, then the ray will be captured by the receiving fiber.

In the second case, shown in Figure 6.4, *r2(i,2)* is positive, and *r3(i,2)* is negative. OA is again given by R + *r2(i,1)*, the angle CAO is equal to $\pi/2$ + *r2(i,2)*, and angle AOC is given by the same calculation as above, viz.,

$$\text{angle AOC} = \frac{d}{R} \quad . \tag{6.7}$$

In triangle AOC, *r3(i,2)* and OC can be computed by

$$r3(i,2) = \text{angle AOC} + r2(i,2) \quad , \tag{6.8}$$

so

$$\frac{OC}{\sin\left(\frac{\pi}{2} + r2(i,2)\right)} = \frac{OA}{\sin\left(\frac{\pi}{2} - r3(i,2)\right)} \quad . \tag{6.9}$$

then

$$OC = OA \frac{\sin\left(\frac{\pi}{2} + r2(i,2)\right)}{\sin\left(\frac{\pi}{2} - r3(i,2)\right)} \quad , \tag{6.10}$$

$$= OA \frac{\cos\left(r2(i,2)\right)}{\cos\left(r3(i,2)\right)} \quad . \tag{6.11}$$

The position of the ray at the end face of the receiving fiber again is

$$r3(i,1) = OC - R \quad . \tag{6.12}$$

In the third case, depicted in Figure 6.5, *r2(i,2)* is negative, and *r3(i,2)* is positive. OA is again given by R + *r2(i,1)*, the angle CAO is equal to $\pi/2$ – *r2(i,2)*, and angle AOC is as before.

In triangle AOC, r3(i,2) and OC can be computed by

$$r3(i,2) = r2(i,2) - \text{angle AOC} \quad , \tag{6.13}$$

so

$$\frac{OC}{\sin\left(\frac{\pi}{2} - r2(i,2)\right)} = \frac{OA}{\sin\left(\frac{\pi}{2} + r3(i,2)\right)} \quad . \tag{6.14}$$

then

$$OC = OA \frac{\sin\left(\frac{\pi}{2} - r2(i,2)\right)}{\sin\left(\frac{\pi}{2} + r3(i,2)\right)} \quad , \tag{6.15}$$

$$= OA \frac{\cos(r2(i,2))}{\cos(r3(i,2))} \quad . \tag{6.16}$$

Once again, the position of the ray at the end face of the receiving fiber is

$$r3(i,1) = OC - R \quad . \tag{6.17}$$

The fourth case of the permutation is that both *r2(i,2)* and *r3(i,2)* are positive, however, we will disregard this case due to the impossibility of the situation. In the three possible cases, the same results were obtained.

Therefore if *r3(i,1)* is within the diameter of the receiving fiber and *r3(i,2)* is within the acceptance angle of the fiber, then the ray will be captured by the receiving fiber. This process is repeated with all rays. Program 2 represents the model of the bending hollow core fiber, which can be seen in the appendix.

6.2 Comparison of the Results of the Model and the Experiments

Figure 6.6 shows the output loss versus the deflection distance, as calculated by the model for different power distributions (i.e., different values of *ba*) and determined empirically. Curves A ~ C correspond to increasing concentrations of energy near the central axis of the fiber and at small exit angles. Curve D was measured experimentally for a step-index fiber of core/cladding diameter 100/140 microns, and acceptance angle 16.85^{o} (in air). Apparently none of the model curves could match the experimental curve. Potential reasons for this will be discussed at the end of the chapter.

6.3 Sensitivity

To make the best sensor, one must consider methods for increasing or decreasing sensitivity, depending on the intended sensor application. However, due to the simplicity of our device, only a limited number of parameters could be changed.

6.3.1 Change in Fiber End Separation

Consider first the sensitivity change due to a change in the fiber end separation. Figure 6.7 shows the losses in curved hollow core sections for different degrees of fiber end separation. The distance d in the figure indicates the vertical deflection of a straight section of the hollow core fiber. As expected from the sensor geometry, the curves of Figure 6.7 demonstrate that the larger the gap between fiber ends, the more sensitive the device is to bending.

6.3.2 Change in NA of the Fibers

We investigated effect on sensitivity of a change in either transmitting fiber or receiving fiber or both. As reviewed earlier, the numerical aperture is an important feature of the fiber, and is determined by the difference in refractive indices of the core and the cladding. It is a measure of the light acceptance capability of the optical fiber. As the NA increases, so does the ability of the fiber to couple light into the fiber. In the model, changes in NA led to changes in the amount of power captured by the receiving fiber, but the proportion of the power to the deflection distance did not change. So the sensitivity is not significantly affected by the numerical aperture of the fiber.

6.3.3 Change in Diameter of the Fibers

Originally, we planned to use a smaller diameter receiving fiber to increase the sensitivity. However, even though different diameter fibers collect different amounts of power, the proportion of this power to the deflection distance does not change. We were therefore unable to use this method to alter sensitivity. Considering that a change in the numerical aperture does not affect sensitivity, it should be no surprise that a change in diameter does not have an effect either.

6.3.4 Change in Launching Condition

In our model, ba controls the width of the Gaussian power distribution. If ba is changed to a larger value, the width of the Gaussian power distribution is narrower, and the sensitivity increases. Therefore, for an

enhanced sensitivity, we should allow more lower order modes than higher order modes to propagate in the transmitting fiber. Among other ways, this can be realized by changing launching conditions.

6.3.5 Change in Index Profile of the Fibers

It is hard to model how the index profile will affect the sensitivity. From our experiments, we already know that graded-index fiber has better sensitivity than step-index fiber does. One might therefore speculate that a sharper index profile such as a triangular profile may lead to even higher sensitivity, though this is unconfirmed.

6.4 Another Model for Ray Propagation in the Hollow Core

In the original model, we did not consider the hollow core fiber in our calculations, in the sense that reflections from the inner walls of the hollow core were neglected. However, when the experimental and model results did not match, we began to realize that the existence of the hollow core fiber could not be ignored. Thus a new approach was taken, which accounts for the reflection of every ray from the inner walls of the hollow core fiber. For simplicity, we only assume that the rays are coming out from the center point of the transmitting fiber. It is reasonable to make such an assumption when the end separation is large enough (for our case, the separation is around 10 mm).

Figure 6.8 shows that the rays emerging from the center A of the transmitting fiber can be divided into three parts. Part one is from θ_{max} to θ_1, part two is from θ_1 to $-\theta_2$, part three is from $-\theta_2$ to $-\theta_{max}$. angle θ_{max} is the maximum angle a ray may take when emitted from the transmitting fiber, the angle θ_1 is between the center optical axis and the ray emitted from the transmitting fiber which first hits the outer core-cladding boundary and then reflects to make a tangent to the inner core-cladding boundary. The angle θ_2 is between the center optical axis and the ray which directly makes a tangent to the inner core-cladding boundary. Part one and part three are zigzag rays which have reflections on both inner and outer walls of the hollow core fiber, while part two comprises whispering gallery rays which have reflections only on the outer core-cladding

boundary. It is possible to prove that θ_1 is equal to θ_2. Thus $\theta_2 = \theta_1 = \cos($ $(R - a)/R)$.

In Figure 6.9, A is the source of the transmitted rays, the total power of which is normalized to 100, R is the radius OA from the center of curvature O to the entry point A on the plane OA, and a is the radius of the transmitting fiber. The positions of the emerging rays are fixed to *r2(i,1)* = R (center of the emitting fiber), the ray angles are designated by *r2(i,2)* and are evenly divided into *asteps* discrete angles, and *r2(i,3)* represents the corresponding ray power which is Gaussian with angle as before.

Case 1. We first analyze the case for $r2(i,2) < -\theta_2$. Those rays are zigzag rays. The incident ray AB makes an angle of incidence θ_I with the tangent to the inner core-cladding boundary at B, the incident ray AC makes an angle of incidence θ_0 with the tangent to the outer core-cladding boundary at C, and θ_i represents incident angle, i.e., $\theta_i = r2(i,2)$. For our computer program, i represents the ray number, and the angle O represents the angle between the plane OA and the radius to the end of the hollow core fiber.

In Figure 6.9, in triangle AOB

$$\frac{R}{\cos\theta_I} = \frac{R-a}{\cos\theta_i} \quad . \tag{6.18}$$

In triangle BOD

$$\frac{R-a}{\cos\theta_0} = \frac{R+a}{\cos\theta_I} = \frac{R+a}{R\cos\theta_i}(R-a) \quad , \tag{6.19}$$

and then we have

$$\cos\theta_0 = \frac{R}{R+a}\cos\theta_i \quad , \quad \theta_0 = \cos^{-1}\left(\frac{R}{R+a}\cos\theta_i\right) \quad ; \tag{6.20}$$

$$\cos\theta_I = \frac{R}{R-a}\cos\theta_i \quad , \quad \theta_I = \cos^{-1}\left(\frac{R}{R-a}\cos\theta_i\right) \quad . \tag{6.21}$$

For the zigzag rays which travel from A to B, the angle $\Delta\phi_{init}$ between the entrance plane OA and the radius to the first reflection point at B is readily shown to be given by

$$\Delta\phi_{init} = -(\theta_I + \theta_i) \quad . \tag{6.22}$$

After this reflection, all subsequent reflections possess an angular periodicity of the ray path given by the angle BOD, so that this periodicity from outer to inner core-cladding boundaries is

$$\Delta\phi = \theta_0 - \theta_I \quad . \tag{6.23}$$

The power collected by the receiving fiber will be

$$r3(i,3) = T\, r2(i,3) \quad , \tag{6.24}$$

where

$$T = T_I^{\,INT(mi/2+1)} + T_0^{\,INT[(mi+1)/2]} \quad . \tag{6.25}$$

Here, m_i is the total of the reflection numbers of the rays in the hollow core fiber, which is

$$m_i = | \, INT((\text{angle O} - \Delta\phi_{init}) / \Delta\phi)) \, | \quad . \tag{6.26}$$

T_I represents the reflection coefficient at outer core-cladding interface, T_0 represents the reflection coefficient at inner core-cladding interface, and INT designates the value in parentheses truncated to an integer value.

Case 2. Our second case is for $r2(i,2) > \theta_1$. Those rays are also zigzag rays, and the following relations apply.

$$\theta_0 = \cos^{-1}\left(\frac{R}{R+a}\cos\theta_i\right) \quad , \tag{6.27}$$

$$\theta_I = \cos^{-1}\left(\frac{R}{R-a}\cos\theta_i\right) \quad , \tag{6.28}$$

$$\Delta\phi_{init} = \theta_0 - \theta_i \quad , \tag{6.29}$$

$$\Delta\phi = \theta_0 - \theta_I \quad , \tag{6.30}$$

$$m_i = | \, (\, \mathrm{INT} \, ((\, \mathrm{angle} \, O - \Delta\phi_{init} \,) / \Delta\phi \,)) \, | \quad . \tag{6.31}$$

Case 3. Our third case is for $\theta_2 > r2(i,2) > \theta_1$, or the whispering ray case. It will be found from consideration of triangle EOF in Figure 6.8, that

$$\theta_0 = \cos^{-1}\left(\frac{R}{R+a}\cos\theta_i\right) \quad , \tag{6.32}$$

$$\Delta\phi_{init} = \theta_0 - \theta_i \quad , \tag{6.33}$$

$$\Delta\phi = 2\,\theta_0 \quad , \tag{6.34}$$

$$m_i = | \, (\, \mathrm{INT} \, ((\, \mathrm{angle} \, 0 - \Delta\phi_{init} \,) / \Delta\phi \,)) \, | \quad . \tag{6.35}$$

For more details, see Program 3 in Appendix.

This approach gives bending results which can be seen in Figure 6.10. Curves A, B, and C represent increasing energy concentrations. It is obvious that the experimental data is between the curve B (ba = 40) and curve C (ba = 60). Through power distribution measurements, the best match between experimental data and model results for 100/140 step index fibers is when ba =14.5, representing a large discrepancy.

6.5 Discussion

The loss in multimode, step-index fiber butt joints within a hollow core optical fiber due to axial displacement and vertical deflection are modeled. Previous models have traditionally assumed simplified calculations and

uniform energy distributions. This work differs from previous models in two fundamental ways: it allows for an arbitrary distribution of light energy among the fiber modes, and it considers very large misalignments. The energy distribution across the emitting fiber face was simplified by assuming meridional rays to be the only rays emerging from the transmitting fiber. Work by previous authors has verified that for many fiber modelling situations, this assumption does not lead to significant error [6]. Also, it should be noted that leaky rays leaving the electric field within the cladding and outside of the cladding have been neglected in our computations. These could be included by letting the point sources reach radius greater than the fiber core.

The model shows excellent agreement with the experimental data in free space, as shown clearly the power distribution measurements discussed in Chapter 5, and the work was done by a former student in the Photonics Lab [45]. For the simulation of axial displacement and deflection, the model depicts poor agreement with the measured data. One of the possible reasons could be that the meridional rays assumption was good enough to model a light transmission in the free space, but not in a hollow core fiber. The ray propagation in a hollow core fiber may be subject to some unknown mechanism related to reflections at the (air) core-cladding boundary. In our second model, we used the Fresnel equations to calculate the reflection coefficient of each ray on the inner wall of the hollow core fiber, with the result that the general trend is very similar to the actual measurement. On the other hand, in order to achieve this partial agreement, the ba that controls the width of the power distribution has to be around 50, which is far away from what we obtained by the measuring power distribution in free space (ba = 14.5). In the model we evenly split the polarization of the electric fields and magnetic fields, which may cause error.

Future work may be focused on using cones instead of rays to represent the mechanism in the hollow core fiber, and effect of electric and magnetic fields in the cladding may be considered. Some experiments will be conducted for a longitudinal displacement and angular misalignment without the hollow core fiber to confirm that the model is correct to simulate the mechanism in free space. In many experiments here, it was discovered that graded index fiber generally offered smoother end

separation curves and bending displacement curves, as well as higher sensitivity. This suggests extending our modeling work to the graded index case, by varying the NA along the radius.

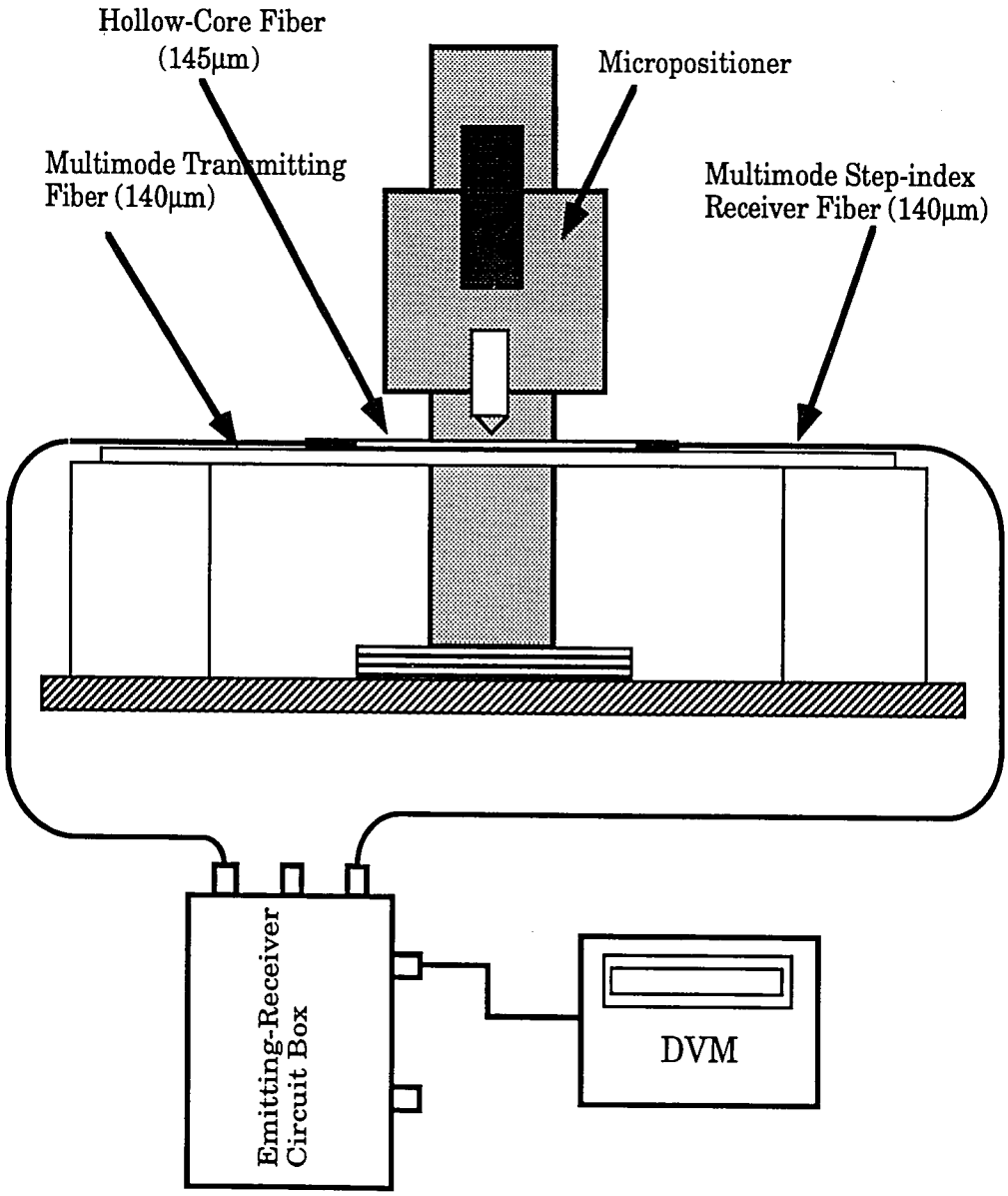

Figure 6.1 Hollow-core fiber bending experiment set up.

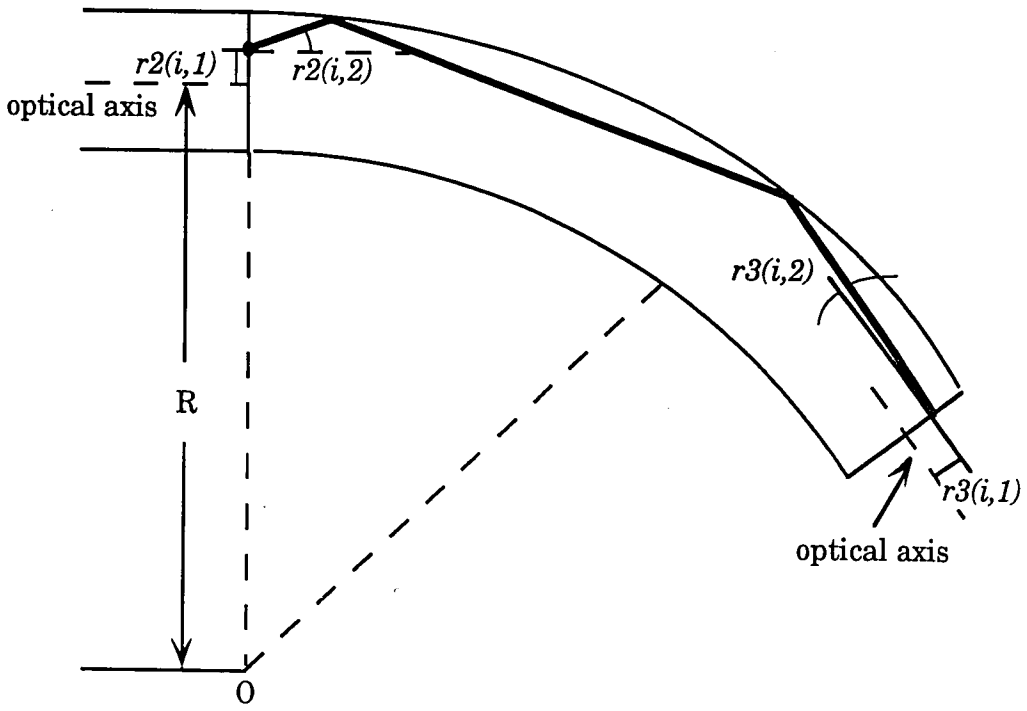

Figure 6.2 Cross section of a bending hollow-core fiber.

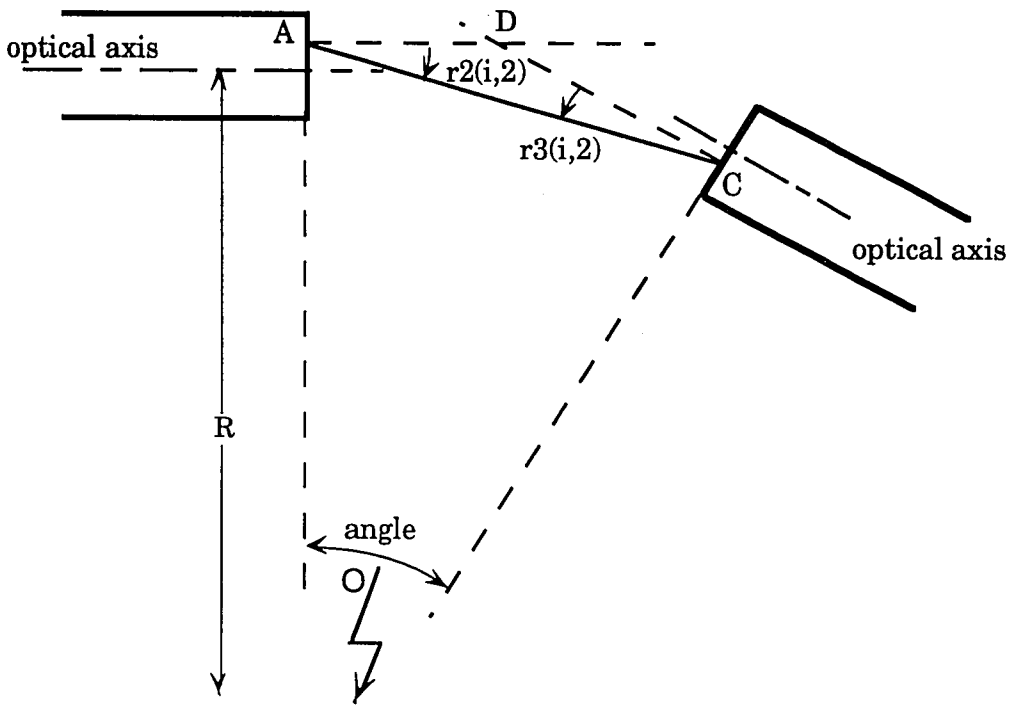

Figure 6.3 A bending hollow-core fiber when *r2(i,2)* and *r3(i,2)* are negative.

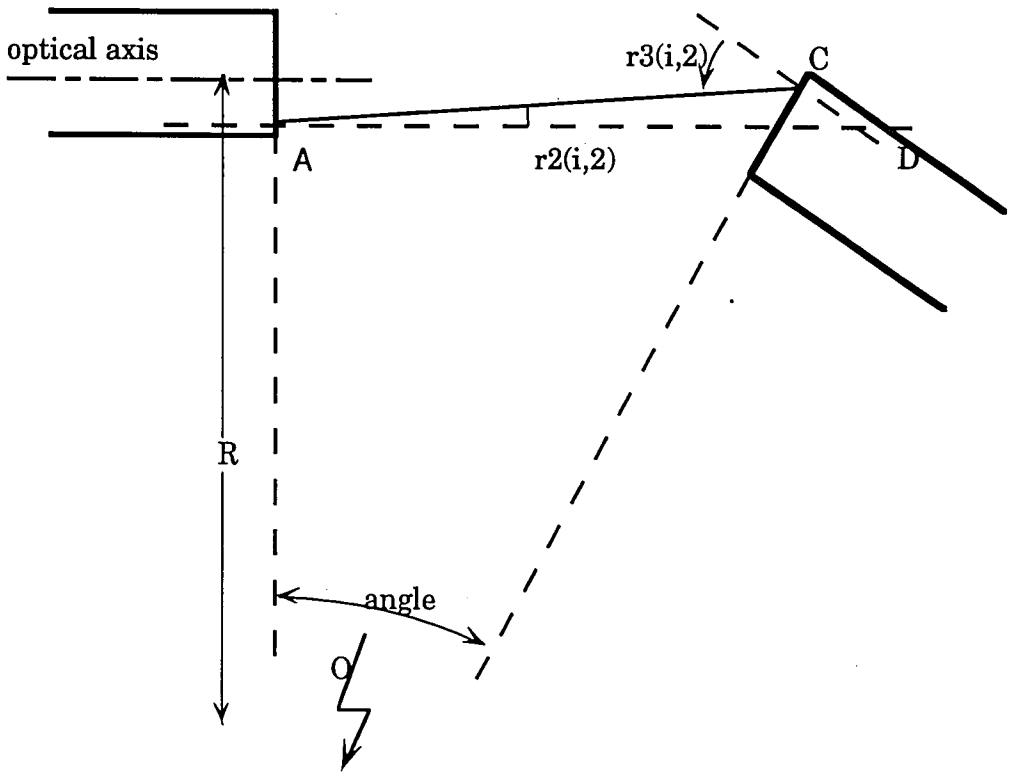

Figure 6.4 A bending hollow-core fiber when *r2(i,2)* is positive and *r3(i,2)* is negative.

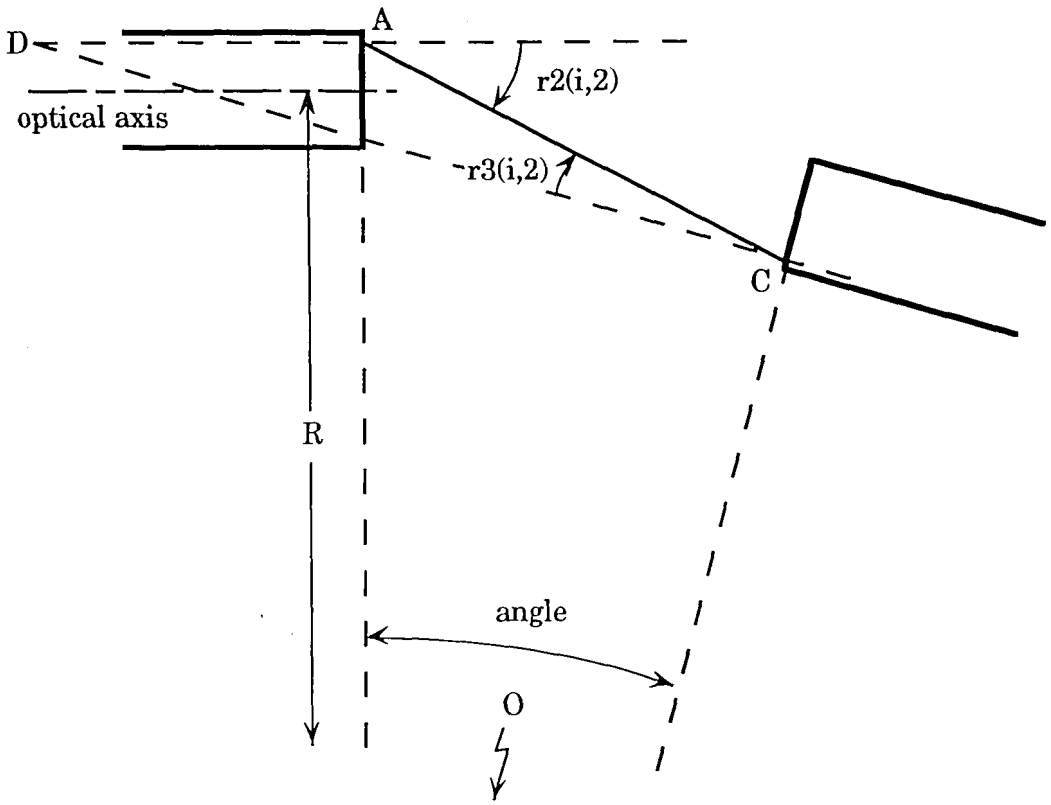

Figure 6.5 A bending hollow-core fiber when *r2(i,2)* is negative and *r3(i,2)* is positive.

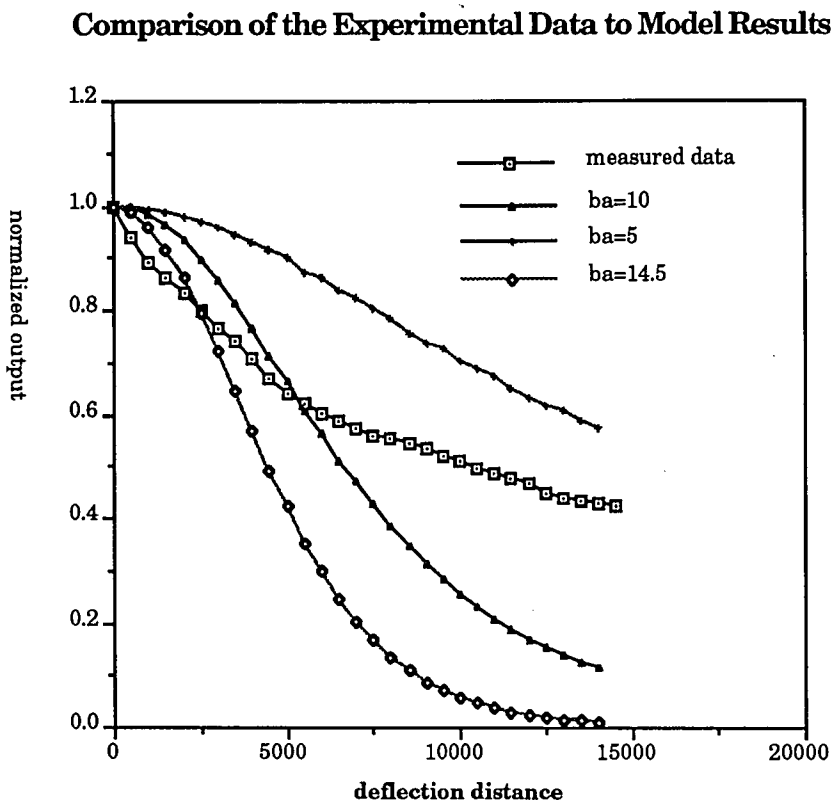

Figure 6.6 Comparison of the experimental data to model results.

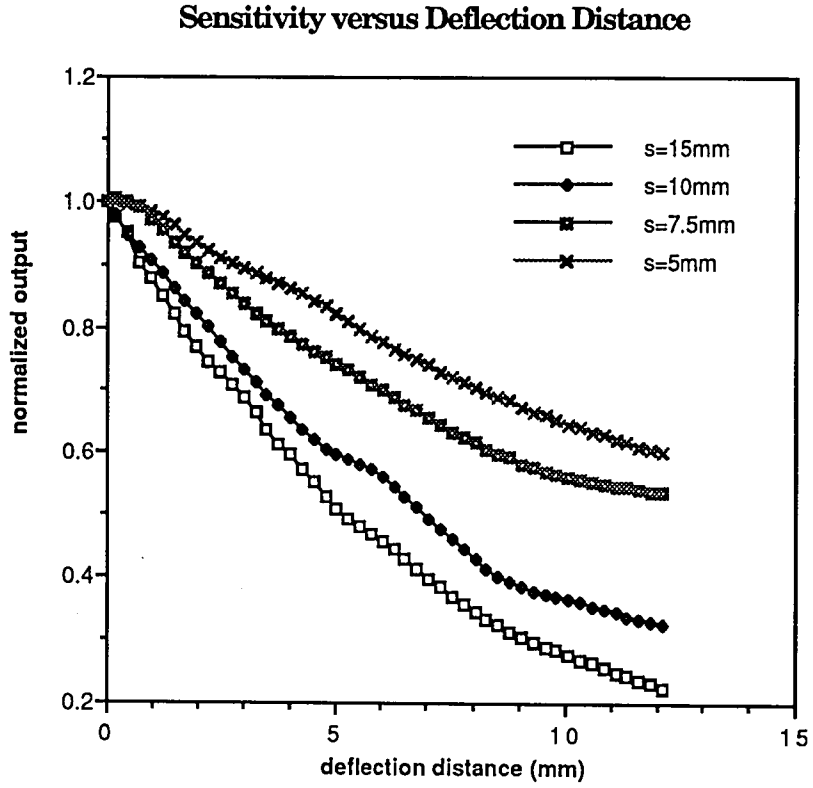

Figure 6.7 Sensitivity versus deflection distance.

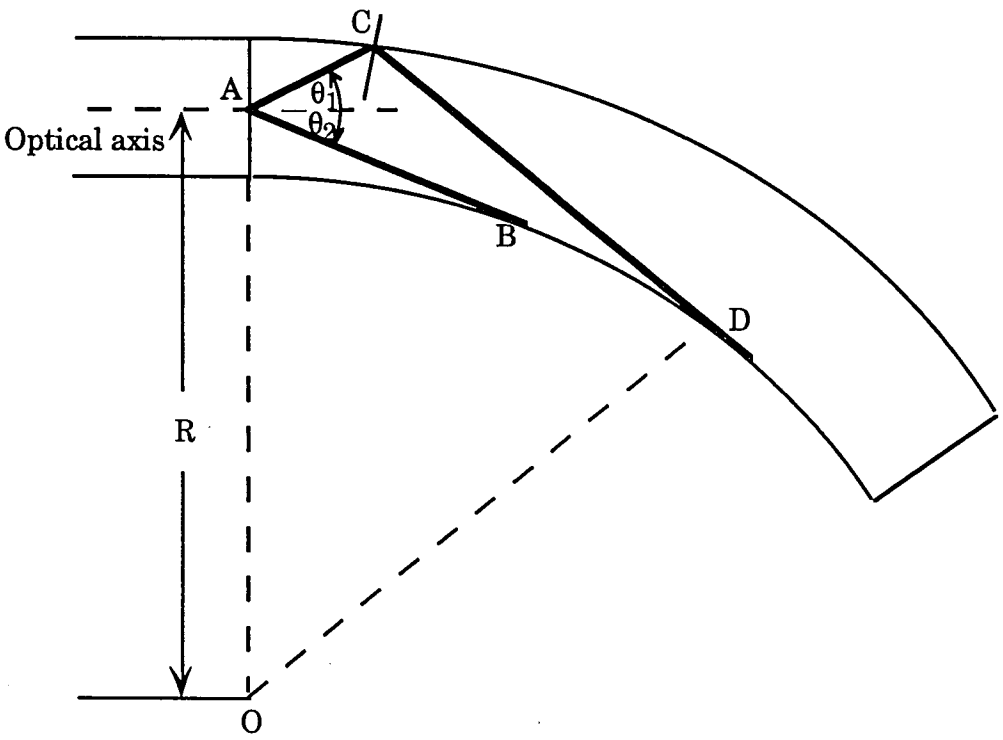

Figure 6.8 When the emission angle is larger than θ_1 or smaller than $-\theta_2$, the ray is a zigzag ray, while rays between θ_1 and θ_2 are whispering gallery rays.

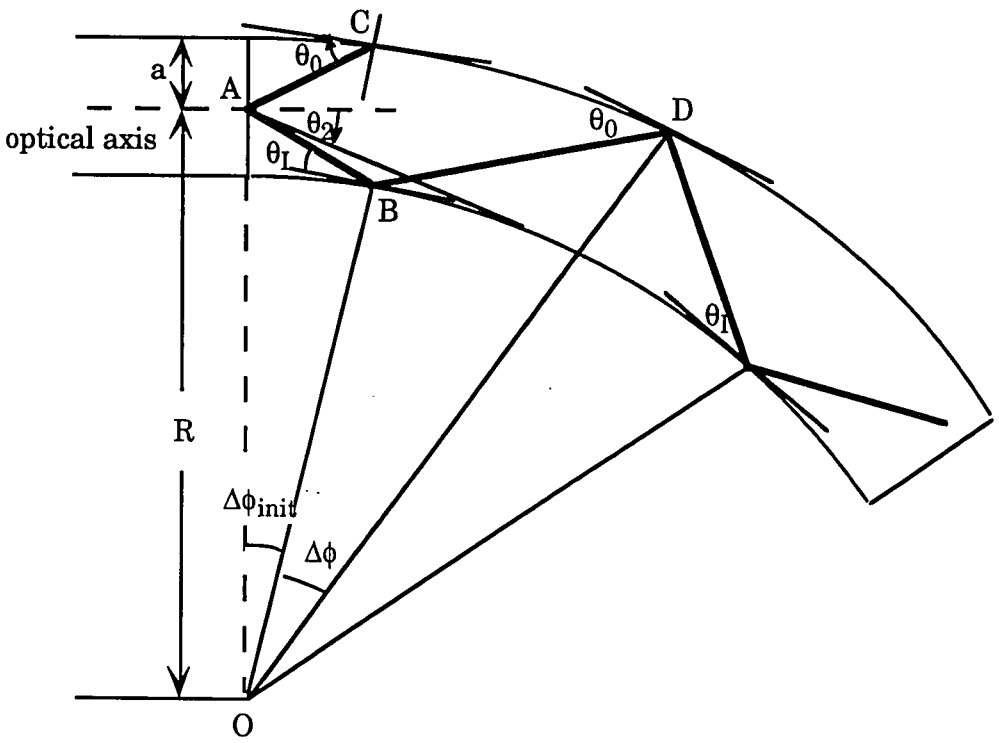

Figure 6.9 A bending hollow core fiber with the definition of $\Delta\phi_{init}$, $\Delta\phi$, θ_I, θ_0.

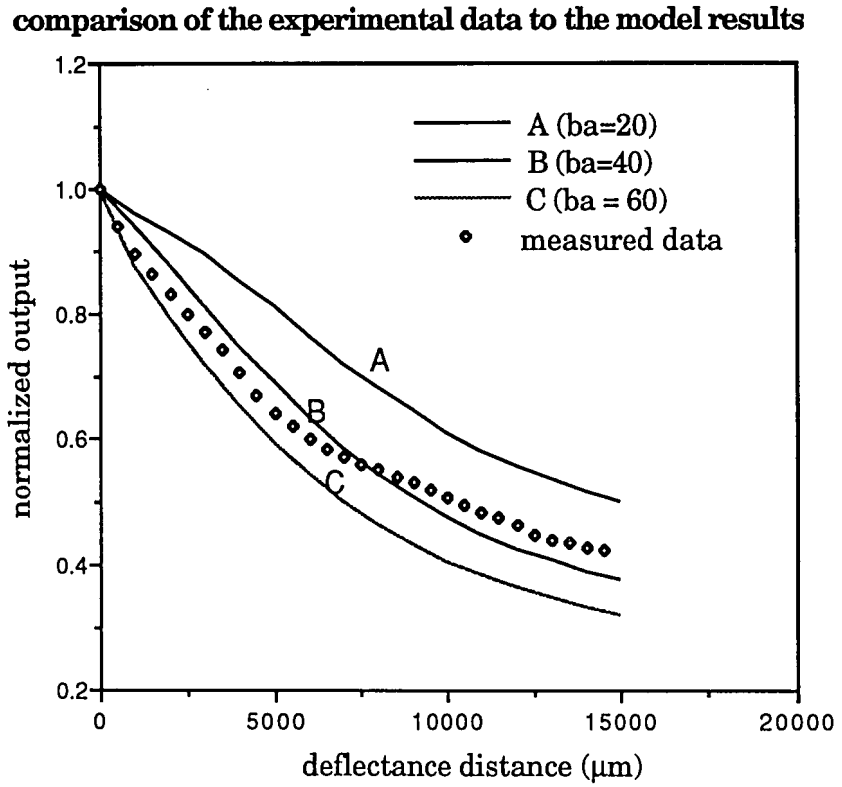

Figure 6.10 Comparison of the experimental data to the model results. solid lines are model curves, dot line is measured data.

7. Intensity Modulated Load Monitor

In the introduction section, we briefly mentioned that one goal of our work was to produce an intensity-modulated sensor. Before we introduce our device, we would like to review some intensity-modulated pressure sensors that other people have used.

7.1 Intensity Modulated Optical Fiber Pressure Sensors

Intensity-based sensors detect the variation of the intensity of the light as modulated by a perturbing environment. Fiber optic intensity are typically categorized according to one of three basic transduction mechanisms. These include the modulation of light which is transmitted between fibers, of light which is reflected from some object and is collected by a fiber, and of light which is lost due to microbending within a fiber. Each of these mechanisms will be briefly discussed below.

7.1.1 The Transmissive Sensor

Transmissive fiber optic pressure sensors have been divided into two basic categories. In the first category, the transmitting and receiving fiber legs remain fixed, and modulation occurs by an object partially obscuring the light path. In the second category, the fibers can move relative to each other to provide the modulation.

Figure 7.1 illustrates a transmissive sensor in which a shutter interrupts the light path in a manner proportional to pressure intensity. Using a reference and sensing channel provides ratiometric data with achievable full scale accuracies of 0.1%. Figure 7.2 shows a transmissive sensor in which a grating is placed in the optical path. One grating is fixed while the other moves due to pressure. As the grating spacing becomes smaller, the sensitivity increases, providing the most sensitive transmissive pressure intensity-modulated sensor known to have been reported [38,39].

The concept of frustrated total internal reflection is a modified transmissive concept. Two opposing probes have fibers polished at an angle

to the fixed axis, which produces total internal reflection for all propagating modes, as shown in Figure 7.3. As the fiber ends come close in proximity to one another, energy is coupled between them. This approach can produce a very high sensitivity transmissive sensor [40].

7.1.2 The Reflective Sensor

The reflective concept [41] is especially attractive for broad sensor use due to accuracy, simplicity, and potential low cost. The concept is shown in Figure 7.4. The sensor is comprised of two bundles of fibers or a pair of single fibers. One bundle of fibers transmits light to a reflecting target, the other bundle traps reflected light and transmits it to a detector. The intensity of the detected light depends on how far the reflecting target is from the fiber optic probe. It is a very precise, compact, noncontact displacement monitor. Therefore, this approach is ideal for monitoring a diaphragm that can move relative to a reflective fiber optic probe.

7.1.3 Microbending Sensor

All optical fibers will radiate energy when bent. The energy distribution in a bent fiber is shown in Figure 7.5. Theoretically, the energy field in the cladding extends to infinity. Therefore, at some radiation distance, X_r, the energy is implied to propagate at a velocity greater than the speed of light due to the longer travel path. Since this is not possible, the waveguide effect ceases. Subsequently, the energy is lost to radiation. The effect of microbending is shown in Figure 7.6. Light loss in the fiber depends on including a coupling from propagating modes in the fiber to radiation modes. When the fiber is distorted in such a way that the distortion has wave numbers equal to the difference in wave number between the propagating and radiating modes, strong loss occurs [42].

Most intensity modulated optical fiber sensors fall in one of the categories reviewed above. One problem often encountered with the extrinsic sensors is with dust, which may enter the sensor and block the light path, yielding incorrect results. The sensor that we are working on will overcome this problem. Next, we will introduce our device, which is

based on the deflection of a hollow core fiber to provide the intensity modulation.

7.2 Principle of Hollow Core Deflection Pressure Sensor

In order for the sensor to be environmentally stable, the sensing area must be entirely enclosed in some type of structure that can isolate the light path from the outside world. Hollow core fibers seem ideal for that purpose. As the name implies the core portion of the hollow core fiber is simply air, the refractive index of which is approximately 1.0. Since the refractive index of the cladding is always higher than 1.0, total internal refraction never takes place in a hollow core fiber. Therefore, once a ray reaches the air-cladding interface, most of it will be refracted into the cladding and no longer be confined to the core.

Figure 7.7 shows a preliminary design of the fiber optic load monitor. A hollow core fiber is embedded in an elastic material and held in a predetermined bend. Two multimode fibers are inserted into the two ends of the hollow core fibers. The hollow core fiber serves to splice the two solid core fibers, encapsulate the ray path between their ends, and provide a means through which light loss can take place. The light coming out of the transmitting fiber follows a Gaussian-like distribution across the diameter, with the maximum at the midpoint of the diameter. When the hollow core fiber is bent, the two solid core fibers are angled with respect to each other, and the amount of light that enters the receiving fiber will vary according to the angle between the transmitting and receiving fibers. If the pressure is directed upwards, the hollow core fiber is straightened so that more light is transmitted through it; if the pressure is in the opposite direction, less light will go through. Hence, not only the magnitude, but also the direction of the load monitor can be readily detected.

7.3 Experimental Set Up

7.3.1 Optical Sources

Light sources are used to convert electrical signals to light that is to be launched into the fiber. This conversion process is called electroluminescence. The principal light sources used for fiber optic

communications and sensing are heterojunction-structured semiconductor laser diodes (LDs) and light emitting diodes (LEDs). A heterojunction consists of two adjoining semiconductor materials with different band gap energies. LDs and LEDs are suitable for fiber transmission systems because (a) their optical output can be modulated by their input current or voltage, (b) their output power is sufficiently high for a wide variety of applications (c) they have a high efficiency, and (d) their dimensional characteristics are compatible with those of the optical fiber [43].

The basic semiconductor hardware is the same for both LEDs and LDs. Pure semiconductors can be made into n-type material which has an excess of conduction electrons, while p-type semiconductors posses extra holes acting as positive charge carriers. When these two materials are placed side by side in a single, continuous structure, a pn junction is formed between them. Because of the difference in electron and hole densities across the junction, holes diffuse from the p side to the n side, and electrons diffuse from the n side to the p side. As a result of this diffusion process, an electric field (barrier potential) appears across the junction. This field prevents further net movements of charges once equilibrium has been established. The junction area then has no mobile carriers and, therefore, is called the depletion region.

When the p side is biased at a higher potential than the n side (when the pn junction is forward-biased), the magnitude of the barrier potential is reduced. Electrons from the n side and holes from the p side, called majority carriers, are allowed to diffuse across the junction and become minority carriers on the other side (they number less than the oppositely charged majority carriers). The excess minority carriers then recombine with the majority carriers, and optical radiation is generated. The amount of light generated can be controlled by the biasing voltage, which determines the amount of diffusion of majority carriers to the opposite sides. If the n side is biased at a higher voltage than the p side (when the pn junction is reverse-biased), then light emission can be completely stopped.

A major difference between LEDs and LDs is that the optical output from an LD is coherent, meaning that all waves emitted are in phase and travel in the same direction, whereas the light produced by an LED is incoherent. In a coherent source the phase of the optical energy is strongly correlated from one part of the beam to another, in addition, the light is

highly monochromatic (possessing only one frequency), and the output beam is highly directional. In an incoherent LED source, no optical cavity exists for wavelength selectivity. The energy of the output light is distributed over a broad frequency spectrum and a broad emission pattern. Hence the incoherent LED output rays have a large beam divergence.

The spatially directed coherent optical output from an LD can be coupled into either single mode or multimode fibers. In general, LEDs are used with multimode fibers, since normally the diverging incoherent light from an LED can be coupled only into a multimode fiber in sufficient quantities to be useful. Some fiber optic sensors take advantage the ability of laser light to distribute power among its different modes while propagating in a fiber. In some sensors, such modal power distribution is avoided to eliminate modal interference.

7.3.2 Optical Receivers

Photodetectors are devices that convert optical signals into equivalent electrical wave forms. In fiber optic sensors, as well as in optical fiber communication systems, reverse-biased pn junction devices are used as photodiodes. Two commonly used photodiodes are the *pin* and the avalanche photodiode (APD). Photodiodes convert incoming photons into electro-hole pairs in a regeneration time on the order of 10^{-10} seconds. Physical processes performed by these devices are exactly the reverse of light emission in a semiconductor. In most cases, the output from the photodiode is very weak and often requires amplification and signal processing. Therefore, a typical optical receiver consists of a photodiode, an amplifier, and some type of filtering circuits.

Pin photodiodes are the most commonly used semiconductor photodetector. The structure of the device consists of p and n regions separated by a very lightly n-doped intrinsic region (i region). In normal operation, a sufficiently large reverse-bias voltage is applied across the device so that the intrinsic region is fully depleted of carriers.

When an incident photon has an energy greater than or equal to the band-gap energy of the semiconductor material, the photon can give up its energy and excite an electron from the valence band to the conduction band. The process generates free electron-hole pairs which are known as

photocarriers, since they are photon-generated charge carriers. The photodetecter is normally designed so that these carriers are generated mainly in the depletion region (the depleted intrinsic region) where most of the incident light is absorbed. The high electric field present in the depletion region causes the carriers to separate and be collected across the reverse-biased junctions. This gives rise to a current flow in an external circuit, with one electron flowing for every carrier pair generated. This current flow is known as the photo-current, which is usually fed into some amplification and filtering circuitry.

7.3.3 Emitter-Detector Circuitry

The Emitter-Detector which we are using was built by a former student in this lab. The circuit is capable of both generating and detecting optical signals. In order to maximize the output of the LED without loading the circuit with too much current, a test was done to measure the optical output of the LED against the amount of current going through it. The input current was set at 120 mA (assuming a 5V input voltage) such that the corresponding optical output is 80% of the maximum. Thus, in exchange for a small reduction in the output, the current in the circuit is decreased by 40%, giving the circuit a greater safety margin.

Many modifications were made to improve the overall performance of the circuit. The final version of the circuit is illustrated in Figure 7.8. It includes one LED and two transimpedance amplifier circuits, which utilize the dual op amps on an LF353N integrated circuit chip. The two amplifier circuits have different gains so that the circuit can detect both strong and weak signals without becoming saturated. The entire circuit is encased in a $5 \times 4 \times 3$ (in^3) aluminum box. The box houses a transformer and uses standard AC power supply. An external modulator input jacket is installed so that the user may switch between constant and modulated LED output. A simple array of zener diodes provides voltage regulation for the LED.

7.3.4 Pressure Sensor Testing and Construction

Using the emitter-detector circuit box, a number of tests were conducted to correlate bending on a hollow core fiber to the amount of light

transmitted over it. Two normal fibers stripped of their jacketing at the ends were inserted into a hollow core fiber. All three fibers were glued to an aluminum beam, which was simply supported at both ends. Constant-intensity light from the LED was launched into one optical fiber, and the output from the other fiber was monitored. A micropositioner pressed the beam at the midpoint. As the beam was bent, so was the hollow core fiber, and the light output was reduced.

According to the results of our computer program, for the best sensitivity, graded-index fiber, rather than step-index fiber, and 10 mm fiber end separation gap were chosen, and two identical solid core fibers with 100/140 μm core-cladding diameter and hollow core fiber with 145 μm inner core diameter were used in the device.

A piece of thin, pliable spring steel was cut, bent to shape, and two solid core fibers were stripped of their jacketing and inserted into the ends of the hollow core fiber. All three fibers were then glued to the metal, and the entire setup was laid in a mold. Silicone rubber (type RTV108) was poured into the mold and allowed cure. After about two days, the glue-like silicone rubber had solidified into a translucent and elastic parallelepiped of $5/8 \times 2 - 5/16 \times 3/4$ (inch^3), with fibers leading out of its two ends.

A test was performed to determine whether the sensor underwent elastic deformation when placed under a load. The sensor was put in a press and applied load was increased in steps of 20 lb. The change in the thickness of the sensor was measured and plotted against the amount of force applied to the sensor, as shown in Figure 7.9. There are clearly two distinctively different regions in the curve. Below 100 lb of load, the deformation is roughly linear with load. Taking into account possible experimental error introduced by the limited precision of the press, this region can be considered essentially linear. Therefore, under relatively light loading the sensor exhibited elastic deformation.

The output of the sensor was measured along with its physical deformation in the same static setting. The result is displayed in Figure 7.10. The plot is roughly linear over the entire range of applied load, but under 100 lb it seems to be smoother than at greater values. The curve suggests that, at lighter levels of loading, the sensor deformed more elastically than it did at heavier levels of loading. This result led to the

conclusion that the compressive load on the sensor should be adjusted to vary between 0 and 100 lb, with the equilibrium point being about 50 lb.

7.3.5 Accelerometer Testing Set Up

The hollow core bending sensor was also include in a preliminary design for an accelerometer. A sensor head having a 9 mm gap was bonded to a thin strip of spring steel, which was then attached to a stiff vibrating beam in a cantilevered fashion, as depicted in Figure 7.11(a). In this vibration system, the natural frequency of just the sensor portion was measured at 3.5 Hz, and was nearly undamped, with a fraction of critical damping coefficient of $\zeta = 0.015$. The time and frequency response of the sensor when an impulse force was applied to the structure beam appears in Figure 7.11(b). As seen in the figure, the beam frequency driving the sensor was 11.175 Hz; even with the low damping, the acceleration response factor R_a is nearly unity for this driving to natural frequency ratio, meaning that the sensor responded essentially in the mode of a displacement meter, where

$$R_a = \left(\frac{\omega}{\omega_n}\right)^2 \frac{1}{\sqrt{[1 - (\omega/\omega_n)^2]^2 + [2\zeta\,\omega/\omega_n]^2}} \quad ,$$

ω_n is sensor natural frequency, and ω is vibrational angular frequency [44]. This device could be improved by a better mechanical design to utilize the maximum vibration dynamic range with minimum damping problem coming from the environment. However, it serves to illustrate that the hollow core sensor idea could in fact be applied to a number of different sensing situations.

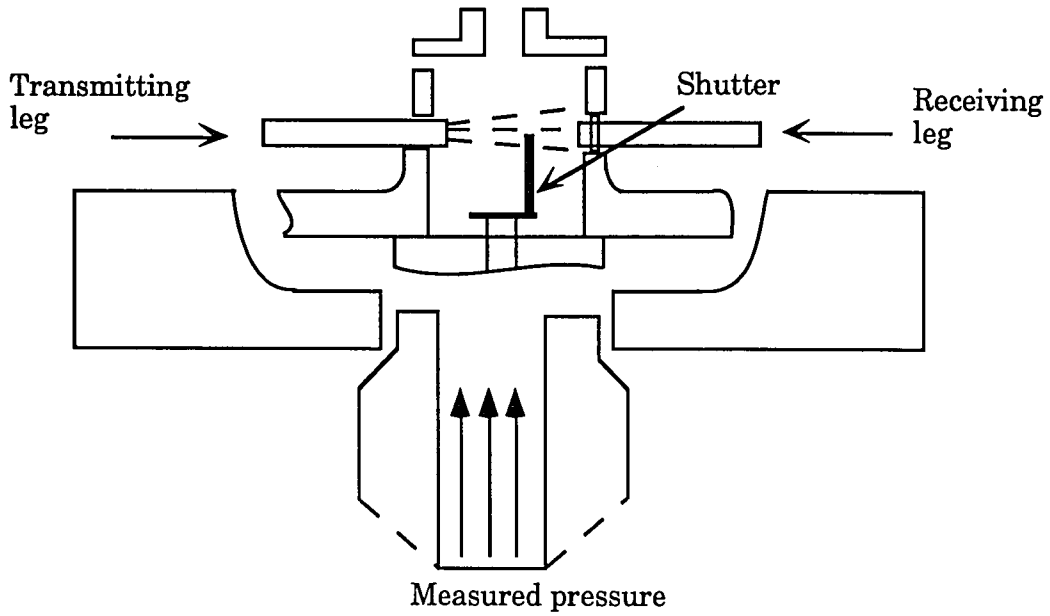

Figure 7.1 Transmissive fiber optic pressure using a shutter to modulate the intensity [38].

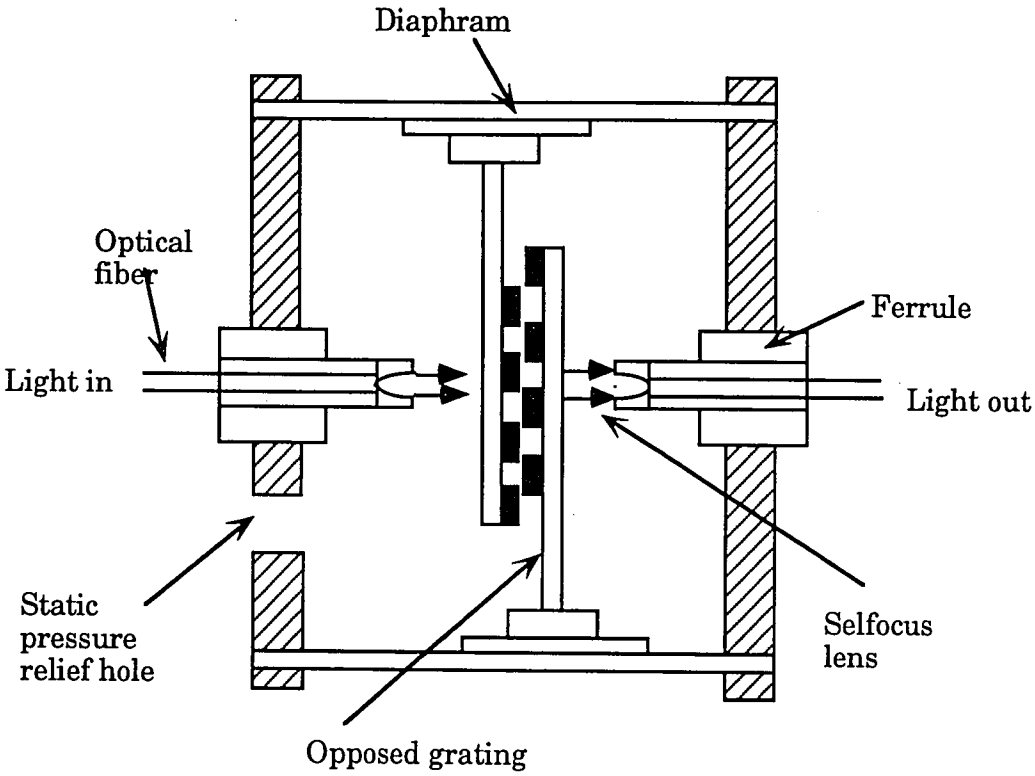

Figure 7.2 Transmissive fiber optic pressure using a moving grating to modulate the intensity [39].

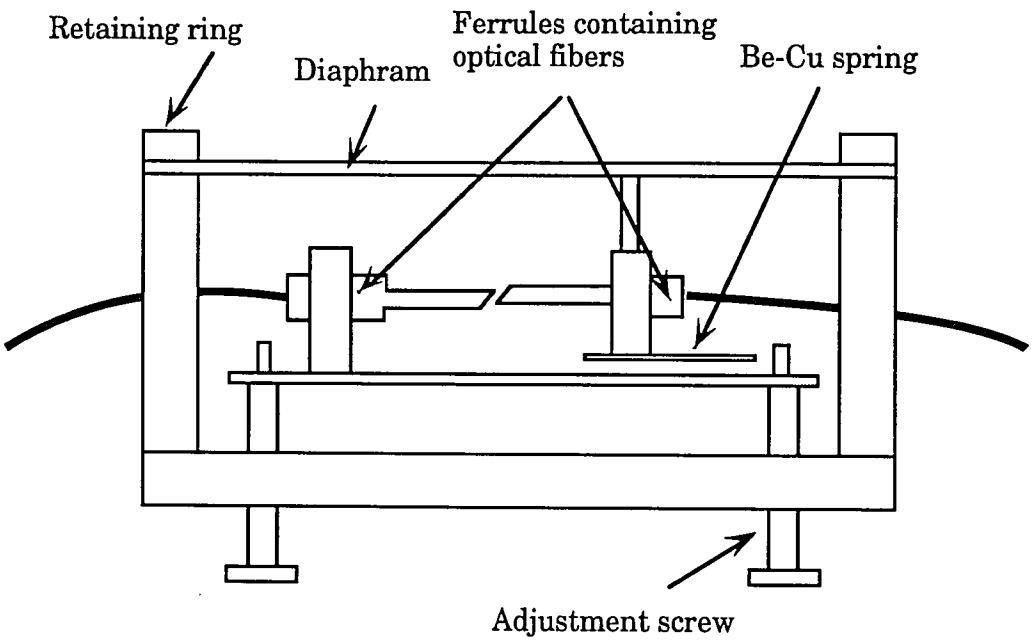

Figure 7.3 FTIR pressure sensor [40].

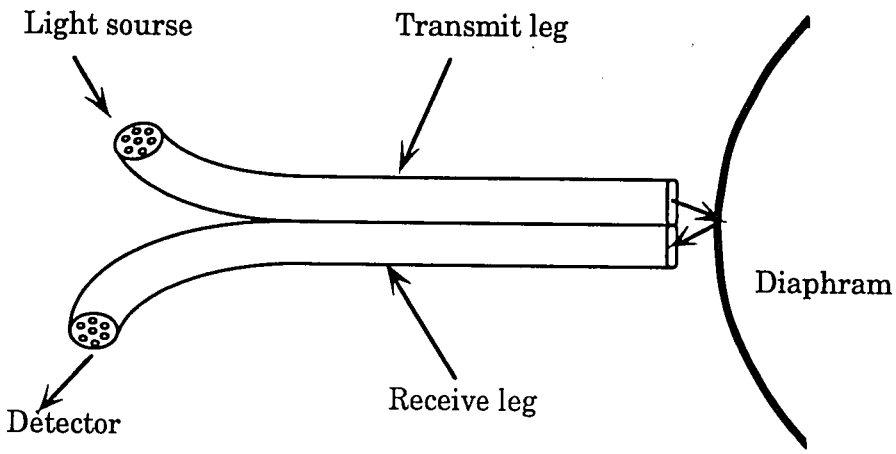

Figure 7.4 Reflective fiber optic pressure sensor using a diaphragm for modulation [41].

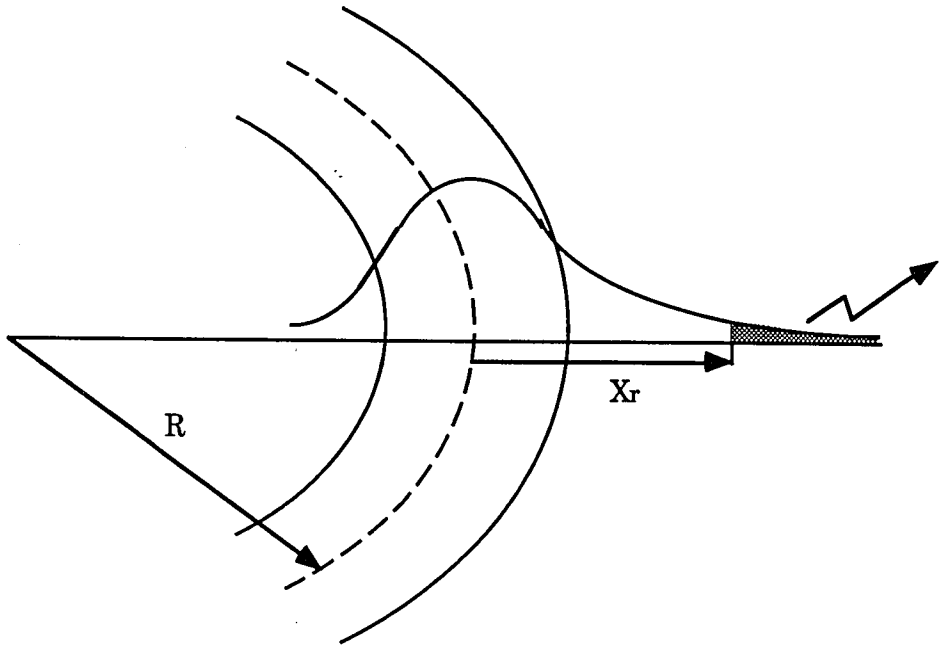

Figure 7.5 Power loss mechanism in bending [43].

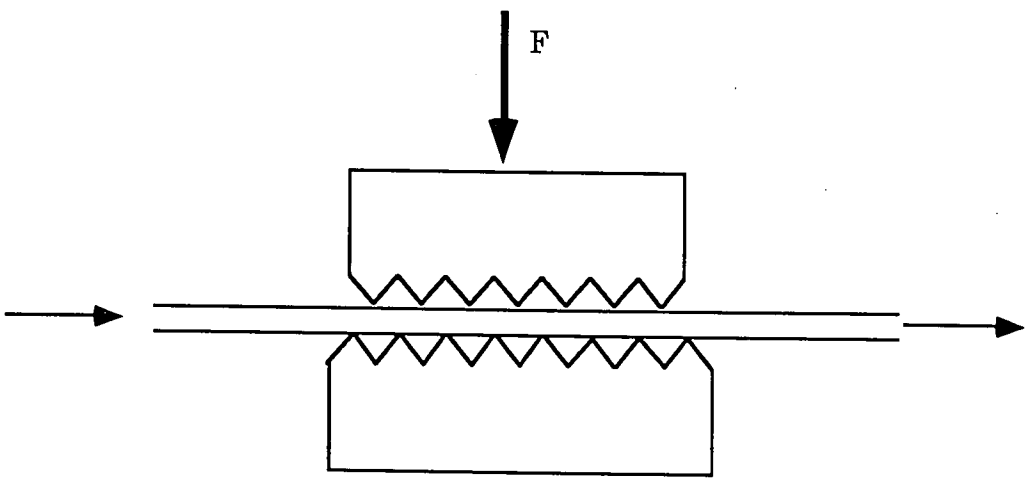

Figure 7.6 Microbending pressure sensor.

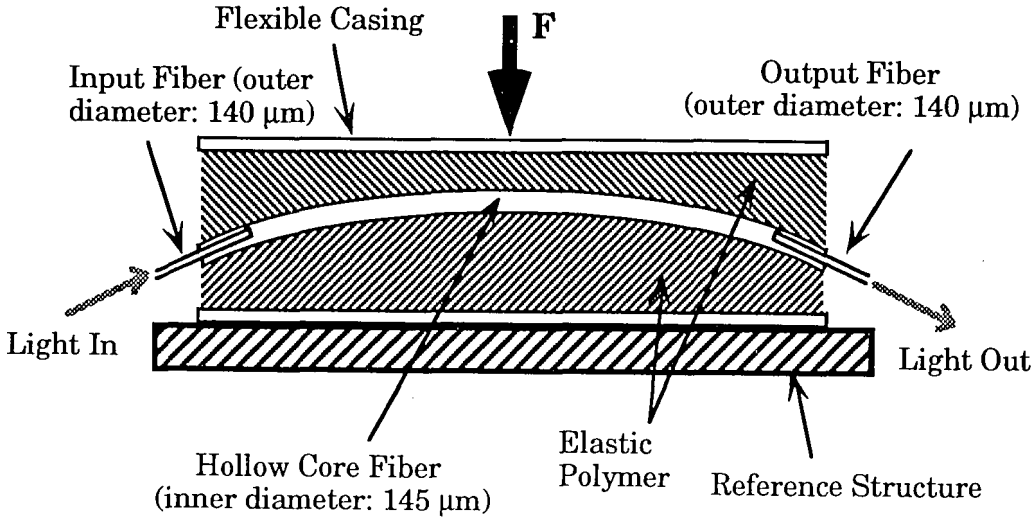

Figure 7.7 Hollow core bend sensor concept. The hollow core fiber is attached to a metallic strip, and a bias bending is applied before the assembly is potted in an elastic polymer.

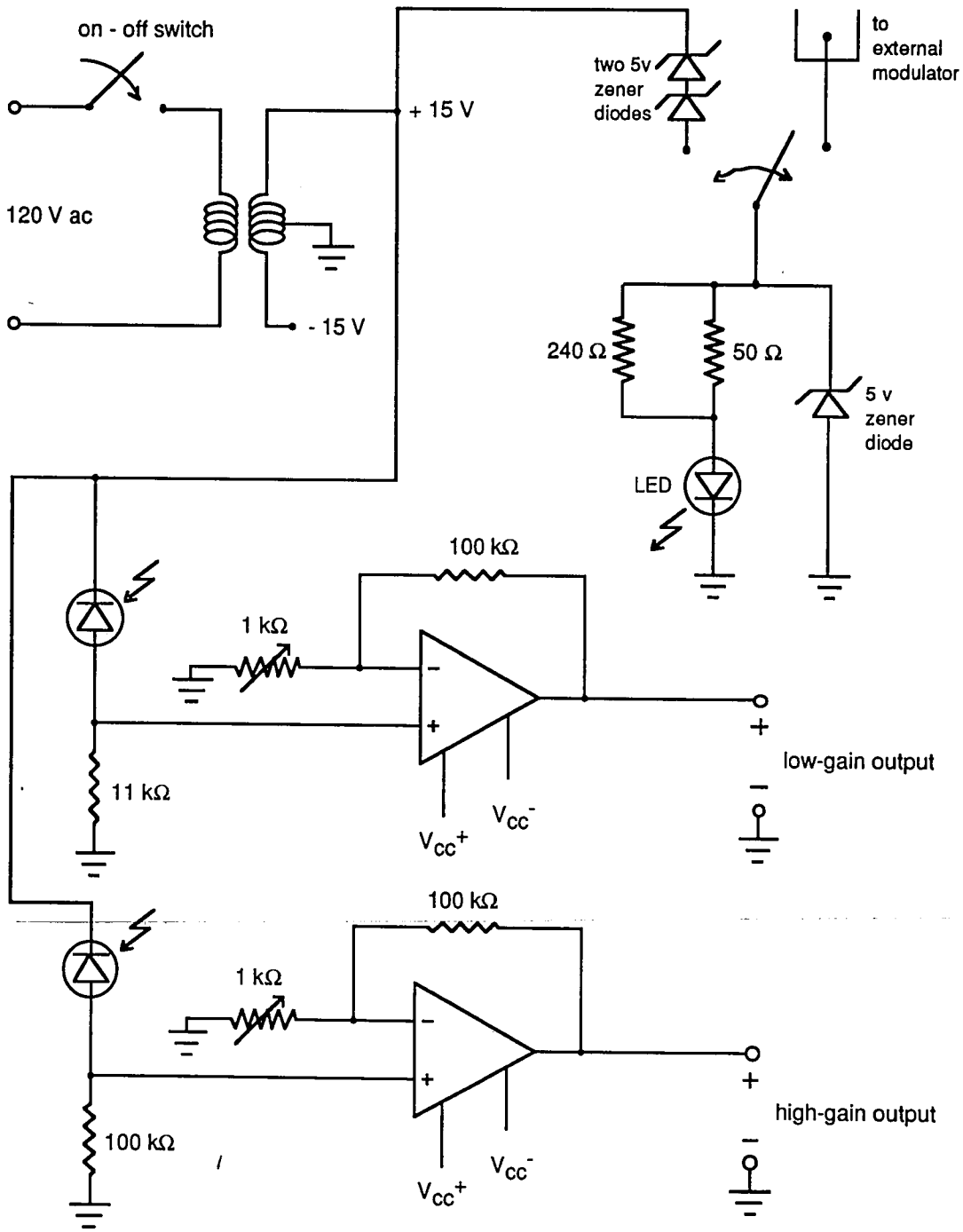

Figure 7.8 Emitter-receiver circuit diagram.

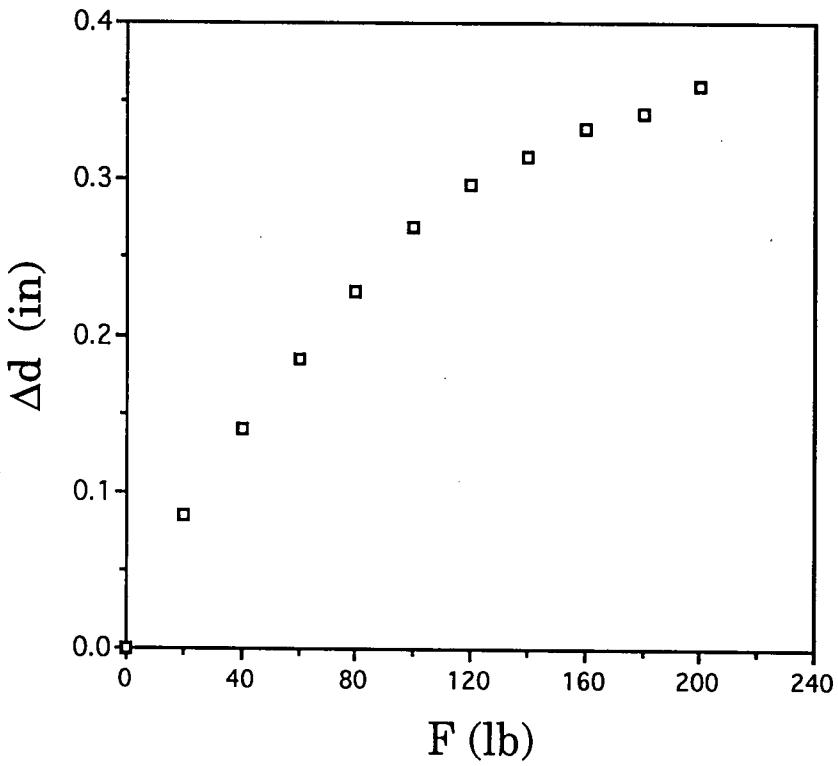

Figure 7.9 The change in the thickness of the sensor head, Δd, is plotted against the amount of force applied to the sensor head, F.

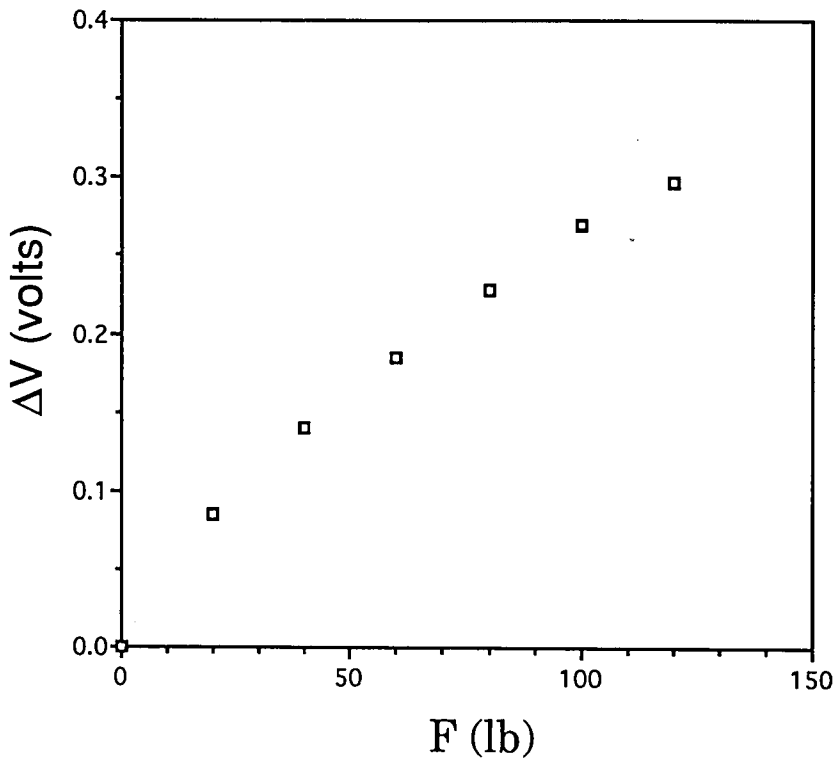

Figure 7.10 ΔV, the change in the output voltage, is plotted against the amount of force applied.

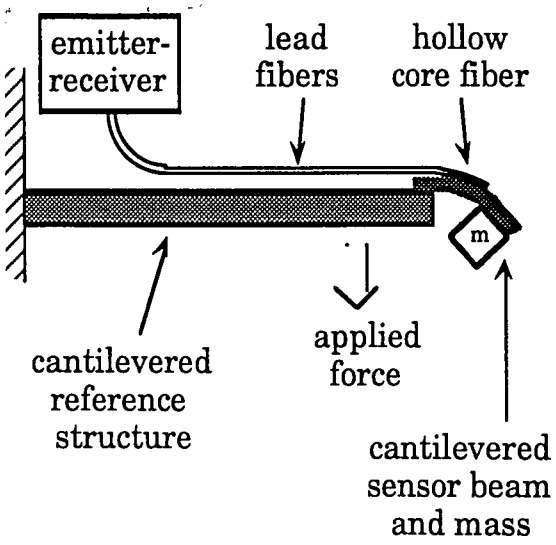

(a)

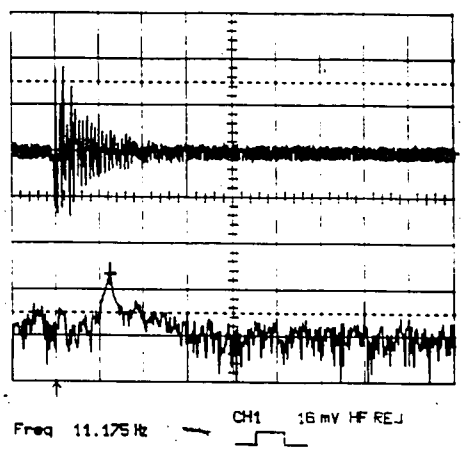

(b)

Figure 7.11 (a) A proof-of concept test in which the natural frequency of the sensing element was set at about one-third of that of the driving frequency. Bias bending in this case is applied by gravity acting on the mass. (b) Time and frequency response of the sensor when an impulse force was applied to the reference structure.

8. Conclusions

Crucial work was developed to model the sensor behavior from the point of view of fiber optic theory, as well as using a ray trace programming approach. Two approaches were taken to demonstrate the unique characteristics of this fiber sensor mechanism. The computer simulation was expanded to model the light emitted from the transmitting fiber end face, trace the light as it propagates through a certain length of bent hollow core fiber, and calculate the amount of power captured by the receiving multimode fiber. Based on the results calculated by the program, the effect of changing various sensor parameters was studied, including fiber type, diameter, numerical aperture, end separation, and launching condition. It was found that the sharper refractive index profile and power distributions with more lower order modes give better sensitivity, while neither changing the diameter nor the numerical aperture of the transmitting and receiving fibers apparently affect the sensitivity.

A number of advantages result from building a sensor around measuring the tilt loss between fibers in a bent hollow core optical fiber. For one, this sensor construction is innately simple, which includes two solid core optical fibers, one hollow core fiber, LED source, and photodetector. For another, the tight tolerances available with this configuration make for accurate alignment between fibers, even over large fiber end separation. These tolerances, as well as the ability to embed the hollow core fiber in a protective medium, also allow the sensor to be free from intrusive particles, and be readily compatible with hermetic sealing if deemed necessary. Furthermore, the mating of ordinary and hollow core fiber involves a small and flexible geometry, so that the sensor can be integrated into a wide variety of device designs as appropriate for different sensing tasks.

Two implementations have been fabricated which utilize the hollow core bend sensor concept. In one the sensor acts as a load monitor, and in the other it performs as an accelerometer. Both devices operate as satisfactory proof-of-concept prototypes. Nearly as important, an experimental procedure for working with hollow core optical fiber-based sensors has been established for future research.

Notwithstanding, more development is required in order to realize the goal of making a practical and cost effective sensor which is rugged enough for field use. Especially, development is needed to miniaturize the design as much as possible, increase the signal-to-noise ratio, and explore more sensor configurations suitable for practical applications. Future work includes the possible extension to multidirectional and/or rotational sensing, and a quasi-distributed network of several devices interrogated using optical time domain reflectometry.

REFERENCES

1. F. L. Thiel and R. M. Hawk, "Optical waveguide cable connection," Applied Optics, Vol. 15, pp. 2785-2791, 1976.

2. F. L. Thiel and R. M. Hawk, "Optical waveguide cable connection," Erratum," Applied Optics, Vol. 16, pp. 1468, 1977.

3. H. Tsuchiya, H. Nakagome, N. Shimizu, and S. Ohara, "Double eccentric connectors for optical fibers," Applied Optics, Vol. 16, pp. 1323-1331, 1977.

4. P. Di Vita and U. Rossi, "Theory of power coupling between multimode fibers," Optical and Quantum Electronics, Vol. 10, pp. 107-117, 1982.

5. B. E. A. Saleh and M. C. Teich, *Fundamentals of Photonics*, Series in Pure and Applied Optics, John Wiley & Sons, Inc., New York, 1991.

6. A. W. Snyder and J. D. Love, *Optical Waveguide Theory*, Routledge, Chapman and Hall, New York, 1984.

7. R. L. Gallawa, *A User's Manual for Optical Waveguide Communications*, Publication No. OTR76-83, U.S. Dept. of Commerce, Washington, D.C., 1976.

8. H. G. Unger, *Planar Optical Waveguides and Fibers*, Clarendon, Oxford, 1977.

9. A. W. Snyder, D. J. Mitchell, "Generalised Fresnel's Law for Loss Due to Curvature," Electronics Letters, Vol. 9, pp. 609-610, 1973.

10. A. W. Snyder, J. D. Love, "Reflection at a Curved Dielectric Interface - Electromagnetic Tunneling," IEEE Transactions on Microwave Theory And Techniques. Vol. MTT-23, No.1, 1975.

11. D. Marcuse, *Light Transmission Optics*, Van Nostrand Reinhold, New York, pp. 16, 398, 1972.

12. M. Abromawitz and I. A. Stegun, Eds., *Handbook of Mathematical Functions*, GPO, Washington, D. C., Sec. 10.4, 1964.

13. D. Marcuse, "Excitation of the dominent mode in round fiber by a Gaussian beam," Bell Syst. Tech. J. 49, pp. 1665-1693, 1970.

14. D. Marcuse, "Loss analysis of single-mode fiber splices," Bell Syst. Tech. J. 56, pp. 703-718,1977.

15. D. Marcuse, "Gaussian approximation of the fundamental modes of graded-index fibers," J. Opt. Soc. Am. 68, pp. 103-109, 1978.

16. W. A. Gambling, H. Matsumura, "Jointing loss in single modefibers," Electron. Lett. 14, pp. 491-493, 1978.

17. H. Kogelnik, "On the propagation of Gaussian beams of light through lenslike media including those with a loss or gain variation," Appl. Opt. 4, pp. 1562-1569, 1965.

18. E.–G. Neumann, *Single Mode Fibers*, Springer-Verlag, Berlin, 1988.

19. W.T. Anderson, D.L. Philen, "Spot size measurements for single-mode fibers - a comparison of four techniques," J. Lightwave Tech. LT-1, pp. 2026, 1983.

20. R. Caponi, "Spot size measurements in single mode fibers," Symp. Opt. Fiber Meas, NBS spec. publ. 683, pp. 37-40, 1984.

21. D. Marcuse, "Loss analysis of single-mode fiber splices," Bell Syst. Tech. J. Vol. 56, pp. 703-718, 1977.

22. D. Marcuse, "Gaussian approximation of the fundamental modes of graded-index fibers," J. Opt. Soc. Am. Vol. 68, pp. 103-109, 1978.

23. W. A. Gambling, H. Matsumura, "Jointing loss in single modefibers," Electron. Lett. Vol. 14, pp. 491-493, 1978.

24. K. Petermann, "Microbending loss in monomode fibers," Electron Lett. Vol. 12, pp. 107-109, 1976.

25. K. Petermann, " Fundamental mode microbending loss in graded-index and W- fibers," Opt. Quantun Electron. Vol. 9 , pp. 167-175, 1977.

26. W. J. Stewart, "Simplified parameter-based analysis of single-mode optical guides," Electron. Lett. Vol. 16, pp. 380-382, 1980.

27. K. Petermann, "Mode field characteristics of single mode fiber designs," Conf. Opt. Fiber Commun, TUA1, 1987.8

28. J.H. Povlsen, "Analysis on splice-, microbending-, and Rayleigh losses in GeO2 doped, dispersion-shifted, single-mode fibers," 11th Europ. Conf. Opt. Commun. pp. 321-324, 1985.

29. J. Streckert, "A new fundamental mode spot size definition usable for non-Gaussian and noncircular field distribution," J. Lightwave Tech. LT-3, pp. 328-331, 1985.

30. C. M. Miller, *Optical Fiber Splice and Connectors*, Marcel Dekker, Inc., New York, 1986.

31. M. J. Adams, D. N. Payne, and F. M. E, Sladen, Appl. Phys. Lett. Vol. 28, pp. 524, 1976.

32. D. Gloge, Bell Syst. Tech. J., Vol 55, pp. 905, 1976.

33. P. DiVita, and U. Rossi, Opt and Quantum Elect., Vol. 10, pp. 107, 1978.

34. C. M. Miller, Bell Syst. Tech. J., Vol. 55, pp. 917, 1976.

35. J. A. Arnaud, W.M. Hubbard, "Technique for Fast Measurement of Gaussian Laser Beam Parameters," Applied Optics, Vol. 10, No. 12, pp. 2775-2776, 1971.

36. C. Saravanos and R. S. Lowe, "The Measurement of Non-Gaussian Mode Field by the Far-field Axial Scanning Technique," Journal of Lightwave Technology, Vol. 10, pp. 1563-1566, 1986.

37. J. M. Dick, "Automated-mode radius measurement using the variable aperture method in the far field" Conf.Opt. Fiber Commun. (OFC'84), pp. 90-91, 1984.

38. Anonymous, "Non-Contacting Optical Sensor," Bulletin HE/S-1, Dresser Industries.

39. J.H. Portor, and D. B. Murray, "Fiber Optic Pressure Detector," U.S. Patent 3, 686, 958, 1972.

40. C. D. Kissenger, B. Howland, "Fiber Optic Displacement Measuring Apparatus," U.S. Patent 3, 940,608, 1976.

41. A. K. Bejczy, H. C. Primus, W. A. Herman, "Fiber Optic Proximity Sensor", NSSA tech. Brief, Vol 4, No.3, Item 63, JPL Report NPO-14653/30-4279.

42. J. N. Fields, J. H. Cole, "Fiber microbending acoustic sensor," Appl. Opt., Vol. 19, pp. 3265-3267, 1980.

43. G. Keiser, *Optical Fiber Communications*, McGraw-Hill, Inc., New York, 1993.

44. G. V. Berg, *Elements of Structural Dynamics*, Prentice Hall, Englewood Cliffs, New Jersey, 1989.

45. B. Prantil, "Fiber Optic Pressure Transducer," Senior Design Project Report, Lafayette College, May 1994.

Appendix

Program 1

```
c This program models the loss of light as a function of displacement
c between two step index fiber ends.  It is essentially a ray tracing
c program with some Jones matrix notation thrown in.
c23456789 123456789 123456789 123456789 123456789 123456789 123456789 12

      integer i, j, k, l, m, n, ix, mx, itot
      integer psteps, asteps, ptot, atot, rows, cntr
      real n0, a1, a2, lamda, xsteps, fftest
       real alpha1, alpha2, aldeg1, aldeg2, d, s
      real NA1,NA2, V1, V2, ba, bp, eneg1, NAmax
      real pinc, ainc, xinc, totpow, intot, endpow
      real inppow(6561,3), outpow(6561,3), ffield(1000,2)
      real r2(6561,3), r3(6561,3)

      write (9,*) "YOUR PROGRAM IS RUNNING"

c initialize data file and variable values:

      OPEN(13,FILE='inp.DAT',STATUS='NEW')
      OPEN(14,FILE='ffi.DAT',STATUS='NEW')
      OPEN(15,FILE='d.DAT',STATUS='NEW')
      OPEN(16,FILE='end.DAT',STATUS='NEW')
      OPEN(17,FILE='ex.DAT',STATUS='NEW')

c The vector inppow holds the input power at each position and angle.
c A total of 25 steps along diameter(12 along radius plus one in the
c center) are allowed and 25 angles are allowed at each position.  Thus
c inppow is a matrix with 25**2 rows, and three columns; the first for
c the position, the second for the angle, the third for the power at
c that position and angle.
c always remember rn(i,3) is the power, even though we use r.


      do 6 i = 1,6561
        do 5 j = 1,3
          r2(i,j) = 0.0
          r3(i,j) = 0.0
5       continue
6     continue
      do 7 i = 1,1000
        ffield(i,1) = 0.0
        ffield(i,2) = 0.0
7     continue

c psteps can at most be 40, asteps can at most be 40 .

      pi = 3.14159265358
      psteps = 10
      asteps = 150
      xsteps = 10
```

```
      xinc = 80
      bp = 0.0
      ba  = 14.5


c These are the independent fiber variables:

      fftest = 0
      NA1 = 0.29
      a1 = 50.

      NA2 = 0.29
      a2 = 50.
      lamda = 0.85

      n0 = 1.0
      aldeg1 = 0.
      aldeg2 = 0.

c Calculate fiber parameters and write some to the data file:


      V1 = 2*pi*a1*NA1/lamda
      V2 = 2*pi*a2*NA2/lamda
      Qc1 = asin(NA1)
      Qc2 = asin(NA2)

      write (13,14) " a1= ",a1," microns"
14    format (28X,A6,F5.1,A8)
      write (13,16) "lamda= ",lamda ,"microns"
16    format (28X,A9,F5.3,A8)
      write (13,1)
1     format (/)


      write (13,24) " a2 = ", a2 , "microns"
24     format (28X, A6, F5.1, A8)
      write (13,2)
2        format (/)



      write (13,34) "The normalized frequency  V1 = ",V1
34    format (5X,A31,F5.1)
      write (13,35) " Qc1 = ", Qc1
35    format (5x,A7,F7.3)
      write (13,36) "The gap index  n0 = ",n0
36    format (5X,A20,F5.3)
      write (13,3)
 3      format(/)


      write(13,44) "The normalized frequency V2 = ", V2
44    format(5X,A31,F5.1)
      write(13,46) " Qc2 = ", Qc2
46    format(5x,A7,F7.3)
```

```
      write(13,4)
4       format(/)


c Now the input ray positions and angles can be determined by dividing
c the available radius into psteps equal parts and angle into asteps.
c The position and angle increments are defined by the number of steps:

      if (psteps.GT.0) then
         pinc = a1/psteps
      else
         pinc = 0.0
      end if
      if (asteps.GT.0) then
         ainc = Qc1/asteps
      else
         ainc = 0.0
      end if
      ptot = 2*psteps + 1
      atot = 2*asteps + 1
      cntr = psteps*atot+asteps+1
      rows = ptot*atot

c Assign the input rays a Gaussian power distribution in angle.
c For now, this distribution is the same at every position.  Perhaps in
c future editions, the Gaussian parameter should vary with radius.
c It seems a bp = 0.05 is a reasonable value to start with for checking
c the effect of grading ray power along radius, and a possible way of
c grading would be to set inppow(m,3) = exp(-(ba*ainc*j*bp*pinc*i)**2).
?
c inppow(psteps*ptot+asteps+1,3) contains the power of the center ray.
c The factor ba determines shape of the Gaussian angular distribution.



c The parameters
      totpow = 0.
      intot = 0.
      endpow = 0.0

      do 140 m = -psteps,psteps
        do 120 n = -asteps,asteps
          j = n + asteps + 1
          i = (m + psteps)*(2*asteps + 1) + j
          r2(i,1) = m*pinc
          r2(i,2) = n*ainc
          r2(i,3) = exp(-(ainc*n*ba)**2) * exp(-(m*pinc*bp)**2)
          totpow = totpow + r2(i,3)
120     continue
140   continue


c Normalize total power so that sum of all ray powers equals 100 which
c is the max NA,  compare


       write (13,160)
160   format ("The input power matrix appears below.")
```

```
       write (13,170)
170    format ("col.1 = position, col.2 = angle, col.3 = ray power",
     +   " at that position and angle", /)

       do 200 k = 1,rows
          r2(k,3) = 100*r2(k,3)/totpow
          intot = intot + r2(k,3)
200    continue

        write (13,240) "Total input power = ",intot
240     format (/,A20,F5.1,/)


c ***************************************************************************

c Find the distribution in the near and far field of Emitting fiber,
c and the amount of power collected by the receiving fiber.
c First transform from the initial [r1(i,1], r1(i,2)] to
c final [r4(i,1),r4(i,2)]: (The concept is ralated to ABCD law). x2 is
c related to r3(i,1),take x2 into account, derive r3(i,1).

         do 360 d = 1000, 15000, 1000
         endpow = 0.0
         do 350 i = 1, rows
          r3(i,2) = r2(i,2)
          r3(i,1) = r2(i,1) + r2(i,2) * d
          r3(i,3) = r2(i,3)

c If fftest = 1, then calculate the far field power distribution.
c Otherwise, skip and directly calculate the amount of power captured.
c The matrix ffield has 201 rows and 2 columns.  ffield(n,1) holds
c the nth position in the far field at which the output power is
c calculated and ffield(n,2) holds the corresponding power.  The
c resolution along the axis perpendicular to the propagation direction
c is limitted to 201 positions, so that xsteps can at most be 100.

          if (fftest.NE.1) goto 330
          do 320 ix = -xsteps,xsteps
            mx = ix+xsteps + 1
            if (r3(i,1).GE.xinc*(ix-0.5)) then
              if (r3(i,1).LT.xinc*(ix+0.5)) then
              ffield(mx,2) = ffield(mx,2) + r3(i,3)
              end if
            end if
320       continue

330      if (abs(r3(i,1)).LE.a2) then
           if (abs(r3(i,2)).LE.Qc2) then
             endpow = endpow + r3(i,3)
           end if
         end if
350      continue

         write (16,*)  endpow

360      continue
```

```
      ffpow = 0.0
      do 400  ix = -xsteps, xsteps
         mx = ix + xsteps +1
         ffield(mx,1) = xinc*ix

         write (17,380) ffield(mx,1)
380      format (F10.1)

         write(14,390) ffield(mx,2)
390      format (F7.3)

         ffpow = ffpow + ffield(mx,2)

400   continue



c     write (9,*) "We got here, at least."


      write (9,*) "FINISHED RUNNING --  HIT RETURN KEY"
      pause
      end
```

Program 2

```
c This program models the loss of light as a function of displacement
c between two step index fiber ends.  It is essentially a ray tracing
c program with some Jones matrix notation thrown in.
c23456789 123456789 123456789 123456789 123456789 123456789 123456789 12

      integer i, j, k, l, m, n, ix, mx, itot
      integer psteps, asteps, ptot, atot, rows, cntr, xsteps, fftest
      real n0, n11, n12, n21, n22, a1, a2, lamda, h, angle
      real alpha1, alpha2, aldeg1, aldeg2, d, s, x, R, pow
      real Qc1, Qc2, Qcdeg1, Qcdeg2, NA1,NA2, V1, V2, b, NAmax
      real pinc, ainc, xinc, totpow, intot, endpow, a, bp, eneg1
      real inppow(6561,3), outpow(6561,3), ffield(1000,2)
      real r1(6561,3), r2(6561,3), r3(6561,3), r4(6561,3)

      write (9,*) "YOUR PROGRAM IS RUNNING"

c initialize data file and variable values:

      OPEN(13,FILE='inp.DAT',STATUS='NEW')
      OPEN(14,FILE='ffi.DAT',STATUS='NEW')
      OPEN(15,FILE='d.DAT',STATUS='NEW')
      OPEN(16,FILE='end.DAT',STATUS='NEW')
      OPEN(17,FILE='ex.DAT',STATUS='NEW')


c The vector inppow holds the input power at each position and angle.
c A total of 40 steps along diameter(12 along radius plus one in the
c center) are allowed and 40 angles are allowed at each position.  Thus
c inppow is a matrix with 81**2 rows, and three columns; the first for
c the position, the second for the angle, the third for the power at
c that position and angle.
c always remember rn(i,3) is the power, even though we use r.


      do 6 i = 1,6561
        do 5 j = 1,3
          r2(i,j) = 0.0
          r3(i,j) = 0.0

5       continue
6     continue
      do 7 i = 1,1000
        ffield(i,1) = 0.0
        ffield(i,2) = 0.0
7     continue

c psteps can at most be 40, asteps can at most be 40.

      pi = 3.14159265358
      psteps = 0.0
      asteps = 3000
      xsteps = 10
      xinc = 15
      ba = 14.5
```

```
      d = 10000

c These are the independent fiber variable:

      fftest = 0
      NA1 = 0.29
      a1 = 50.
      lamda = 0.85


      NA2 = 0.29
      a2 = 50.
      n0 = 1.0

c Calculate fiber parameters and write some to the data file:

      Qc1= asin(NA1)
      Qcdeg1 = 180*Qc1/pi
      V1 = 2*pi*a1*NA1/lamda
      Qc2 = asin(NA2)
      Qcdeg2 = 180*Qc2/pi
      V2 = 2*pi*a2*NA2/lamda


      write (13,14) " a1= ",a1," microns"
14    format (32X,A6,F5.1,A8)
      write (13,16) "lamda= ",lamda ,"microns"
16    format (28X,A9,F5.3,A8)
      write (13,1)
1     format (/)


      write (13,24) " a2 = ", a2 , "microns"
24     format (29X, A6, F5.1, A8)
      write (13,2)
2        format (/)


      write (13,30) "The critical angle  Qcdeg1 = ",Qcdeg1," degrees"
30    format (7X,A29,F5.2,A8)
      write (13,34) "The normalized frequency  V1 = ",V1
34    format (5X,A31,F5.1)
      write (13,36) "The gap index  n0 = ",n0
36    format (15X,A20,F5.3)
      write (13,3)
 3      format(/)


      write (13,40) "The critical angle  Qcdeg2 = ",Qcdeg2,"degrees"
40     format(7X,A29,F5.2,A8)
      write(13,44) "The normalized frequency V2 = ", V2
44     format(5X,A31,F5.1)
      write(13,4)
4       format(/)

c Now the input ray positions and angles can be determined by dividing
```

```
c the available radius into psteps equal parts and angle into asteps.
c The position and angle increments are defined by the number of steps:

      if (psteps.GT.0) then
         pinc = a1/psteps
      else
         pinc = 0.0
      end if
      if (asteps.GT.0) then
         ainc = Qc1/asteps
      else
         ainc = 0.0
      end if
      ptot = 2*psteps + 1
      atot = 2*asteps + 1
      cntr = psteps*atot+asteps+1
      rows = ptot*atot

c Assign the input rays a Gaussian power distribution in angle.
c For now, this distribution is the same at every position.  Perhaps in
c future editions, the Gaussian parameter should vary with radius.
c It seems a bp = 0.05 is a reasonable value to start with for checking
c the effect of grading ray power along radius, and a possible way of
c grading would be to set inppow(m,3) = exp(-(ba*ainc*j+bp*pinc*i)**2).
c inppow(psteps*ptot+asteps+1,3) contains the power of the center ray.
c The factor ba determines shape of the Gaussian angular distribution.


c The parameters

      bp = 0.00
      totpow = 0.
      intot = 0.
      endpow = 0.0
      eneg1 = 1/(Qc1*ba)
      write (13,80) "The 1/e power points are at ±",eneg1,"*Qc1."
80    format (A29,F4.3,A,/)

      do 140 m = -psteps,psteps
        do 120 n = -asteps,asteps
          j = n + asteps + 1
          i = (m + psteps)*(2*asteps + 1) + j
          r2(i,1) = m*pinc
          r2(i,2) = n*ainc
          r2(i,3) = exp(-(ba*ainc*n)**2)
          totpow = totpow + r2(i,3)
120     continue
140   continue


c Normalize total power so that sum of all ray powers equals 100

       write (13,160)
160   format ("The input power matrix appears below.")
       write (13,170)
170   format ("col.1 = position, col.2 = angle, col.3 = ray power",
     +  " at that position and angle", /)
```

```
      do 200 k = 1,rows
         r2(k,3) = 100*r2(k,3)/totpow
         intot = intot + r2(k,3)

200   continue

      write (13,240) "Total input power = ",intot
240   format (/,A20,F5.1,/)
c *********************************************************************

c Find the distribution in the near and far field of Emitting fiber,
c and the amount of power collected by the receiving fiber.
c First transform from the initial [r1(i,1], r1(i,2)] to
c final [r4(i,1),r4(i,2)]: (The concept is ralated to ABCD law). x2 is
c related to r3(i,1),take x2 into account, derive r3(i,1).Here there is
c limitation that r2(i,2),r3(i,2) must be acute angle, in fact, that is
c easy to be satisfied. h goes larger, R goes smaller, and angle will be
c bigger, the relationship is not linear. In this program, h can't be 0.
c but endpower could be calculated by using the program 8 when h is
equal
c to zero.

      do 360 h = 500, 14000, 500
        endpow = 0.0

        R = (27500.0**2 + h**2)/(h*2)
        angle = d/R

        do 350 i = 1, rows

         r3(i,2) = angle + r2(i,2)
         x = (R + r2(i,1))*sin(pi/2+r2(i,2))/sin(pi/2 - r3(i,2))
         r3(i,1) = x - R
         r3(i,3) = r2(i,3)



c If fftest = 1, then calculate the far field power distribution.
c Otherwise, skip and directly calculate the amount of power captured.
c The matrix ffield has 201 rows and 2 columns.  ffield(n,1) holds
c the nth position in the far field at which the output power is
c calculated and ffield(n,2) holds the corresponding power.  The
c resolution along the axis perpendicular to the propagation direction
c is limitted to 201 positions, so that xsteps can at most be 100.

        if (fftest.NE.1) goto 330
        do 320 ix = -xsteps,xsteps
          mx = ix+xsteps + 1
          if (r3(i,1).GE.xinc*(ix-0.5)) then
            if (r3(i,1).LT.xinc*(ix+0.5)) then
            ffield(mx,2) = ffield(mx,2) + r3(i,3)
           end if
          end if
320     continue


330     if (abs(r3(i,1)).LE.a2) then
         if (abs(r3(i,2)).LE.Qc2) then
```

```
            endpow = endpow + r3(i,3)
          end if
         end if
350      continue
         write (16,*) endpow

360      continue

        ffpow = 0.0
        do 400  ix = -xsteps, xsteps
           mx = ix + xsteps +1
           ffield(mx,1) = xinc*ix

           write (17,380) ffield(mx,1)
380        format (F10.1)

           write(14,390) ffield(mx,2)
390        format (F7.3)
           ffpow = ffpow+ffield(mx,2)
400     continue



c       write (9,*) "We got here, at least."
c       goto 999

999     write (9,1)
        write (9,*) "FINISHED RUNNING --  HIT RETURN KEY"
        pause
        end
```

Program 3

```
c This program models the loss of light as a function of displacement
c between two step index fiber ends.  It is essentially a ray tracing
c program with some Jones matrix notation thrown in.
c23456789 123456789 123456789 123456789 123456789 123456789 123456789

      integer i, j, k, l, m, n, ix, mx, itot
      integer psteps, asteps, ptot, atot, rows, cntr, xsteps
      real n0, n11, n12, n21, n22, a1, a2, lamda, h, angle
      real  d, s, x, R, pow, c, Qc1, Qc2, ba, NA1, NA2
      real pinc, ainc, xinc, totpow, intot, endpow,bp,eneg1
      real Re1, Re2, Rh1, Rh2, mi, Qm, T01, T02, m1
      real Re11, Re12, Rh11, Rh12, Re21, Re22, Rh21, Rh22
      real inppow(2500,3), outpow(2500,3), ffield(100,2)
      real r0(2500,3), r2(2500,3), r3(2500,3), rt(2500,3)
      real rI(2500,3), fftest, T1, T2

      write (9,*) "YOUR PROGRAM IS RUNNING"

c initialize data file and variable values:

      OPEN(13,FILE='inp.DAT',STATUS='NEW')
      OPEN(14,FILE='ffi.DAT',STATUS='NEW')
      OPEN(15,FILE='d.DAT',STATUS='NEW')
      OPEN(16,FILE='end.DAT',STATUS='NEW')
      OPEN(17,FILE='ex.DAT',STATUS='NEW')


c The vector inppow holds the input power at each position and angle.
c A total of 40 steps along diameter(12 along radius plus one in the
c center) are allowed and 40 angles are allowed at each position.Thus
c inppow is a matrix with 81**2 rows, and three columns; the first for
c the position, the second for the angle, the third for the power at
c that position and angle.
c always remember rn(i,3) is the power, even though we use r.


      do 6 i = 1,2500
        do 5 j = 1,3
          r0(i,j) = 0.0
          r2(i,j) = 0.0
          r3(i,j) = 0.0
          rt(i,j) = 0.0
          rI(i,j) = 0.0
          Q(i,j) = 0.0

5       continue
6     continue
      do 7 i = 1,100
        ffield(i,1) = 0.0
        ffield(i,2) = 0.0
7     continue

c psteps can at most be 10, asteps can at most be 10.
```

```
      pi = 3.14159265358
      psteps = 0
      asteps = 150
      xsteps = 10
      xinc = 15
      ba = 60
      d = 10000

c These are the independent fiber variable:

       fftest = 0
      NA1 = 0.29
       a1 = 50.
      lamda = 0.85


      NA2 = 0.29
       a2 = 50
      n0 = 1.0
      n1 = 1.5

c Calculate fiber parameters and write some to the data file:

       Qc1 = asin(NA1)
       Qc2 = asin(NA2)



c Now the input ray positions and angles can be determined by dividing
c the available radius into psteps equal parts and angle into asteps.
c The position and angle increments are defined by the number of steps:

       if (psteps.GT.0) then
         pinc = a1/psteps
       else
         pinc = 0.0
       end if
       if (asteps.GT.0) then
         ainc = Qc1/asteps
       else
         ainc = 0.0
       end if
       ptot = 2*psteps + 1
       atot = 2*asteps + 1
       cntr = psteps*atot+asteps+1
       rows = ptot*atot

c Assign the input rays a Gaussian power distribution in angle.
c For now, this distribution is the same at every position.  Perhaps in
c future editions, the Gaussian parameter should vary with radius.
c It seems a bp = 0.05 is a reasonable value to start with for checking
c the effect of grading ray power along radius, and a possible way of
c grading would be to set inppow(m,3) = exp(-(ba*ainc*j+bp*pinc*i)**2).
c inppow(psteps*ptot+asteps+1,3) contains the power of the center ray.
c The factor ba determines shape of the Gaussian angular distribution.
c The parameters
```

```
      bp = 0.00
       totpow = 0.
       intot = 0.0

       do 140 m = -psteps,psteps
        do 120 n = -asteps,asteps
          j = n + asteps + 1
          i = (m + psteps)*(2*asteps + 1) + j
          r2(i,1) = m*pinc
          r2(i,2) = n*ainc
          r2(i,3) = exp(-(ba*ainc*n)**2)
          totpow = totpow + r2(i,3)
120     continue
140     continue


c Normalize total power so that sum of all ray powers equals 100


       do 200 k = 1,rows
          r2(k,3) = 100*r2(k,3)/totpow
          intot = intot + r2(k,3)

200    continue

c ***************************************************************************

c Find the distribution in the near and far field of Emitting fiber,
c and the amount of power collected by the receiving fiber.
c First transform from the initial [r1(i,1], r1(i,2)] to
c final [r4(i,1),r4(i,2)]: (The concept is ralated to ABCD law). x2 is
c related to r3(i,1),take x2 into account, derive r3(i,1).Here there is
c limitation that r2(i,2),r3(i,2) must be acute angle, in fact, that is
c easy to be satisfied. h goes larger, R goes smaller, and angle will be
c bigger, the relationship is not linear. In this program, h can't be 0.
c but endpower could be calculated by using the program 8 when h is
equal
c to zero.

       do 400 h = 1000,15000,1000
        endpow = 0.0
       R = (27500.0**2 + h**2)/(h*2)
       angle = d/R
       Qm = acos((R-a1)/R)


       do 350 i = 1,rows


c r0(i,2) = Q0, r3(i,1) = Qinit, r0(i,1) = deltQ, r4(i,1) is incident
angle at the
c outer wall. rI(i,1) is the incident angle at the inner wall, rt(i,2)
is the
c refracted angle at the outer wall, rt(i,3) is the refracted angle at
the
c inner wall.

       if(r2(i,2).GT.Qm) then
```

```
rI(i,2) = acos(R*cos(r2(i,2))/(R-a1))
r0(i,2) = acos(R*cos(r2(i,2))/(R+a1))
r3(i,1) = r0(i,2) - r2(i,2)
r0(i,1) = r0(i,2) - rI(i,2)

  if (r3(i,1).GT.angle) then
    mi = -1.0
    else
    mi = abs((angle - r3(i,1))/r0(i,1))
  end if



rt(i,2) = asin(n0/n1*cos(r0(i,2)))
rt(i,3) = asin(n0/n1*cos(rI(i,2)))

Re11 = n0*cos(rt(i,2)) - n1*sin(r0(i,2))
Re12 = n0*cos(rt(i,2)) + n1*sin(r0(i,2))
Re1 = Re11/Re12

Rh11 = n0*sin(r0(i,2)) - n1*cos(rt(i,2))
Rh12 = n0*sin(r0(i,2)) + n1*cos(rt(i,2))
 Rh1 = Rh11/Rh12

T01 = (Re1**2 + Rh1**2)/2

Re21 = n0*cos(rt(i,3)) - n1*sin(rI(i,2))
Re22 = n0*cos(rt(i,3)) + n1*sin(rI(i,2))
Re2 = Re21/Re22

Rh21 = n0*sin(rI(i,2)) - n1*cos(rt(i,3))
Rh22 = n0*sin(rI(i,2)) + n1*cos(rt(i,3))
Rh2 = Rh21/Rh22

T02 = (Re2**2 + Rh2**2)/2
T1 = T01**INT(mi/2+1) * T02**INT((mi+1)/2)
r3(i,3) = r2(i,3) * T1

else if(r2(i,2).LT.-Qm) then

r0(i,2) = acos(R*cos(r2(i,2))/(R+a1))
rI(i,2) = acos(R*cos(r2(i,2))/(R-a1))
r3(i,1) = abs(rI(i,2) + r2(i,2))
r0(i,1) = abs(r0(i,2) - rI(i,2))

  if (r3(i,1).GT.angle) then
    mi = -1.0
    else
    mi = abs((angle - r3(i,1))/r0(i,1))
  end if



rt(i,2) = asin(n0/n1*cos(r0(i,2)))
rt(i,3) = asin(n0/n1*cos(rI(i,2)))

Re11 = n0*cos(rt(i,2))-n1*sin(r0(i,2))
Re12 = n0*cos(rt(i,2))+n1*sin(r0(i,2))
```

```
Re1 = Re11/Re12

Rh11 = n0*sin(r0(i,2))-n1*cos(rt(i,2))
Rh12 = n0*sin(r0(i,2))+n1*cos(rt(i,2))
 Rh1 = Rh11/Rh12

T01 = (Re1**2 + Rh1**2)/2

Re21 = n0*cos(rt(i,3))-n1*sin(rI(i,2))
Re22 = n0*cos(rt(i,3))+n1*sin(rI(i,2))
Re2 = Re21/Re22

Rh21 = n0*sin(rI(i,2))-n1*cos(rt(i,3))
Rh22 = n0*sin(rI(i,2))+n1*cos(rt(i,3))
Rh2 = Rh21/Rh22

T02 = (Re2**2 + Rh2**2)/2
T2 = T02**INT(mi/2+1) * T01**INT((mi+1)/2)

r3(i,3) = r2(i,3)* T2

else

  r0(i,2) = acos(R*cos(r2(i,2))/(R+a1))
  r3(i,1) = r0(i,2) - r2(i,2)
  r0(i,1) = 2*r0(i,2)

  if (r3(i,1).GT.angle) then
    mi = -1.0
    else
    mi = abs((angle - r3(i,1))/r0(i,1))
  end if


  rt(i,2) = asin(n0/n1*cos(r0(i,2)))

  Re11 = n0*cos(rt(i,2))-n1*sin(r0(i,2))
  Re12 = n0*cos(rt(i,2))+n1*sin(r0(i,2))
   Re1 = Re11/Re12

  Rh11 = n0*sin(r0(i,2))-n1*cos(rt(i,2))
  Rh12 = n0*sin(r0(i,2))+n1*cos(rt(i,2))
   Rh1 = Rh11/Rh12

  T01 = (Re1**2 + Rh1**2)/2

  r3(i,3) = r2(i,3)*(T01**(mi+1))

end if


  endpow = endpow + r3(i,3)

350    continue

write (16,*) endpow
```

```
400     continue

        write (9,*) "FINISHED RUNNING --  HIT RETURN KEY"
        pause
        end
```

VITA

Jing Wang was born in Beijing, China in 1963. She received a B.S. degree in Electrical Engineering from the Beijing Broadcasting Institute, Beijing in 1884, and attended Lehigh University, where she received M.S. degree in Electrical Engineering in 1994. She worked from 1984–89 at Beijing Broadcasting Institute as an instructor, Co-taught courses microwave technology and electromagnetics. Between April 1992 – September 1992, she worked in Binney and Smith Inc. as a technician, Conducted and recorded experimental formulation of pigment and dyes, prepared prototype samples and operated laboratory equipment. She received an academic award in 1983 in China, and became a member of ΦΒΔ Honorary Society for international scholar in 1994 at Lehigh University. She published "Structural Vibration Monitoring Using Deflection of a Hollow Core Optical Fiber" in Review of Progress in Quantitative Nondestructive Evaluation, (13A, pp381–387) in 1983.

END OF TITLE